Effect of H2S on SOFC anode structure and electrical performances

Hai Ha Mai Thi

UNIVERSITÉ DE GRENOBLE

THÈSE

Pour obtenir le grade de

DOCTEUR DE L'UNIVERSITÉ DE GRENOBLE

Spécialité : **Matériaux Mécanique Génie Civil Electrochimie**

Arrêté ministériel : 7 août 2006

Présentée par

Hai Ha MAI THI

Thèse dirigée par **Thierry PAGNIER** et
codirigée par **Nicolas SERGENT et Julie MOUGIN**

préparée au sein du **Laboratoire d'Electrochimie et de Physico-chimie des Matériaux et des Interfaces**
dans **l'École Doctorale Ingénierie – Matériaux Mécanique Energétique Environnement Procédés Production**

Effet de H_2S sur la structure et les performances électriques d'une anode SOFC

Thèse soutenue publiquement le **30 Janvier 2014**,
devant le jury composé de :

Mme Elisabeth DJURADO
Professeur, Grenoble-INP, Présidente
Mme Rose-Noëlle VANNIER
Professeur, ENSC Lille, Rapporteur
Mr Jean-Marc BASSAT
DR, ICMC Bordeaux, Rapporteur
Mr Stéphane LORIDANT
CR, IRCELYON, Membre
Mr Thierry PAGNIER
CR, LEPMI Grenoble, Invité
Mme Julie MOUGIN
Chef de Laboratoire, CEA Grenoble, Membre
Mr Nicolas SERGENT
Maître de Conférences, Grenoble-INP, Membre

UNIVERSITÉ DE GRENOBLE

THÈSE

Pour obtenir le grade de

DOCTEUR DE L'UNIVERSITÉ DE GRENOBLE

Spécialité : **Matériaux Mécanique Génie Civil Electrochimie**

Arrêté ministériel : 7 août 2006

Présentée par

Hai Ha MAI THI

Thèse dirigée par **Thierry PAGNIER** et
codirigée par **Nicolas SERGENT et Julie MOUGIN**

préparée au sein du **Laboratoire d'Electrochimie et de Physico-chimie des Matériaux et des Interfaces**
dans **l'École Doctorale Ingénierie – Matériaux Mécanique Energétique Environnement Procédés Production**

Effet de H_2S sur la structure et les performances électriques d'une anode SOFC

Thèse soutenue publiquement le **30 Janvier 2014**,
devant le jury composé de :

Mme Elisabeth DJURADO
Professeur, Grenoble-INP, Présidente
Mme Rose-Noëlle VANNIER
Professeur, ENSC Lille, Rapporteur
Mr Jean-Marc BASSAT
DR, ICMC Bordeaux, Rapporteur
Mr Stéphane LORIDANT
CR, IRCELYON, Membre
Mr Thierry PAGNIER
CR, LEPMI Grenoble, Invité
Mme Julie MOUGIN
Chef de Laboratoire, CEA Grenoble, Membre
Mr Nicolas SERGENT
Maître de Conférences, Grenoble-INP, Membre

Thương tặng bố An, mẹ Cúc
anh Sơn, em Cường, em Anh
em Trang, cháu Tùng (kiwi)

To my family,
for the unconditional love
and support

Acknowledgements

Foremost, I would like to express my deepest gratitude and appreciation to my supervisor Dr. Thierry Pagnier for his greatest guidance, patience, and excellent caring even in daily life. My sincerest thanks also go to my co-advisor Dr. Nicolas Sergent, Dr. Bernadette Saubat for their enormous, enthusiastic helps in setting up the experimental measures, interpretations of the Raman spectra and correcting my thesis. I also thank Dr. Julie Mougin for her helpful discussions. Without their contributions and support, this work would not have been realized.

I am also grateful to Frédéric Charlot, Stéphane Coindeau, Michel Dessarts for their greatest helps in SEM, XRD analysis and sample preparations.

I would also like to acknowledge with much appreciation the crucial role of the defense committee including Prof. Elisabeth Djurado, Prof. Rose-Noëlle Vannier, Dr. Jean-Marc Bassat, Dr. Stéphane Loridant for their acceptance to evaluate my work and their invaluable scientific discussions.

I would like to thank the members of LEPMI including Thierry, Nicolas, Bernadette, Noël, Denis, Alain, Priscillia, Michel, Alex, Vincent for proving me with an intimate working atmosphere. A special thanks goes to Noël and Bernadette who always consoled me and proposed me to another relaxing activities.

I offer my sincere appreciation to Ass. Prof. Nguyễn Thị Phương Thoa, Dr. Mẫn, Dr. Phụng who introduced me to the project “Pile-eau-biogaz”.

Many thanks go to Floriane and her family, “bạn” Lệ Thủy, Thu Thủy, Trà, Hùng, Chương, “anh” Bảo, Trinh, “chị” Giang, Hương, Đạt, Kiên, Phước, Priew, Emeline, Isabel, Mohammed who have cheered me up, kept me balanced with warm cares, interesting trips and warm meals. Special thanks to Lệ Thủy and Thu Thủy for being like my sisters.

Finally, and most importantly, I would like to thank my family for their unending support from the distance. Deepest thanks to my older brother Sơn, his girlfriend Điệp and my cousin Anh, who covered distance to be with me in the last difficult moment of my thesis defense date.

CONTENTS

GENERAL INTRODUCTION

Biogas is formed by the anaerobic decomposition of organic waste including carbohydrates, fats and proteins. It has turned to be a potential sustainable energy source through the three European Union policies: the Renewable Energy Directive 2009/28/CE that is aiming for a 20% renewable energy share in gross final energy consumption by 2020, the Directive 1999/31/CE that requires the reduction of the amount of biodegradable waste disposed of in landfills, and the Directive 2008/98/EC encouraging waste recycling and recovery.

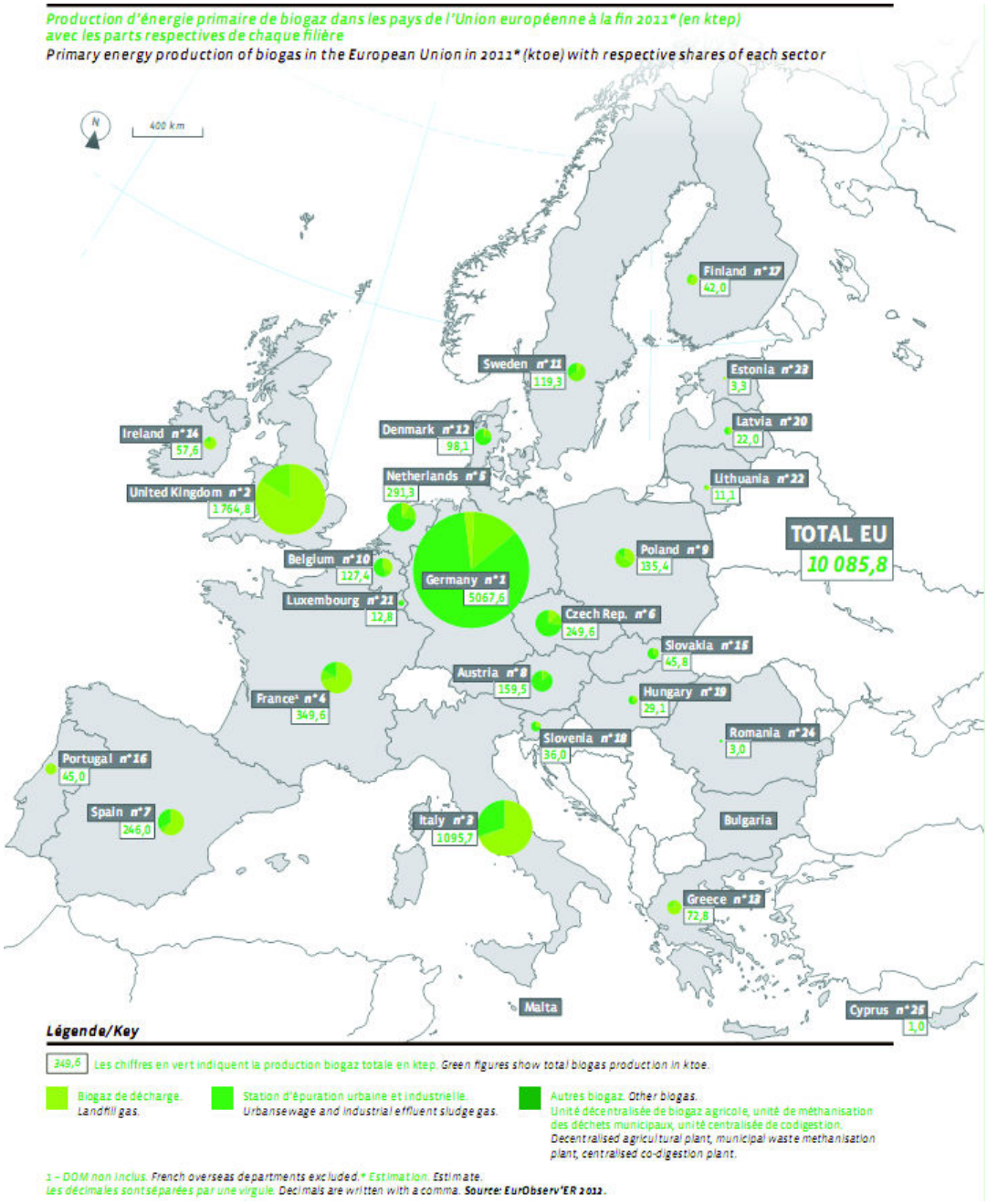

Figure 1. Production of primary energy of biogas in Europe in 2011 [1]

According to the data given by Eurobserv'Er 2012 [1], the production of primary energy of biogas in Europe in 2011 was 10 Mtoe (Million Tons of Oil Equivalent). The purpose-designed energy recovery plants (collectively grouped as "other biogas" which includes decentralised agricultural plant, municipal solid waste methanisation plant, centralised co-digestion plant) dominate the field with their 56.7% share. They overweight the other production channels of landfill biogas (31.3%) and wastewater treatment plants (12%). Each country has different biogas development strategy as displayed in Figure 1. Landfill biogas is the main player in the UK, France, Italy and Spain, whereas "other biogas" dominates the German, Dutch, Austrian, Belgian, Danish, and many of the Eastern Europe's markets.

The primary energy of biogas is used to generate electricity or cogenerate electricity (21 TWh in 2011) and heat (55 ktoe in 2011). A combined heat and power engine (CHP) is presented in Figure 2 [2]. The fuel gas is burnt and converted into mechanical energy via a cylinder's combustion engine. This mechanical energy is in turn used to turn the engine's alternator in order to produce electricity. The electrical efficiency of the engine is ~40%. The heat produced is recovered directly on site for drying sludge, heating buildings and maintaining the digester at optimum temperature. CHPs are typically embedded close to the end user, therefore help reduce transportation and distribution losses. They regularly reach 80% or even 90% efficiency (the amount of fuel burned relative to the energy gain) at the point of use. Gas-fired power stations are normally around 50% efficient, whilst coal-fired power stations are even worse at 38%.

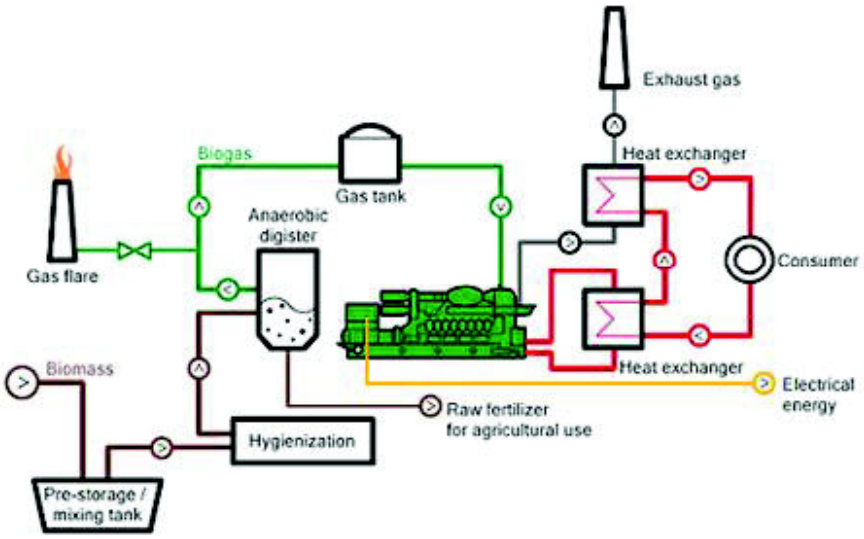

Figure 2. Simple drawing of a combined heat power engine [2]

High temperature Solid Oxide Fuel Cells (SOFCs) are well suited for on-site cogeneration of heat and power plant [3], or to integrate with conventional power plants of gas turbine, coal-fired types to convert available heated fuel in the effluent into additional power [4]. They can be fed with a wide variety of fuels without a preliminary reforming because of their high operating temperature of 700-1000°C. Indeed, the methane is reformed *in situ* into hydrogen inside the cell by carbon dioxide or steam also present in the biogas.

Besides the main components of methane and carbon dioxide, biogas contains numerous minor elements: sulfur, halogenated compounds, terpenes, alcohols, ketones, alkenes, cyclic hydrocarbons, aromatics, esters or silicon compounds (silanols, siloxanes). Some are unwanted for SOFC applications. They may poison the electrodes, for example, mask the catalytic sites by sulfur adsorption or carbon deposition. Siloxanes and silanols are the sources of solid inorganic silicon deposits during the biogas combustion, and are responsible for production stoppages.

In this context, the thesis will focus mainly on the identification and the understanding of interactions between hydrogen sulfide, the most common impurity in biogas, and anode materials at different temperatures, as well as functioning anode. The study is expected to reveal the poisoning rate and extent at various conditions, and also to elucidate the modifications of electrochemical properties of SOFC caused by the reaction between anode and H_2S.

Chapter 1 will focus on the properties of materials used to fabricate SOFC anode, on the oxidation mechanisms on the anode together with its electrochemical properties - possible sources of anode overvoltage. The suggested impacts of H_2S will be also summarized.

Chapter 2 will describe the principles of techniques employed *in situ* and *ex situ* with much emphasis on Impedance Spectroscopy and Raman spectroscopy. Sample preparations and experimental procedures will be also included.

Chapter 3 will be dedicated to the effects of H_2S on anode materials: the reaction kinetics, the poisoning extent reflected through structural/morphological changes, the spatial distributions of sulfide compounds at different temperatures.

At last, in chapter 4, the relations between anode electrochemical properties and compositional/morphological modifications due to H_2S will be revealed. An equivalent circuit based on Volmer-Heyrovsky mechanism will be employed to find out the most H_2S-vulnerable process under open circuit and polarizing conditions.

REFERENCES

[1] http://eurobserv-er.org/ (29/10/2013)
[2] http://www.clarke-energy.com/chp-cogeneration/ (29/10/2013)
[3] *Solid Oxide Fuel Cells: Materials Properties and Performance*; J. W. Fergus, Ed.; CRC Press, 2009.
[4] A. Verma, A. D. Rao, G. S. Samuelsen, *J. Power Sources* **2006**, *158*, 417.

Chapter 1

LITERATURE SURVEY

CONTENTS

1. Introduction

Hydrogen is considered as the primary fuel with large quantity being produced from biogas, natural gas, liquid hydrocarbons or coal gas through external reformers [1]. A Solid Oxide Fuel Cell (SOFC) can transform directly these sources into electricity due to its high operating temperatures of 700-1000°C. As a result, it is most suitable to be used in on-site/distributed generation power plants (100-500 kW system) [2]. Micro SOFCs operating at 300-600°C are also considered for portable electronic devices (500 W battery chargers) [3,4]. Nevertheless, numerous minor elements in biogas like sulfur or halogenated compounds may degrade fast SOFC anodes.

This chapter will introduce the SOFC functioning principle and the properties of its components materials, especially the anode and the electrolyte. A detailed oxidation mechanism on the anode together with its electrochemical properties will be reviewed. The last part will cover the impacts of H_2S reported in various experimental conditions from the literature.

2. Fundamental structure of a SOFC

The basic components of a SOFC and the net reactions at each electrode are given in Figure 1. The gaseous fuel diffuses into the porous structure of the anode, and is oxidized with the help of an oxygen ion from the electrolyte to release electrons. The electrons next transport through the electronically conducting phase in the anode to the external circuit and to the cathode. There, molecular oxygen is reduced into oxygen anions.

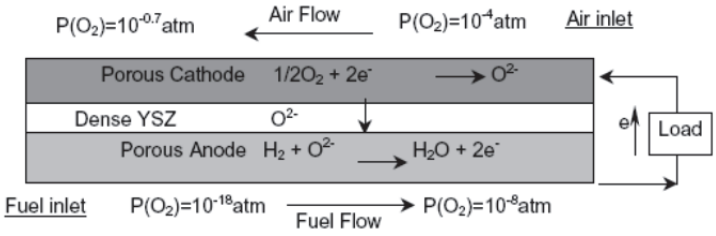

Figure 1. Simple drawing of a SOFC with the net reactions at each electrode [5].

The overall cell reaction may be:

$$H_2 + ½\ O_2 \rightarrow H_2O \qquad (1)$$

$$CO + ½\ O_2 \rightarrow CO_2 \qquad (2)$$

$$CH_4 + 2O_2 \rightarrow CO_2 + 2H_2O \qquad (3)$$

The SOFC electrolyte is an oxygen-anion conductor. The operating temperature of the SOFC is mostly set by the requirement for high ionic conductivity of the electrolyte. So, for example, a temperature higher than ~700°C is necessary for yttria-stabilized zirconia electrolyte [6].

Any part of a SOFC, anode, cathode, or electrolyte, can serve as a mechanical support which is made much thicker than other parts. The favor trend today is to reduce the operating temperature from ~1000°C to 500-800°C in order to reduce the cost of the other parts of SOFC. Therefore, a cell design with a thin electrolyte to lower the ohmic resistance and a thick mechanical support on the anode side is the best choice (Figure 2). The support is usually made of the anode material, but with a coarser microstructure than that of the anode functional layer [7].

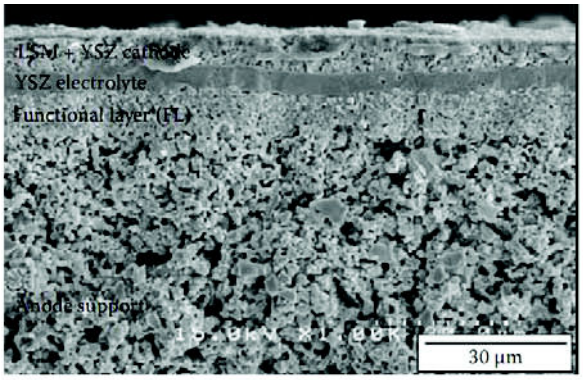

Figure 2. Cross-sectional view of an anode-supported SOFC with thin layers of cathode, electrolyte, functional anode and a thick layer of anode support [8].

2.1. Electrolyte

The electrolyte of a SOFC is a solid oxide ion conductor which has to meet certain criteria on the electrochemical, chemical, thermodynamical, thermal and mechanical properties as listed below [9]:

- a high ionic conductivity for the oxygen anion (> 10^{-3} S cm^{-1}), and a low electronic conductivity (to avoid an internal short circuit between the anode and the cathode) over a wide range of oxygen pressures, since the electrolyte is subjected to an oxidizing atmosphere at the cathode side (P_{O_2} ~1 atm) and to a reducing atmosphere at the anode side (P_{O_2} ~10^{-20} atm);
- to be chemically stable in relation to the reactant environment and contacting electrode materials under SOFC operation as well as fabrication conditions;
- a thermal expansion compatible with the other parts;
- to be dense enough to separate the fuel and the air compartments;
- to be thermodynamically stable over a wide range of temperature and P_{O_2} .

The ionic conductivity of the solid oxide is defined as follows:

$$\sigma = \sigma_o . e^{\frac{-E}{RT}} \qquad (4)$$

where σ_o and E are factors depending on the electrolyte materials, T is the electrolyte temperature, and R is the ideal gas constant. The ionic conductivity will increase by increasing the operating temperature, or by refining the crystal structure by doping methods.

Four groups of material have been used as SOFC electrolyte: doped ZrO_2 and CeO_2, $LaGaO_3$-based perovskites, and apatites [7]. The first two groups are most widely employed and are thus discussed further.

2.1.1. Doped zirconia

Pure zirconium oxide has three polymorphic structures depending on temperature as follows:

$$\text{Monoclinic} \xleftrightarrow{1170^oC} \text{Tetragonal (distorted fluorite structure)} \xleftrightarrow{2370^oC} \text{Cubic (fluorite structure)} \qquad (5)$$

The phase transformation from the sintering temperatures to low usage temperatures, especially from t-ZrO_2 to m-ZrO_2, is accompanied by a large volume change which can fragmentize the material. This phenomenon can be suppressed by the additions of lower valence metal oxides M_xO_y such as CaO, Y_2O_3 or rare-earth oxides. These dopants form solid solution with ZrO_2, thus help to stabilize t- and c- ZrO_2 at low temperatures (see Figure 3).

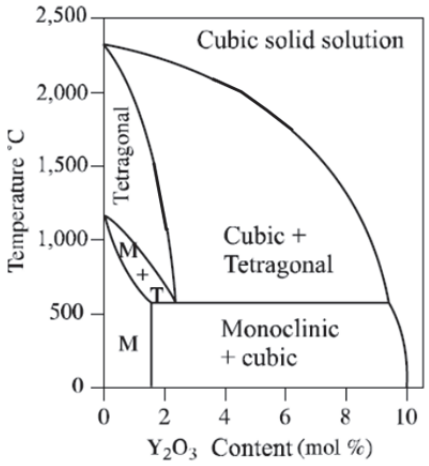

Figure 3. ZrO_2-Y_2O_3 diagram [10].

Besides the stabilization effect, the substitution of Zr^{4+} with a lower valence ion Y^{3+} or Ca^{2+} at the corresponding lattice sites will introduce oxygen vacancies according to the equation below:

$$Y_2O_3 \xrightarrow{2ZrO_2} 2Y'_{Zr} + V_O^{\cdot\cdot} + 3O_O^{\times} \qquad (6)$$

The oxygen ions can migrate through the vacancies (or the vacancies are transportable), thus creating the ionic conductivity of stabilized zirconia.

According to Bonanos et al. [11], fully stabilized zirconia (FSZ) with a cubic structure has a high ionic conductivity at elevated temperature. Partially stabilized zirconia (PSZ) consisting of

cubic and tetragonal phases has good mechanical strength and toughness. Tetragonal stabilized zirconia (TZP) has a high mechanical strength, which exceeds 1 GPa. The available TZP has a composition of 3 mol% Y_2O_3, and FSZ has 8 mol% Y_2O_3, their corresponding conductivities are given in Table 1. No significant degradation of the conductivity with aging at 1000°C was observed in TZP [12].

Table 1. Ionic conductivities of two widely used yttria-doped zirconia.

Sample	Phase	Conductivity ($S.cm^{-1}$)		Activation energy ($kJ.mol^{-1}$)	Ref.
		1000°C	800°C		
ZrO_2 - 3 mol% Y_2O_3	Tetragonal	6.5×10^{-2}	1.8×10^{-2}	72	[12]
		4×10^{-2}			[13]
ZrO_2 - 8 mol% Y_2O_3	Cubic	1.6×10^{-1}	4.5×10^{-2}	70	[12]

A high dopant concentration leads to the introduction of more vacancies into the lattice, as well as more interactions (associations) between oxygen vacancies and dopant cations, which reduce the free vacancy concentration [11]. So, the conductivity as a function of the dopant concentration will reach a maximum at relatively low additions of dopant. The composition with 8 mol% Y_2O_3 (8YSZ) has traditionally dominated because the ionic conductivity exhibits a maximum at that yttria content.

2.1.2. Doped ceria

Both doped and undoped ceria possess a mixed ionic and electronic conductivity at low oxygen pressure. The conductivity depends on the activation energies of the oxygen ion migration via the oxygen vacancies and of the defect complex association. The contribution of the electronic conductivity becomes significant under reducing atmosphere at high temperature.

Trivalent rare earth oxides dopants such as Gd_2O_3, Sm_2O_3, Y_2O_3 can induce a much higher conductivity and stability with CO_2 and H_2O than bivalent ones because they have an ionic radius closer to that of the host ion [14]. The oxide ion conductivity is a function of temperature, dopant concentration and type as read from Table 2.

Table 2. Ionic conductivity of rare earth oxides-doped ceria [15]

Composition	Dopant	r_d (Å)	ΔE (eV)	σ_0	σ ($S\,cm^{-1}$)		
					500 °C	600 °C	700 °C
$Ce_{0.9}Gd_{0.1}O_{1.95}$	Gd^{3+}	1.053	0.64	1.09×10^5	0.0095	0.0253	0.0544
$Ce_{0.9}Sm_{0.1}O_{1.95}$	Sm^{3+}	1.079	0.66	5.08×10^4	0.0033	0.0090	0.0200
$Ce_{0.887}Y_{0.113}O_{1.9435}$	Y^{3+}	1.019	0.87	3.16×10^6	0.0087	0.0344	0.1015
$Ce_{0.8}Gd_{0.2}O_{1.9}$	Gd^{3+}	1.053	0.78	5×10^5	0.0053	0.018	0.047

The maximum ionic conductivity occurs at ~10-20 mol% for most dopants. $Ce_{0.9}Gd_{0.1}O_{1.95}$ (10CGO) is the most studied ceria based electrolyte [9]. The inconsistence of the conductivity peaks for different Gd contents shown in Figure 4 might come from impurities inside the starting materials, synthesis processes, and sintering conditions which create different microstructures with different grain boundaries and bulk resistances. The impurities may come from the original ores as SiO_2 is ubiquitous in minerals, from furnace refractories during the sintering procedure or from glass-ware used for the precursor fabrication [14].

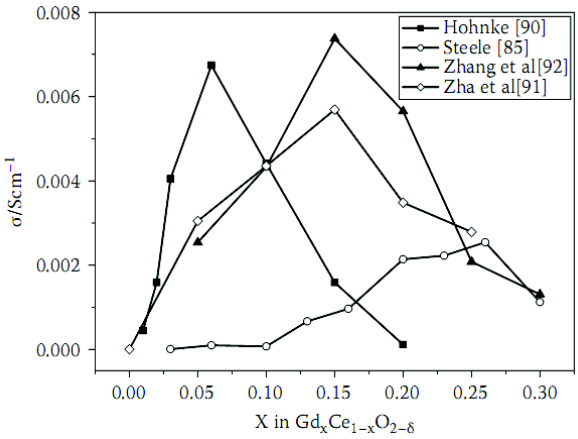

Figure 4. Conductivity at 500°C of Gd-doped ceria as a function of Gd concentration [14].

The ionic conductivity also depends on surrounding atmosphere. In general, there exist always exchanges of oxygen between the solid (O^{2-} ions), at least at the surface, and the gaseous atmosphere (oxygen molecules), followed by the formation of oxygen vacancies. The two electrons of O^{2-} ion remain on the oxygen site. They are strongly attracted by the nearby cations and easily delocalised on all the cationic sites of the solid. The nature of majority defects (doubly ionized oxygen vacancies $Vo^{\cdot\cdot}$ and electrons) depends on the temperature and on the partial pressure of oxygen. In a reducing atmosphere (P_{O_2} <10^{-18} bar), $Vo^{\cdot\cdot}$ and electrons are in majority (n-type electronic conduction), while in an oxidizing atmosphere (P_{O_2} >10^{-10} bar), cationic vacancies are numerous and capture the electrons released (p-type electronic conduction) [10].

The prominent drawback of ceria is that, at low oxygen partial pressure and high temperature, Ce^{4+} is easily reduced to Ce^{3+}, resulting in a n-type electronic conduction and a lattice expansion. The electronic conduction will facilitate electronic leakage currents between anode and cathode [9]. The lattice expansion may create cracks and fissures at the electrode/electrolyte interface and a subsequent delamination of the electrode from the electrolyte [5,16].

Moreover, CeO_2 will react with YSZ at high temperatures [1,5,7]. So, doped ceria is most suitable for intermediate temperature SOFC (below 800°C) [5], while doped zirconia is better for high temperature SOFC.

2.2. Anode material and three-phase boundary

The material for SOFC anode is a porous cermet (a composite of ceramic and metal) which is a mixed ionic and electronic conductor. The two most commonly applied anodes are Ni-YSZ and Ni-CGO because of their low cost, high conductivities and good catalytic activities [17]. Ni serves as a catalyst for H_2 bond breaking, steam reforming of hydrocarbons and as a channel for electron transport. The ceramic phase acts mainly as a framework to retain the dispersion of the metal particles and the porosity during long-term operation, as well as a channel for O^{2-} to diffuse farther into the anode. Moreover, the porosity provides the pathways for the fuel diffusion and products removals.

Oxidation reaction can only occur at triple phase boundaries (TPB), the positions where the ionic conducting phase (for O^{2-}), electronic conducting phase (for H_{ads}, electron) and gas phase are in contact. The effective TPB in fact extends ~10 μm from the electrolyte into the electrode despite the effort to use cermet anode [18,19]. The electrolyte material within the electrode is only effective if its particles are sintered to the electrolyte and linked together. This requires a high sintering temperature of at least 1500K for YSZ particles [6]. It is clear that SOFC performance depends strongly on the microstructure of the anode, in which a fine homogeneous distribution of three phases is important for anode to operate efficiently.

The electrical conductivity of a cermet anode depends on the particle size, size distribution, contiguity of each component, porosity, and ratio of nickel/YSZ content. The percolation threshold for the electronic conductivity is at about 30 vol% nickel as indicated in Figure 5. This value decreases when the NiO particle size is reduced while the YSZ size is increased. It is the average size, not the BET-specific surface that determines the cermet conductivity, since small particles can agglomerate to give a surface area similar to that of big particles [14]. The suggested anode electronic conductivity varies from 1 to 100 S/cm, depending on how well a current collector is connected to the anode [20].

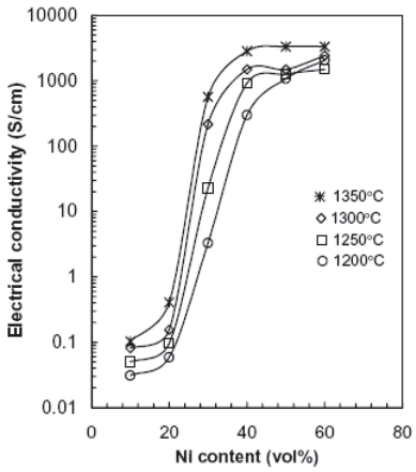

Figure 5. Electrical conductivity at 1000°C of Ni-YSZ as a function of nickel concentration at various temperatures [14].

When operating on hydrocarbon fuels, the anode must be stable against carbon dioxide and sulfide compounds. Ni, however, is sensitive to sulfur and catalyzes the deposition of carbon [1,6], leading to a rapid deterioration of the cell performances. One approach is to replace Ni with Cu which catalyzes nothing and add cerium oxide to act as an oxidation catalyst [1], another one is to dope Ni/YSZ anode with molybdenum and gold [5].

2.3. Cathode

The cathode in SOFC is responsible for the reduction of oxygen and the transport of oxygen ions to the electrolyte. So, it also operates based on the triple phase boundaries like the anode. A typical choice is the perovskite $(La,Sr)MnO_{3\pm d}$ (LSM) [9,14]. The YSZ/LSM composite is used primarily instead of Sr-doped $LaFeO_3$ (LSF) or $LaCoO_3$ (LSC) since YSZ-LSM mixtures can be heated to higher temperatures before undergoing a solid state reaction with YSZ to form a $La_2Zr_2O_7$ insulating phase [21,22], resulting in the cell degradation.

For lower operation temperatures of SOFCs, $La_{1-x}Sr_xCo_{1-y}Fe_yO_{3-d}$ (LSCF) may be used for its fast ion transport, good oxygen reduction kinetics and acceptable electronic conduction [9].

3. Oxidation mechanism on SOFC anode

The reaction mechanism on the SOFC anode is still under discussion while the net reaction is widely accepted as follows:

$$\mathbf{H_{2,gas} + O_{o\,YSZ}^{\times} \rightarrow H_2O_{gas} + V_{O\,YSZ}^{\cdot\cdot} + 2e_{Ni}^{-}} \qquad (7)$$

A rather clear picture was given by Vogler et al. [23], in which the author formulated possible processes into various elementary processes of surface diffusions, surface chemical reactions, and charge transfer reactions as follows where s denotes a free surface site:

- **Ni surface chemical reactions:**

$H_{2,gas} + 2s_{Ni} \rightleftharpoons 2H_{Ni}$ (8) (adsorption and dissociation of H_2 gas)

$H_{Ni} + O_{Ni} \rightleftharpoons OH_{Ni} + s_{Ni}$ (9)

$H_{Ni} + OH_{Ni} \rightleftharpoons H_2O_{Ni} + s_{Ni}$ (10)

$H_2O_{gas} + s_{Ni} \rightleftharpoons H_2O_{Ni}$ (11)

$H_2O_{Ni} + O_{Ni} \rightleftharpoons 2\ OH_{Ni}$ (12)

The heterogeneous chemistry on Ni is fast, there is almost no influence of the kinetic parameters related to the Ni surface.

- **YSZ surface chemical reaction:**

$$H_2O_{gas} + s_{YSZ} \rightleftharpoons H_2O_{YSZ} \quad (13)\text{ (adsorption of steam)}$$

$$H_2O_{YSZ} + O^{2-}_{YSZ} \leftrightharpoons 2OH^{-}_{YSZ} \quad (14)\text{ (dissociation of adsorbed water)}$$

$$O^{\times}_{O\,YSZ} + s_{YSZ} \leftrightharpoons O^{2-}_{YSZ} + V^{\cdot\cdot}_{O\,YSZ} \quad (15)\text{ (bulk-surface exchange)}$$

The rate coefficients of these reactions have not yet been reported.

- **Charge-transfer reaction:**

$$H_{Ni} + O^{2-}{}_{YSZ} \rightleftharpoons OH^{-}{}_{YSZ} + e^{-}{}_{Ni} + s_{Ni} \quad (16)\text{ (hydrogen spillover into YSZ surface)}$$

$$H_{Ni} + OH^{-}{}_{YSZ} \rightleftharpoons H_2O_{YSZ} + e^{-}{}_{Ni} + s_{Ni} \quad (17)\text{ (hydrogen spillover)}$$

$$O^{2-}{}_{YSZ} \rightleftharpoons O^{-}{}_{YSZ} + e^{-}{}_{Ni} \quad (18)$$

$$O^{2-}{}_{YSZ} + s_{Ni} \rightleftharpoons O^{-}{}_{Ni} + e^{-}{}_{Ni} + s_{YSZ} \quad (19)\text{ (oxygen spillover into Ni surface)}$$

$$O^{-}{}_{Ni} \rightleftharpoons O_{Ni} + e^{-}{}_{Ni} \quad (20)$$

$$O^{2-}{}_{YSZ} + s_{Ni} \rightleftharpoons O_{Ni} + 2e^{-}{}_{Ni} + s_{YSZ} \quad (21)\text{ (oxygen spillover into Ni surface)}$$

$$OH^{-}{}_{YSZ} + s_{Ni} \rightleftharpoons OH_{Ni} + e^{-}{}_{Ni} + s_{YSZ} \quad (22)\text{ (oxygen spillover into Ni surface)}$$

- **Surface diffusion :**

Many species diffuse to take part in the reaction, including H_{Ni}, O_{Ni}, OH_{Ni}, H_2O_{Ni}, O^{2-}_{YSZ}, H_2O_{YSZ}, OH^{-}_{YSZ}.

By conducting semi-empirical models counting all the chemical reactions and diffusion steps with only one or two charge-transfer reactions, the authors supported the hydrogen spillover pathway and the four rate-determining processes are: water adsorption/desorption on YSZ, water dissociation on YSZ, surface diffusion of OH^{-}_{YSZ} and hydrogen spillover to oxide ion.

However, the density-functional theory calculations by Rossmeisl et al. [24] of the surface adsorption energies of the hydrogen atoms, oxygen atoms and hydroxyl radicals on metals showed that the measured conductivity obtained by Setoguchi et al. [25] is well-correlated with the oxygen binding energies, indicating the dominance of oxygen spillover reaction pathway.

No consensus exists so far concerning the kind of the rate determining reaction step. It is assumed to be the hydrogen adsorption/diffusion process on the surface of Ni particles and a charge transfer process on zirconia electrolyte surface by Jiang et al. [26]. Different findings from the literature may imply that the active mechanism varies with operating conditions and/or sample preparation methods [24].

4. SOFC electrode polarization

The cell potential V under current I is always lower than the equilibrium value E° due to losses/polarizations in the electrodes $\eta_{anode/cathode}$ and electrolyte:

$$V = E° - IR - \eta_{anode} - |\eta_{cathode}| \quad (23)$$

IR is purely ohmic, contributed mostly from the electrolyte rather than electrodes due to the low value of ionic conductivity [5,6].

For the anode, the losses may come from many sources including [5]:

- a concentration polarization resistance due to the limited diffusion of gas phase and adsorbed species to/from/on the electrodes surfaces;
- an activation polarization resistance induced from activation barriers of the electrochemical reaction steps at the triple-phase boundaries. The anode polarization depends strongly on the anode microstructure which in turn varies with processing approach, characteristics of starting raw material, Ni content, Ni:YSZ ratio and sintering temperature. 40-45 vol.% Ni is considered to be able to minimize the overpotential by enlarging the TPB length [5,27];
- a contact resistance between the anode and the electrolyte. The resistance decreases monotonically with the increase in Ni content [27];
- an internal resistance to electron transport, which depends on the anode thickness. Its contribution is negligibly low compared to the three above resistances owing to anode fairly high predominant electronic conductivity [27].

The anode overpotential is reported to be independent of the H_2 concentration under dry condition, and is reduced significantly in the presence of steam. Steam probably accelerates the adsorption/desorption of hydrogen. Also, the overpotential is decreased by decreasing the gas flow rate [28].

5. Effects of sulfide pollutants

5.1. Major components of biogas

Landfill biogas is the main source in France. The composition varies strongly depending on many factors like waste sources (urban, industrial, or agricultural waste), landfill storage height and density, air temperature, atmospheric pressure and precipitation levels (see Table 3). One million tons of city solid waste generate 1.7-2.5 million m^3 of collectable methane, enough to fuel a gas engine capacity of 850-1,250 kW producing 6,500 to 10,000 MWh of electricity per year. That roughly corresponds to the average power demand of 1,500-2,200 EU households [29].

Table 3. Composition of main components of biogas from two different feedstocks (ADEME - Gaz de France).

Composition (by % volume)	Farm plant	Sewage treatment plants
Methane (CH_4)	22 – 65 %	50 – 74 %
Carbon dioxide (CO_2)	15 – 51%	25 – 49 %
Nitrogen (N_2)	0 – 54 %	0 – 5.4 %
Oxygen (O_2)	0 – 11%	0 – 1.5 %
Hydrogen (H_2)	< 0.002 – 3 %	< 1 %
Water vapeur	1.4 – 15.2 %	0.2 – 16.4 %

5.2. Minor components of biogas

Besides the main compounds listed above, ~250 minor elements grouped into 17 chemical families can be found in biogas such as particulate matter, tar, alkali metal compounds and halides, sulfur compounds (sulfides, disulfides and mercaptans), terpenes, alcohols, ketones, alkenes, cyclic hydrocarbons, aromatics, esters or silicon compounds (silanols, siloxanes) [30-33].

The literature study indicates detrimental effects of sulfide and silicon compounds. Siloxanes are formed from materials in soaps and detergents. During the combustion process, silicon is released and can combine with free oxygen or other elements in the gas to form silica (SiO_2) or silicates (Si_xO_y) deposits. Siloxanes are often problematic in landfill gas and sewage gas plants while much less in agricultural biogas plants [29]. Hydrogen sulfide (H_2S) is derived from high sulfur feedstocks such as amino-acids and proteins. When burnt in a gas engine, hydrogen sulfide can condense with water to form sulfuric acid which is corrosive [29]. The concentrations of these compounds are given in Table 4.

Table 4. Composition of sulfide compounds in biogas from two different feedstocks (ADEME - Gaz de France).

Composition (mg/Nm^3)	Farm plant	Sewage treatment plants
H_2S	1 – 1830	15 – 4200
Dimethyl sulfide	0.1 – 40	0 – 0.3
D4 (Octamethylcyclotetrasiloxane)	0.7 – 20	0.2 – 4.0

5.3. Effects of sulfide compounds on SOFC

H_2S is the most stable sulfide compound in the working conditions of a SOFC [34]. It is very difficult to clean the system out of sulfides efficiently and economically [35]. The extent and rate of the SOFC degradation are complicated, depending on many parameters such as H_2S concentration, temperature, cell functioning voltage/current, fuel composition, anode material and cell structure (stack or single cell).

The poisoning mechanisms of hydrogen sulfide were studied for a long time in the catalytic field using conventional surface analysis techniques such as Low Energy Electron Diffraction (LEED), Electron Energy Loss Spectroscopy (EELS) or field emission microscopy [36-38]. The most possible reactions between H_2S and Ni are written as follows:

$$H_2S_{(g)} \leftrightarrow HS_{ads} + H_{(g/ads)} \rightleftharpoons S_{ads} + H_{2(g/ads)} \quad (24)$$

$$Ni + H_2S \rightleftharpoons NiS + H_2 \quad (25)$$

$$3Ni + xH_2S \rightleftharpoons Ni_3S_x + xH_2 \quad (26)$$

From Figure 6, it can be seen that the coverage of Ni surface by H_2S is proportional to the H_2S partial pressure in H_2. At low concentrations of pH_2S/pH_2 (< 100 ppm) and at temperatures above ~900°C, the adsorption of sulfur species is more favorable than the formation of nickel sulfides. At high H_2S concentrations and low temperatures, the formation of bulk nickel sulfides Ni_3S_2 is more favorable. The reaction kinetics may vary according to the different Ni crystallography planes [39].

The most realistic operating conditions for SOFC, and thus the most investigated conditions, include H_2S concentration range of 0.1-10 ppm and temperature range of 700-800°C [40]. With these conditions, according to the diagram of Figure 6, it is most likely that sulfur absorption is energetically favorable.

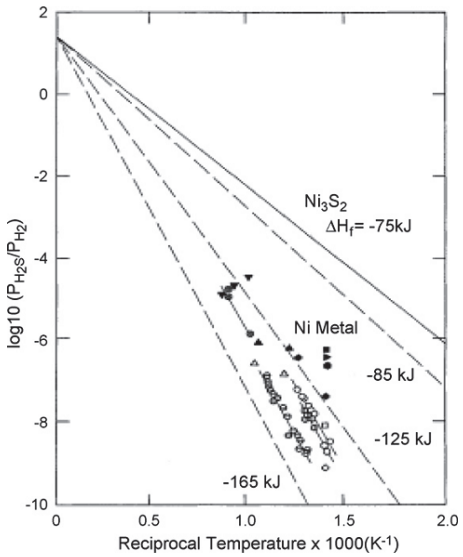

Figure 6. Coverage of Ni surface by H_2S θ at different H_2S partial pressures and temperatures (open symbols θ = 0.5-0.6; closed symbols θ = 0.8-0.9) [41].

In the aspect of cell electrochemical performance, H_2S was reported to decrease the cell power output and the cell operating voltage, while increase the total cell resistance and the anode interfacial polarization resistance [34,42-44]. By comparing the impedance size (with 0.02-15 ppm H_2S, 750-1000°C, and half-cell configuration), Matsuzaki et al. [43] revealed that (a) H_2S suffering threshold increased as the working temperature increased, e.g. from 0.05 ppm at 750°C to 2 ppm at 1000°C; (b) the degradation was more severe as the H_2S concentration increased and as the temperature decreased; (c) the recovery was much slower than the poisoning rate at lower temperatures, while the two processes were faster at higher temperatures. These trends were also observed by Brightman et al. [17] and Zha et al. [44], and can be explained by an adsorption mechanism of H_2S onto Ni, blocking the active sites for hydrogen oxidation. The unrecoverable performance was caused by a formation of Ni_3S_2 layer [45].

Cheng et al. [46] reported that with 10 ppm H_2S at 800°C, the relative increase in the total cell resistance (~impedance size) was smaller at higher cell current and lower cell voltage (see Figure 7), no matter whether the cell was tested under galvanostatic or potentiostatic conditions. So the extent of H_2S poisoning decreases with increasing cell current and decreasing cell voltage [44]. The same result was reported by Brightman et al. [17]. However, with testing conditions of 35 ppm H_2S and 1000°C, Primdahl et al [47] found no dependence of a relative increase in the anode interfacial resistance on current density up to 100 mA/cm^2. Although the time needed for the recovery was less when the current was high [48], alleviating sulfur poisoning by passing a large current is not practical since the cell power output is low [14].

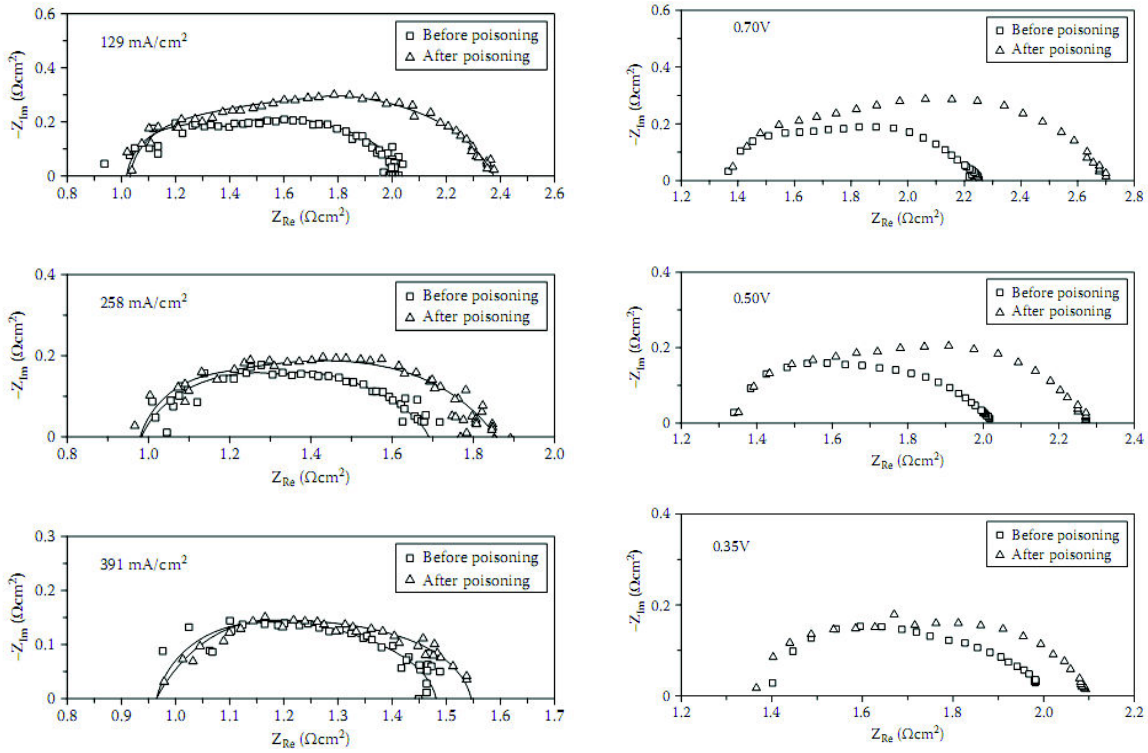

Figure 7. Impedance spectra of an electrolyte-supported cell under 10 ppm H_2S at 800°C at different currents/voltages [46].

In recent years, Raman spectroscopy has been applied to study *in situ* the properties of materials in SOFCs [49-52] given the ability to identify molecular species, and the kinetics of electrochemical processes. It has been applied successively to:

- ✓ Probe surface temperature based on temperature-dependent shifts in the F_{2g} mode of YSZ [49];
- ✓ Monitor the redox state of the YSZ electrolyte [53];
- ✓ Examine the kinetic of NiO reduction and Ni oxidation [49,54];
- ✓ Measure the formation/disappearance of graphite over a cermet anode [55].

However, for the sulfidation process, little information on the morphological and molecular changes observed by *in situ* Raman has been reported; instead it was the electric properties changes under H_2S as mentioned above that has been widely investigated. Most information has come from the group of Prof. Liu. Referent Raman spectra of different sulfides have been reported successively with compromise between experiment and theory calculation [50,56]. According to Cheng et al. [50], the Raman peaks of Ni_3S_2 disappear once the temperature increases to ~567°C due to a phase transition. This fact clearly inhibits the real time detection of Ni_3S_2 if any by Raman spectroscopy at the high operating temperatures of SOFC (700-1000°C). In the study by Cheng et al. [39], the exposure of Ni-YSZ pellets to 50 ppm H_2S at the working temperatures of ~570 °C or 800°C together with the slow cooling down (2.5 °C/min) in the same

atmosphere induced the surface morphology changes and Raman spectrum of Ni_3S_2 at lower temperatures. On the contrary, when the cooling was done fast at 70°C/min, neither morphology change nor Ni_3S_2 was observed. The authors thus concluded that the sulfide and the changes in morphology seen at low temperatures actually occurred during the slow cooling process, not at high working temperatures. This observation is expectable in the point view of thermodynamic where nickel sulfide is more stable at lower temperatures. However, there is a lack of kinetic information of the sulfidation process related to the slow/fast cooling process in H_2S.

5.4. Long-term behavior of a SOFC under H_2S

For a long-term exposure to even a small amount of H_2S (ppm level), there exist two main observations: (a) a quick saturation of sulfur poisoning after initial fast drop [14]; (b) a gradual but persistent deterioration in cell performance for several days after an initial sharp drop [44,57]. The initial sharp degradation is attributed to the dissociative chemisorption of H_2S onto Ni, which blocks the active sites for hydrogen adsorption and oxidation [44]. The subsequent slow degradation is speculated to be due to Ni surface reconstruction or S-electrolyte interactions [34]. The increase in Ni surface density induced by sulfur is considered as a general phenomenon at high temperature and high S-surface coverage [41].

6. Conclusion

The two most commonly applied anodes are Ni-YSZ and Ni-CGO because of their low cost, high conductivities and good catalytic activities. At low oxygen partial pressure and high temperature, doped ceria develops the n-type electronic conduction, so, is most suitable for intermediate temperature SOFC (below 800°C), while doped zirconia is for high temperature SOFC.

The SOFC anode polarization depends strongly on the microstructure of the anode, which in turn depends on the processing approach and the characteristics of the starting raw material, Ni content, Ni:YSZ ratio and sintering temperature. No consensus exists so far concerning the nature of the rate determining the reaction step: it may be water adsorption/desorption on YSZ, water dissociation on YSZ, surface diffusion ofOH^-_{YSZ}, hydrogen spillover to oxide ion, oxygen spillover,... Different findings from the literature may imply that the active mechanism varies with specific operating conditions and/or sample preparation methods.

The extent of H_2S-poisoning was mostly evaluated based on the cell power output or the total resistance. It was reported to vary with H_2S concentration, temperature, cell current and voltage, in which it increased with increasing H_2S concentration, decreased with increasing cell current and decreasing cell voltage; or independent of current density up to a certain value.

Since SOFC performances depend strongly on the anode microstructure, detailed investigations on the morphological changes caused by H_2S are very important. Also, in order to understand well the poisoning mechanism, it is necessary to couple electrochemical measurements with an *in situ* technique that allows the identification of H_2S-induced molecular scale changes on the anode surface.

REFERENCES

[1] A. J. Jacobson, *Chem. Mater.* **2010**, *22*, 660.
[2] N. Q. Minh, *Solid State Ionics* **2004**, *174*, 271.
[3] U. P. Muecke, K. Akiba, A. Infortuna, T. Salkus, N. V. Stus, L. J. Gauckler, *Solid State Ionics* **2008**, *178*, 1762.
[4] H. Huang, M. Nakamura, P. Su, R. Fasching, Y. Saito, F. B. Prinz, *J. Electrochem. Soc.* **2007**, *154*, B20.
[5] W. Z. Zhu, S. C. Deevi, *Mater. Sci. Eng., A* **2003**, *A362*, 228.
[6] S. McIntosh, R. J. Gorte, *Chem. Rev. (Washington, DC, U. S.)* **2004**, *104*, 4845.
[7] N. H. Menzler, F. Tietz, S. Uhlenbruck, H. P. Buchkremer, D. Stoever, *J. Mater. Sci.* **2010**, *45*, 3109.
[8] S.-D. Kim, J.-J. Lee, H. Moon, S.-H. Hyun, J. Moon, J. Kim, H.-W. Lee, *J. Power Sources* **2007**, *169*, 265.
[9] D. J. L. Brett, A. Atkinson, N. P. Brandon, S. J. Skinner, *Chem Soc Rev* **2008**, *37*, 1568.
[10] *Ceramic Materials: Processes, Properties and Applications*; J.-C. N. Philippe Boch, Ed.; ISTE Ltd, 2007.
[11] N. Bonanos, R. K. Slotwinski, B. C. H. Steele, E. P. Butler, *J Mater Sci Lett* **1984**, *3*, 245.
[12] O. Yamamoto, Y. Takeda, R. Kanno, K. Kohno, T. Kamiharai, *J Mater Sci Lett* **1989**, *8*, 198.
[13] S. P. S. Badwal, M. V. Swain, *J Mater Sci Lett* **1985**, *4*, 487.
[14] *Solid Oxide Fuel Cells: Materials Properties and Performance*; J. W. Fergus, Ed.; CRC Press, 2009.
[15] B. C. H. Steele, *Solid State Ionics* **2000**, *129*, 95.
[16] M. Mogensen, T. Lindegaard, H. U. Rud, *J. Electrochem. Soc.* **1994**, *141*, 2122.
[17] E. J. Brightman, R. Maher, D. G. Ivey, G. Offer, N. P. Brandon, *ECS Transactions* **2011**, *35*, 1407.
[18] X. Wang, N. Nakagawa, K. Kato, *J. Electrochem. Soc.* **2001**, *148*, A565.
[19] J. Mizusaki, H. Tagawa, K. Tsuneyoshi, A. Sawata, *J. Electrochem. Soc.* **1991**, *138*, 1867.
[20] A. Atkinson, S. Barnett, R. J. Gorte, J. T. Irvine, A. J. McEvoy, M. Mogensen, S. C. Singhal, J. Vohs, *Nature materials* **2004**, *3*, 17.
[21] K. Kleveland, M.-A. Einarsrud, C. R. Schmidt, S. Shamsili, S. Faaland, K. Wiik, T. Grande, *J. Am. Ceram. Soc.* **1999**, *82*, 729.
[22] M. T. Colomer, B. C. H. Steele, J. A. Kilner, *Solid State Ionics* **2002**, *147*, 41.
[23] M. Vogler, A. Bieberle-Hütter, L. Gauckler, J. Warnatz, W. G. Bessler, *Journal of The Electrochemical Society* **2009**, *156*, B663.
[24] J. Rossmeisl, W. G. Bessler, *Solid State Ionics* **2008**, *178*, 1694.
[25] T. Setoguchi, K. Okamoto, K. Eguchi, H. Arai, *Journal of The Electrochemical Society* **1992**, *139*, 2875.
[26] S. P. Jiang, S. P. S. Badwal, *Solid State Ionics* **1999**, *123*, 209.
[27] H. Koide, Y. Someya, T. Yoshida, T. Maruyama, *Solid State Ionics* **2000**, *132*, 253.
[28] C. Wen, R. Kato, H. Fukunaga, H. Ishitani, K. Yamada, *J. Electrochem. Soc.* **2000**, *147*, 2076.
[29] http://www.clarke-energy.com/chp-cogeneration/ (29/10/2013)
[30] P. V. Aravind, J. P. Ouweltjes, N. Woudstra, G. Rietveld, *Electrochem. Solid-State Lett.* **2008**, *11*, B24.
[31] M. R. Allen, A. Braithwaite, C. C. Hills, *Environ. Sci. Technol.* **1997**, *31*, 1054.

[32] E. Davoli, M. L. Gangai, L. Morselli, D. Tonelli, *Chemosphere* **2003**, *51*, 357.
[33] B. Eklund, E. P. Anderson, B. L. Walker, D. B. Burrows, *Environ. Sci. Technol.* **1998**, *32*, 2233.
[34] K. Sasaki, K. Susuki, A. Iyoshi, M. Uchimura, N. Imamura, H. Kusaba, Y. Teraoka, H. Fuchino, K. Tsujimoto, Y. Uchida, N. Jingo, *Journal of The Electrochemical Society* **2006**, *153*, A2023.
[35] J.-H. Wang, M. Liu, *J. Power Sources* **2008**, *176*, 23.
[36] C. H. Bartholomew, P. K. Agrawal, J. R. Katzer, *Adv. Catal.* **1982**, *31*, 135.
[37] C. A. Papageorgopoulos, M. Kamaratos, *Surf. Sci.* **1995**, *338*, 77.
[38] M. Blaszczyszyn, R. Blaszczyszyn, R. Meclewski, A. J. Melmed, T. E. Madey, *Surf. Sci.* **1983**, *131*, 433.
[39] Z. Cheng, M. Liu, *Solid State Ionics* **2007**, *178*, 925.
[40] E. Brightman, D. G. Ivey, D. J. L. Brett, N. P. Brandon, *Journal of Power Sources* **2011**, *196*, 7182.
[41] C. H. Bartholomew, *Applied Catalysis A: General* **2001**, *212*, 17.
[42] M. Gong, X. Liu, J. Trembly, C. Johnson, *Journal of Power Sources* **2007**, *168*, 289.
[43] Y. Matsuzaki, I. Yasuda, *Solid State Ionics* **2000**, *132*, 261.
[44] S. Zha, Z. Cheng, M. Liu, *Journal of The Electrochemical Society* **2007**, *154*, B201.
[45] V. I. B. S. J. Xia In *Solid Oxide Fuel Cells IX (SOFC-IX)*; J., S. S. C. a. M., Ed.; Pennington, NJ. USA: 2005; Vol. Materials Electrochemical Society Proceedings.
[46] Z. Cheng, S. Zha, M. Liu, *Journal of Power Sources* **2007**, *172*, 688.
[47] S. Primdahl, M. Mogensen, *J. Electrochem. Soc.* **1997**, *144*, 3409.
[48] J. Mougin, *ECS transaction* **2007**, 459.
[49] M. B. Pomfret, J. C. Owrutsky, R. A. Walker, *J Phys Chem B* **2006**, *110*, 17305.
[50] Z. Cheng, H. Abernathy, M. Liu, *J. Phys. Chem. C* **2007**, *111*, 17997.
[51] R. C. Maher, L. F. Cohen, P. Lohsoontorn, D. J. L. Brett, N. P. Brandon, *J. Phys. Chem. A* **2008**, *112*, 1497.
[52] M. B. Pomfret, J. C. Owrutsky, R. A. Walker, *Annual Review of Analytical Chemistry* **2010**, *3*, 151.
[53] M. B. Pomfret, C. Stoltz, B. Varughese, R. A. Walker, *Anal Chem* **2005**, *77*, 1791.
[54] E. Brightman, R. Maher, G. J. Offer, V. Duboviks, C. Heck, L. F. Cohen, N. P. Brandon, *Rev. Sci. Instrum.* **2012**, *83*, 053707/1.
[55] R. C. Maher, V. Duboviks, G. J. Offer, M. Kishimoto, N. P. Brandon, L. F. Cohen, *Fuel Cells (Weinheim, Ger.)* **2013**, *13*, 455.
[56] J.-H. Wang, Z. Cheng, J.-L. Bredas, M. Liu, *The Journal of Chemical Physics* **2007**, *127*, 214705.
[57] J. P. Trembly, A. I. Marquez, T. R. Ohrn, D. J. Bayless, *J. Power Sources* **2006**, *158*, 263.

Chapter 2

Experimental methods and procedures

CONTENTS

1. Introduction

Chapter 2 describes the principles of techniques employed *in situ* and *ex situ* with much emphasizes on impedance spectroscopy and Raman spectroscopy. Sample preparations and experimental procedures are also included. The effect of H_2S has first been observed on Ni pellets and Ni-CGO pellets at temperatures between 200 and 800°C. Then 500°C was chosen to investigate H_2S-induced changes in electrochemical properties and morphologies of the anode with and without polarization. Contact with pollutant has been done by passing a flow of H_2S-containing hydrogen through a home-made furnace that allows the acquisitions of optical images, *in situ* Raman and impedance spectroscopies simultaneously. *Ex situ* techniques like Scanning Electron Microscopy and X-ray Diffraction were used to confirm the results obtained *in situ*.

2. Raman spectroscopy

Raman spectra originate in the electronic polarization caused by ultraviolet or visible light. A laser is the source of a monochromatic light of frequency ν that will impose an electric field E to a sample and induce a dipole moment P following [1]:

$$E = E_o \cos(2\pi\nu t) \qquad (1)$$

$$P = \alpha E \qquad (2)$$

where E_o is the amplitude and t the time. α is the polarizability, i.e. ability of the electron cloud to distort or to polarize.

If the atoms vibrate with frequency ν_1, the nuclear displacement q and the polarisability α can be written as:

$$q = q_o \cos 2\pi\nu_1 t \qquad (3)$$

$$\alpha = \alpha_o + \left(\frac{\partial\alpha}{\partial q}\right)_o q \qquad (4)$$

where α_o is the polarizability at the equilibrium nuclear position.

Combining equations 1-4, we have:

$$P = \alpha_o E_o \cos 2\pi\nu t + \frac{1}{2}\left(\frac{\partial\alpha}{\partial q}\right)_o q_o E_o \left[\cos 2\pi(\nu+\nu_1)t + \cos 2\pi(\nu-\nu_1)t\right] \qquad (5)$$

The first term corresponds to a photon of frequency ν at the origin of the Rayleigh scattering. The second and third terms correspond to photons of frequency $\nu + \nu_1$ (anti-Stokes scattering) and $\nu - \nu_1$ (Stokes scattering). A Raman spectrum displays the scattered intensity versus the frequency shift ν_1 from the incident frequency. Very often, only the Stokes scattering is displayed. Indeed, in ordinary conditions of temperature and frequency, the Stokes spectrum intensity is much higher than that of the anti-Stokes one.

If $\left(\frac{\partial \alpha}{\partial q}\right)_o$ is zero, the Raman scattering vanishes. So the vibration is Raman active only if the polarizability changes during the vibration [1].

Any vibration of a system can be expressed as a superposition of normal vibrations in which all the nuclei move with the same frequency and in phase. For a N-atom molecule, the number of normal vibrations is 3N-6, or 3N-5 for linear molecules. However, only vibrations that satisfy the selection rules can appear in Raman spectra. Such vibrations are determined by the symmetry of the molecule. In the case of crystals, the vibrations of interest are found at the center of the Brillouin zone Γ. Their number is 3N-3, where N is the number of atoms in the primitive cell of the crystal.

Raman spectra were obtained using a Renishaw InVia spectrometer in back-scattering micro-Raman configuration. The exciting source was the green line of 514.53 nm of an Ar laser. Laser light rejection was done with dielectric filters and the photon collector was a Peltier-cooled CCD. The laser light was focused on the sample surface with a x50 objective having a long working distance of 8 mm. Depending on the experiments, a line focus mode or a point focus mode was selected, allowing the illumination of a 45 µm x 4 µm region, and 4 µm x 4 µm region, respectively, with a power of 9-11 mW on the sample. In general, the acquisition time was 10s x 10 accumulations.

3. Impedance spectroscopy

3.1. Principle of measure and analysis

The determination of the current-potential curve with a 3-electrode setup is the basis of any electrochemical study. However, this technique is insufficient for the study of complex electrochemical reactions. In the case of solid state electrochemistry, another limitation of the technique is due to the non-negligible electrical resistance of the electrolyte, which induces an ohmic drop between the reference and the working electrodes. The applied potential to the working electrode can thus be separated into three components:

$$E_w = E_0 + RI + \eta(I) \qquad (6)$$

where E_w is the applied potential, E_0 the potential of the working electrode at 0 current, RI the ohmic drop between the working and the reference electrodes when a current I passes between the counter and the working electrodes, and $\eta(I)$ the overpotential which is the only part of the potential providing informations about the kinetics of the electrode process.

In order to overcome these difficulties, electrochemical impedance spectroscopy (EIS) superimposes to the continuous applied signal a sinusoidal signal of low amplitude. If the imposed parameter is the voltage (potentiostatic methods in continuous current techniques), the imposed signal between reference and working electrodes is:

$$E = E_w + E_1\cos(\omega t) \qquad (7)$$

then the current flowing between counter and working electrodes will be of the form

$$I = I_w + I_1\cos(\omega t + \varphi) \qquad (8)$$

provided that the sinusoidal signal amplitude is low enough to consider that the E(I) characteristic is linear around (E, I). Assuming that the (E_w, I_w) point is a stationary point of the system (independent of time), the electrochemical impedance:

$$Z(\omega) = (E_1\cos(\omega t))/(I_1\cos(\omega t + \varphi)) \qquad (9)$$

will contain all the information that can be accessed with the method.

The major advantage of the technique is that it can in principle distinguish among the various processes occurring in various time domains at the electrode. Each process has its own rate, characteristic time constant, and impedance $Z(\omega)$ which brings about the polarization of the measured cell. The experimental impedance data $Z(\omega)$ can be approximated by the impedance of an equivalent electrical circuit (EEC). The EEC may consist of ideal resistors, capacitors, inductances, or distributed circuit element like constant phase element. Their physical meanings are given in Table 1.

Table 1. Impedances and physical meanings of some electrical elements [2].

Electrical element	Impedance Z	Physical interpretation
Resistor R	R	Resistance of a conductive path, a chemical/physical step, or a charge transfer.
Capacitor C	$\frac{1}{j\omega C}$	Space charge regions, specific adsorption, electrocrystallization processes.
Constant phase element CPE/Q	$\frac{1}{A\ j\omega\ ^{n}}$ or $\frac{1}{j\omega A\ ^{n}}$	Inhomogeneous properties of an electrochemical interface (due to surface defects, adsorbed species…) cause the time constant value of a process to be distributed, not a single-valued ➔ CPE is used to replace a simple ideal resistor and capacitor in parallel or series.
Inductor L	$j\omega L$	Adsorption or desorption equilibrium of surface active species on a metal [3], or hindering effect of one process to another [4].

In the ideal case, each polarization process can be modeled by a circuit made of a parallel connection of a resistance R and a capacitance C, for example:

- The conduction in semiconductors or ionic conductors can be represented by a resistor R in parallel with a capacitance C (while ohmic conduction can generally be described as a pure resistance R). The time constant RC corresponds to the inverse of the jump frequency of the mobile species. It lies in the GHz to THz region for electrons, in the MHz region for ions.
- The electrode reactions at the electrode/electrolyte interface (which can be of various kinds: diffusion-limited, concentration-limited, etc.) could be approximated by a capacitance C in parallel with a charge transfer resistance.

However, in reality, interfacial process, especially at complex geometries, always shows a distribution of time constant (i.e. without discrete value of time constant). In Nyquist representation, the characteristic semicircle arc, instead of being centered on the real axis, is depressed with an angle (1-α)π/2. The constant phase elements were thus introduced to model these non-ideal behaviors. The equation of a resistor in parallel with a constant phase element is

$$Z = \frac{R}{1+RA\ j\omega\ ^{\alpha}} \qquad (10)$$

From a physical point of view, the imaginary part of the denominator should be without dimension. Because of the α power, A is not any more a capacitance (instead it reflects the distributed nature of the response). Moreover, two circuits modeled with the same equation, but different values of α, cannot be compared, because the two A values are not of the same unit. Therefore, in this work, we preferred to use a "depressed parallel RC" with the impedance:

$$Z = \frac{R}{1+\ j\omega RC\ ^{\alpha}} = \frac{R}{1+\ j\frac{\omega}{\omega_0}\ ^{\alpha}} \qquad (11)$$

which is physically acceptable and introduces gently a real resistance R and a real capacitance $C = 1/(R\omega_0)$ that can both be compared between experiments, whatever the parameter α.

In principle, the impedance of any model can be calculated with the help of a Laplace transform, provided that the two conditions: stationarity of the measurement point and linearity of the I(V) characteristic are fulfilled.

It is a prerequisite to understand as much as possible the number of electrochemical, chemical and physical processes that contribute to polarization of the system in order to choose an appropriate equivalent circuit, since there are many circuits that can produce the same polarization property.

3.2. The capacitive double layer

An attempt to determine the capacitance of the double layer at the interface between porous platinum electrodes and yttria-stabilized zirconia has been made by Robertson et al. [5], in which it was extracted from the short-time exponential decay of the current. The values obtained (0.23 to 1.24 μF/cm^2 at 555-695°C) were compared with predictions of the Gouy-Chapman-Stern model to see if they were physically reasonable. However, they were an order of magnitude higher than the capacitance of the compact double layer formed by adsorption of oxygen ions at the interface. The assignment of these values to that of the diffuse layer of mobile ionic species inside zirconia electrolyte although resulted in reasonable Debye length values, theirs strong temperature dependence was unexplainable.

Another description of the double layer capacitance is based on a surface concentration of charged defects different to that observed in the bulk of the electrolyte [6]. Hendriks et al [7] have calculated and measured values in the order of 100 μF/cm^2 for tetragonal zirconia and cubic zirconia between 500 and 800°C.

Kek et al. [8] proposed the values of 10-20 μF/cm^2 to be characteristic for compact double layer, with 20 μm/cm^2 corresponds with d= 0.4 nm, typical thickness of a space charge region.

A capacitance is used also as a reflection of kinetics of adsorption process at low frequencies, since at high frequencies, the adsorption/desorption process is not fast enough to have any effect, and the surface coverage does not change [9].

3.3. Origin of inductive elements

A high frequency inductive element often appears, due to the external circuitry. Indeed, a single loop very often appears due to the current-carrying wires. At low frequency, adsorption or desorption equilibria of surface active species on a metal surface have been reported as a possible source of induction in impedance spectra [3]. The induction produces negative impedance magnitudes at high and low frequencies, positive phase angles and negative impedance magnitudes.

Another cause may be a hindering effect of one process to another. As one or more of the individual steps in a complex reaction is significantly slower than the others, it restricts how fast electrical double layer composition changes in response to polarizing voltage, thus induces an inductive loop [4].

3.4. Equipment

The impedance spectra were recorded with an Autolab PGSTAT302N. The applied frequency range was 100 kHz - 10 mHz with 10 points/decade, and an AC voltage amplitude of 10 mV.

4. Scanning Electron Microscope (SEM)

The SEM produces images by illuminating the sample with electrons instead of light. When the electron beam hits the sample, it induces other emissions of electrons (including primary backscattered electrons, secondary electrons, Auger electrons) and X-rays which are then collected by detectors to create images.

Secondary-electron images (SE) are created from secondary electrons with low energy (smaller than 50 eV) that are rejected from the k-orbitals of the specimen. The brightness of the signal depends on the number of SEs reaching the detector. Since more electrons are emitted from steep surfaces and edges, they tend to be brighter than flat surfaces, which results in images with a three-dimensional appearance. With in-lens detector, images with high contrast can be obtained in particular at low voltages and small working distances. The in-lens detector images differences in the work function on the sample (the higher the work function is, the less electrons are emitted, the darker the image), while the conventional detector images the topographic information dominantly [10].

Backscattered-electron images (BSE) are created from elastic scattered electrons with high energy. Heavy elements backscatter electrons more strongly than light elements, and thus appear brighter in the image. BSE images reveal the differences in chemical composition (average atomic number) in the sample.

Energy Dispersive X-ray analysis (EDS/EDX/XEDS/EDAX) is a technique used to identify the elemental composition of a sample and is used in conjunction with SEM. The photons X emitted possess energies and wavelengths characteristics of each element. Thus by analyzing the emitted x-rays, the composition of the sample can be determined. EDS is a powerful tool for microanalysis of elemental constituents.

In SEM, samples must be electrically conductive, at least at the surface, and electrically grounded to prevent the accumulation of the electrostatic charge at the surface. The charging of the sample may cause scanning faults and image artifacts.

The microscope used in this study is a FEG ZEISS Ultra 55.

5. X-ray Diffraction (XRD)

When X-rays interact with a crystalline phase and the Bragg's law is satisfied, its atomic planes will cause the incident beam to interfere constructively with one another as they leave the crystal. The diffracted beams will create a diffraction pattern which allows the determination of lattice parameters (volume of unit cell, interplanar spacing), as well as phase chemical nature.

The X-ray diffractometer used here is an X'Pert Pro MPD PANalytical. X-ray tube is Cu type with an average Kα of 1.5418 Å (from $K\alpha_1$ of 1.5406 Å and $K\alpha_2$ of 1.5450 Å). The goniometer is theta:theta configuration. 2θ is between 20° and 120°, with a pace of 0.017° and acquisition time of ~1 hour for a diffractogram.

6. Experiments

6.1. Gas flow control

A gaseous flow was delivered to the sample by a gas supply system (Figure 1) fed by bottles of Ar (Messer), 3%H_2/Ar (Messer), 500 ppm H_2S/3%H_2/Ar (Air Liquide) and O_2 (Messer). The flow rates are controlled by mass flow controllers (Brooks, 5850TR) with flow ranges of 40 sccm, 100 sccm and 300 sccm.

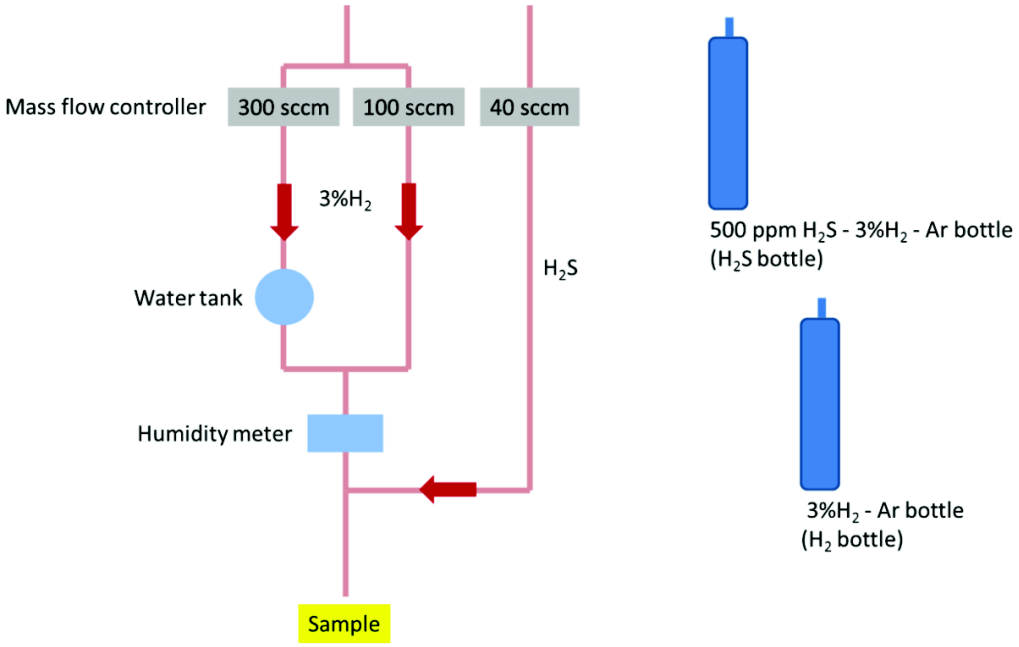

Figure 1. The gas delivery system with the two main gas bottles

If all measurements were carried out at open circuit potential, there would be no need for a humid gas. However, since a current has to go through the cell, it is necessary to feed the counter electrode with a gas containing a reducible component. This component will be the water molecules of the gas.

Water vapor is controlled by the reservoir temperature. The water percentage in the flow is then measured by a humidity & temperature transmitter HMT 337 (Vaisala, Finland) (Figure 1). When the temperature is set at 39°C, with Ar flowing through the 300 sccm line, H_2O is measured to be ~5% (volume) and is independent of flow rate. Since it takes a long time for the tank temperature to be stable, a lower water content of 3% is obtained by passing gas through 100 sccm line simultaneously, not by changing the reservoir temperature. All the gas lines are wound with elastic heating threads to prevent water condensation. H_2S was sent only through 40 sccm line in order not to contaminate other parts in the gas supply system. The 500 ppm H_2S-containing gas is diluted by 3%H_2/Ar to obtain the desired gas compositions.

6.2. Home-made *in situ* cell (LEPMI)

Figure 2 schemes the home-made round furnace designed specially to acquire optical images, Raman spectra, and impedance spectra at the same time. The sample is placed on a ceramic disk which in turn is placed on a steel base. The base is heated by two halogen lamps with a ramp rate of 130°C/min. Two thermocouples positioned inside the base and near the sample surface allow

the temperature readings. The furnace also contains three electrical terminators in order to connect the sample with a potentiostat for electrical measurements.

Before any new experiment, especially after one with pollutants, the furnace was cleansed by 20%O_2 in Ar at 750°C for 1 hour in order to oxidize any trace of H_2S, carbon, as well as others undesired impurities.

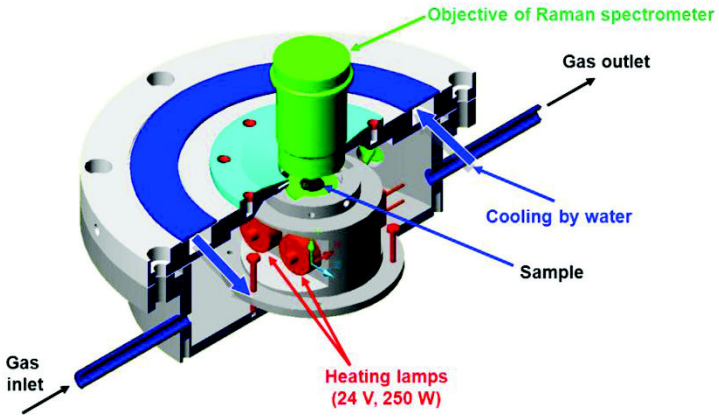

Figure 2. Home-made *in situ* cell allowing Raman, impedance and optical measurements at various temperatures in controlled atmosphere

Figure 3 exhibits the set up combining Raman, optical images and electrochemical impedance investigations.

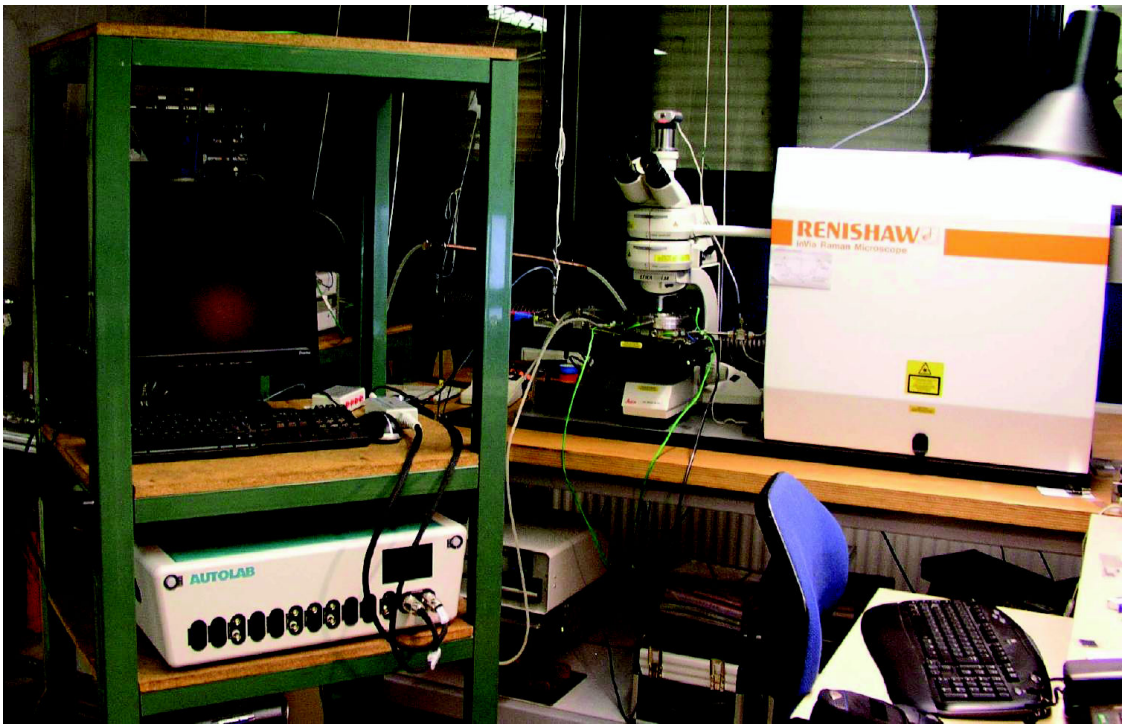

Figure 3. Combination of Raman, optical images and impedance measurements

6.3. Investigations of H_2S and Ni reaction

6.3.1. Ni pellet making

The commercial powder NiO (Alfa Aesar) was pressed uniaxially at 29000 N/cm^2 (290 MPa) into pellets of 7.85 mm in diameter and 0.76 mm thickness. They were sintered lightly in air at 800°C during 3 hours. The heating and cooling were done at 60°C/min. The pellets were then reduced at 715°C in 3%H_2/Ar during 9 hours. The completion of the reduction was evaluated by a Thermo Gravimetric Analysis (TGA), as shown in Figure 4. The reduction almost ends after the first 3.5 hours with 75% NiO being reduced. As the rate of reduction becomes very slow after that, the reduction of NiO in all the experiments was all conducted in 3.5 hours at 715°C in 3%H_2/Ar.

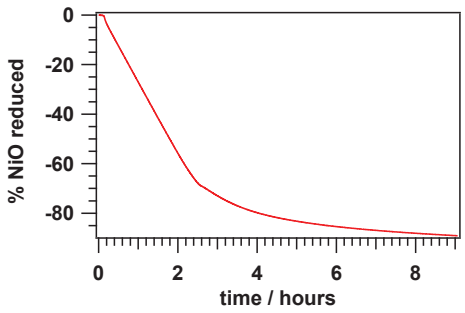

Figure 4. TGA curve showing the mass loss of NiO due to the reduction in 3%H_2 at 715°C

6.3.2. Contact with H_2S at a working temperature

The sample was heated fast (120°C/min) to the working temperature in 33 sccm of 3%H_2/Ar. After 30 minutes waiting at the working temperature, the gas was switched to 300 ppm H_2S/3%H_2/3%H_2O/Ar with the same flow rate. Raman spectra and optical images were recorded after regular time interval. After a determined period, the gas was changed into Ar to clean the system off H_2S in 1 hour. Then, the system was cooled down fast to 50°C in Ar in about 50 minutes. Much care was taken into account to assure that contact with H_2S happened only at the working temperature by purging the whole system with high flow rate of Ar before decreasing the temperature very fast to 50°C.

Table 2 summarizes the main parameters of the series of experiments between Ni pellet and H_2S.

Table 2. Summary of experiments on Ni pellet

H_2S in 3%H_2/Ar	T (°C)	H_2S exposure time hh:mm	Ar exposure time hh:mm
300 ppm	200°C	24:00	15:40
	300°C	63:00	21:38
	500°C	61:00	6:00
	800°C	18:00	1:00

6.3.3. Contact with H_2S during the heating process

The heating process was done with 2°C/min. The heating from 50°C to 800°C was done in 300 ppm H_2S in 3%H_2/Ar. Raman spectra, together with optical images, were taken every 100°C. After 10 minutes at 800°C, the gas was changed to Ar. The purging in Ar was done in 5 hours. The cooling was done very fast in order to avoid any further reaction between anode and H_2S trace if any as mentioned by Cheng et al. [11].

6.4. Investigations of H_2S and Ni-CGO reaction

6.4.1. Powder mixing

The powder NiO/CGO (supplied by CEA) was mixed for 20 hours in ethanol with zirconia balls in order to break down the big agglomerates. Then the mixture was put in an ultrasonic bath at 65°C to remove ethanol and to mix the two components. At last, it was dried in an oven at 75°C.

Figure 5 shows that the grinding is effective to reduce particle sizes. Smaller agglomerates will form more homogeneous distribution among phases.

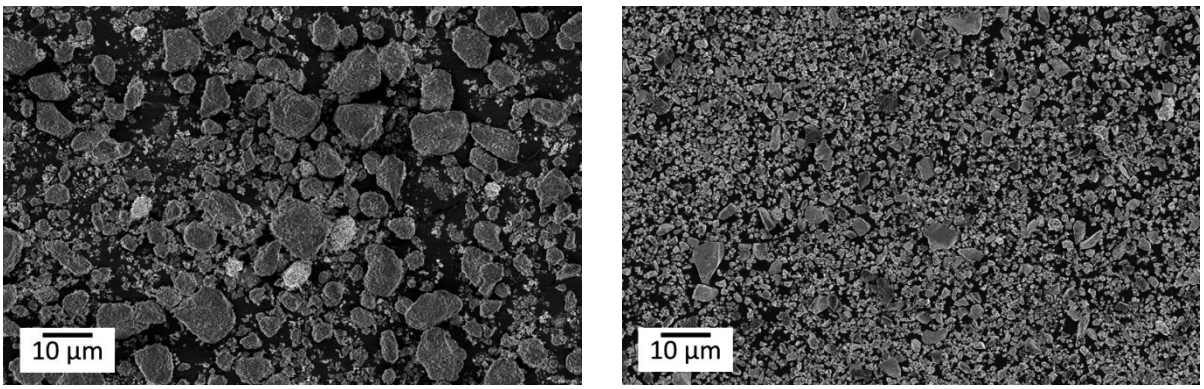

Figure 5: SEM images of NiO/CGO powder before and after grinding

6.4.2. Ni-CGO pellet making

The powder NiO-CGO was pressed first uniaxially and then isostatically at 1950 N/cm^2 (19.5 MPa). The pressure used was restricted to the value as low as possible to ensure a porous and homogeneous structure of the pellet. The pellet was then sintered slightly in air at 715°C for 1 hour with heating and cooling rates of 2°C/min. The pellet reduction was conducted in 3%H_2/Ar at 715°C for 3 hour. The heating and cooling were done fast in 5 minutes and 50 minutes respectively. Some physical parameters of Ni-CGO pellet are given in Table 3.

Table 3. Physical parameters of the Ni-CGO pellets

	Before reduction	After reduction
Mass/ g	0.03	0.02
Diameter/ mm	3.74	3.59
Thickness/ mm	0.87	0.85
Volume/ cm^3	0.01	0.01
Density/ g/cm^3	2.84	2.80

6.4.3. Ni-CGO pellet characterizations

6.4.3.1. Raman spectrum of doped CeO_2 from literature

CeO_2 has a fluorite structure with one allowed F_{2g} Raman mode which is the symmetric breathing mode of the oxygen atoms around each cation. The Raman shift is 465 cm^{-1}.

In CeO_2 doped with trivalent lanthanide cation of $Ce_{1-x}Re_xO_{2-y}$ (Re= La, Nd, Eu, Gd), the 465 cm^{-1} band becomes asymmetric with a lower frequency tail, and two bands appear at about 560 and 600 cm^{-1}. The 560 cm^{-1} band is attributed to oxygen vacancies introduced by the doping [12-14]. The 600 cm^{-1} band is either attributed to the intrinsic vacancies which becomes clear in a nanocrystalline pure cerine oxide [15,16], or to the presence of lower valence ions (Gd^{3+}, Ce^{3+}) at the place of Ce^{4+} in the non-vacancy environment [14,17].

6.4.3.2. Raman spectra of Ni-CGO

Figure 6 presents the Raman spectra obtained from pellets of NiO, NiO-CGO, and Ni-CGO. After 3 hours in 3%H_2/Ar at 715°C, no peaks of NiO can be seen on the surface of Ni-CGO pellet because of the reduction of NiO to Ni.

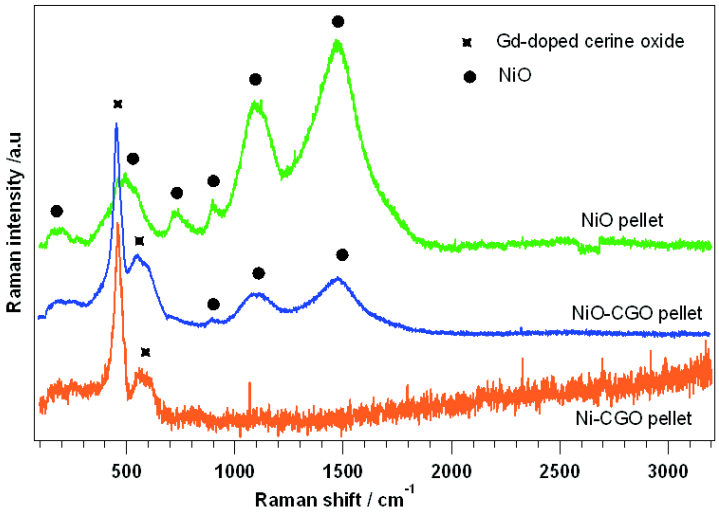

Figure 6. Raman spectra taken at 50°C in Ar of NiO, NiO-CGO and Ni-CGO pellets

6.4.3.3. Morphology of Ni-CGO pellet

The morphology of the pellet is displayed in Figure 7. EDS chemical analysis has revealed that the white clusters of very small particles are CGO, while the much bigger dark particles are Ni. The two phases are mixed well, with the CGO particles of ~50 nm surrounding the Ni particles/agglomerates of about 0.5–1 μm. There is no observable difference among the surface, the bottom and the cross-section.

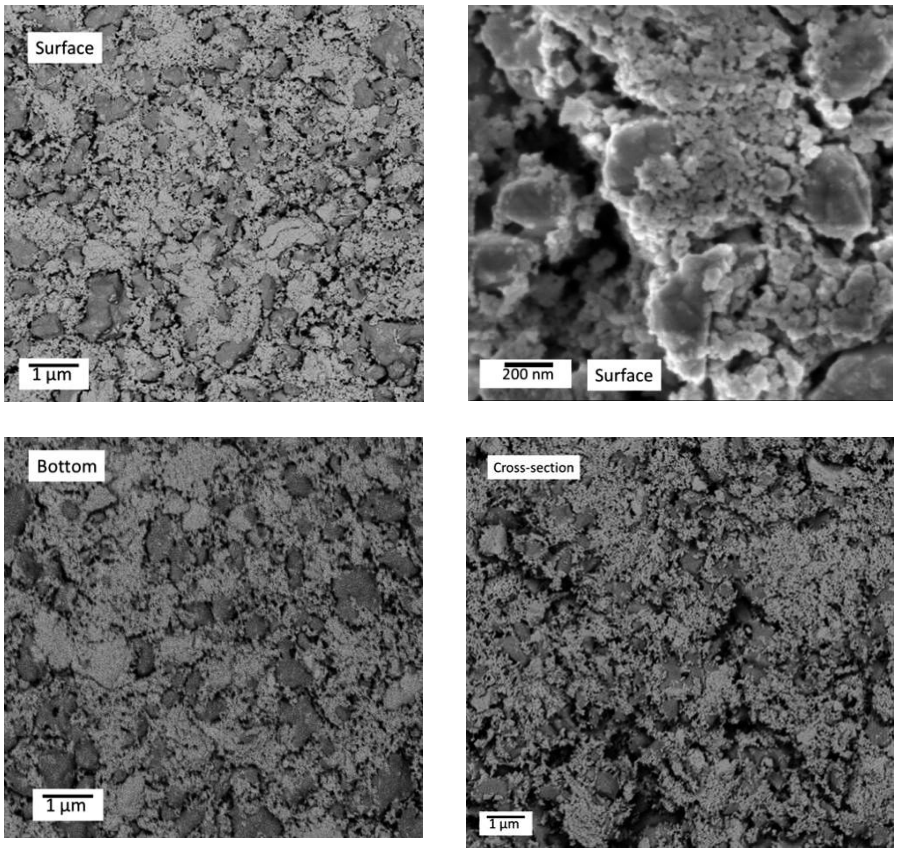

Figure 7 : SEM images showing the morphology of Ni/CGO pellet

6.4.4. Investigation procedure for H_2S and Ni-CGO reaction

The same procedure like that of Ni was applied to Ni-CGO pellet (see part 6.3.2). A summary of all the experiments is given in Table 4.

Table 4. Summary of experiments on Ni-CGO pellet

x ppm H_2S in 3%H_2/Ar	T°C	Exposure time to H_2S
500 ppm	715°C	14 h
	715°C	17.7 h
	750°C	3 h
	770°C	40 min
	780°C	15 min
	790°C	15 min
	500°C	12.3 h
	200°C	11.5 h

6.5. Half-cell Ni-YSZ/YSZ

6.5.1. Sample construction

To study only the anodic reaction, NiO-YSZ/YSZ half-cells (Kerafol) were constructed in a 3-electrode measurement configuration. Cathode and reference electrodes were added onto commercial half-cell by Pt paste, Pt mesh and wire (Alfa Aesar).

To make the counter electrode (CE), Pt paste was painted onto the YSZ electrolyte on the side opposite to the anode. The painted area is marked by dash line in Figure 8. Two layers of Pt were applied to obtain a sufficient amount of Pt. Each layer was dried naturally at 57°C. Then, the Pt cathode was sintered slowly with 2°C/min from room temperature to 900°C in air, with 1 hour waiting successively at 100°C, 200°C, 300°C, 400°C, 500°C, and 900°C. The temperature then decreased with 5°C/min to room temperature.

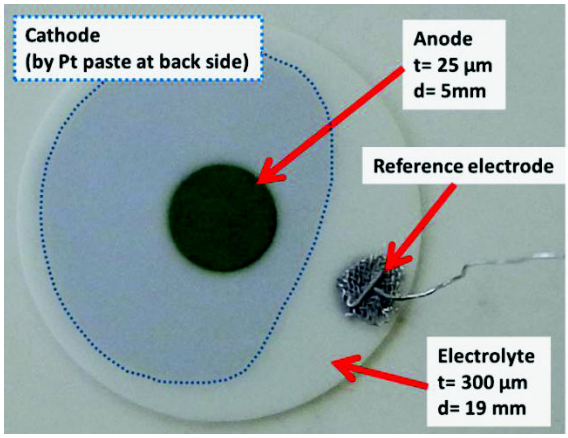

Figure 8. Half-cell added with Pt cathode and Pt reference electrode (t = thickness, d = diameter)

For the reference electrode (RE), two layers of Pt paste were painted in the form of a small dot onto YSZ electrolyte on the anode side and were dried naturally. Next, the current collector was fixed to RE with the Pt paste (see Figure 8). More Pt paste was added if necessary to fix well the Pt mesh and wire. After being dried naturally, the Pt RE was sintered in the same way as the CE.

6.5.2. Sample installation

The interior of the *in situ* home-made furnace is shown in Figure 9A. The grooves in the ceramic substrate act as gas supplying channel to cathode side and as electrical insulator. The thermocouple helps to measure gaseous temperature near the half-cell. A large Pt mesh serves as cathode current collector.

The sample was positioned as in Figure 9B and 9C. A Pt current collector is pressed to the anode by a three-hole ceramic piece. These holes allow contact between fuel and anode, and allow the illumination of the anode surface in *in situ* Raman and optical measurements. A voltmeter was used to verify the electrical contacts to prevent any short circuit in the system.

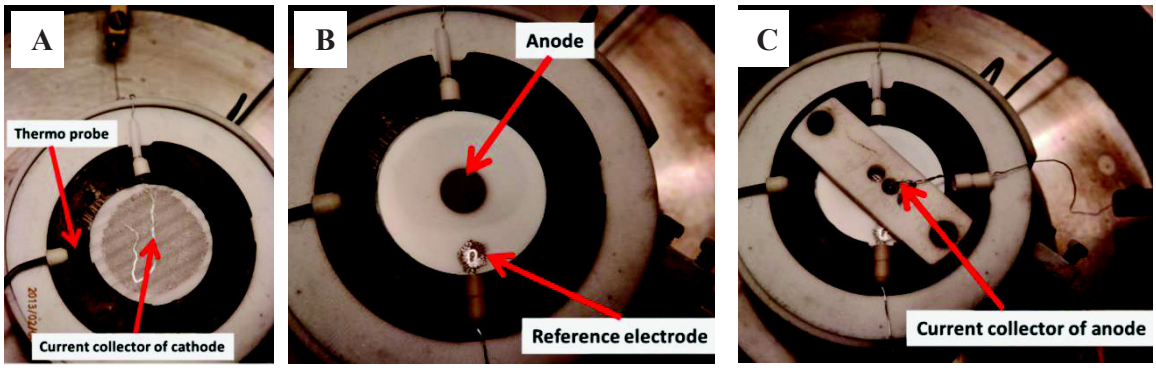

Figure 9. EIS set-up measurement with 3-electrode configuration

6.5.3. Experimental procedure

The sample was heated to 715°C in Ar with 50°C/30 minutes. Then the gas was switched to 3%H_2 /3%H_2O/Ar to start pre-treatment (stage A). During this stage, NiO was reduced to Ni. Impedance spectra (IS) were recorded at Open Circuit Potential (OCP), 100, 300, and 500 mV/ref every hour. The standby condition (when there was no impedance measurement) was at OCP and 715°C. Cycles of polarization at these voltages were repeated until the spectra attained stable forms. Then the sample was back to the working temperature of 500°C. The pre-treatment (stage B) at 500°C was done as with 715°C.

After stage B, the sample was fixed permanently at one value of polarization voltage during the whole experiment, either at OCP or 500 mV/ref. The polarizing voltage was fixed in order to prevent the activation phenomenon observed, i.e. the decrease/increase in cell resistance when polarization starts/stops [18,19]. Cell performance in clean fuel was monitored during stage C, and was compared with performance in polluted fuel in stage D. In stage E, pollutant was removed from the gas flow to test the recovery capacity of the sample.

For all the experiments, the total flow rates were kept constant at 97.3 sccm. Table 5 summarizes the purpose of each stage together with measuring parameters and time.

Table 5. Impedance measuring procedure

(in red: standby voltage, in bold black: applied voltage to measure)

A	B	C	D	E
Pretreatment 715°C	Pretreatment 500°C	Operation w/o pollutan	Attack of pollutan	Operation after pollutant removal
715°C 3%H_2/3%H_2O/Ar	500°C 3%H_2/3%H_2O/Ar	500°C 3%H_2/3%H_2O/Ar	500°C 3%H_2/3%H_2O/Ar + 200 ppm H_2S	500°C 3%H_2/3%H_2O/Ar
OCP	OCP	OCP	OCP	OCP
OCP-500mV	**OCP-500mV**	**OCP**	**OCP + *in situ* Raman**	**OCP**
43.8 h	19.7 h	191.3 h	48.5 h	58.4 h
715°C 3%H_2/3%H_2O/Ar	500°C 3%H_2/3%H_2O/Ar	500°C 3%H_2/3%H_2O/Ar	500°C 3%H_2/3%H_2O/Ar + 200 ppm H_2S	500°C 3%H_2/3%H_2O/Ar
OCP	OCP	500 mV	500 mV	OCP
OCP-500mV	**OCP-500mV**	**500 mV**	**500 mV + *in situ* Raman**	**500mV**
15.5 h	7.8 h	156.1 h	53.8 h	57.5 h

A,B - *to activate the anode*

- *to obtain stable forms of impedance spectra (IS) which can characterize the half-cell*

C *to find down aging effect in clean fuel*

D *to study changes in electrochemical processes caused by pollutants*

E *to reveal the recovery capacity of the half-cell when the pollutants are removed*

References

[1] *Infrared and Raman spectra of Inorganic and Coordination Compounds*; 4th ed.; K. Nakamoto, Ed.; John Wiley and Sons, 1986.
[2] *Impedance Spectroscopy Theory, Experiment, and Applications*; Second ed.; J. R. M. Evgenij Barsoukov, Ed.; Wiley-Interscience.
[3] J. N. Murray, P. J. Moran, E. Gileadi, *Corrosion (Houston)* **1988**, *44*, 533.
[4] *An Introduction to Electrochemical Corrosion Testing for Practicing Engineers and Scientists* W. S. Tait, Ed.; Pair O'Docs Publications, 1994.
[5] N. L. Robertson, J. N. Michaels, *Journal of The Electrochemical Society* **1991**, *138*, 1494.
[6] R. B. Poeppel, J. M. Blakely, *Surface Sci.* **1969**, *15*, 507.
[7] M. G. H. M. Hendriks, J. E. ten Elshof, H. J. M. Bouwmeester, H. Verweij, *Solid State Ionics* **2002**, *146*, 211.
[8] D. Kek, M. Mogensen, S. Pejovnik, *J. Electrochem. Soc.* **2001**, *148*, A878.
[9] *Electrochemical Impedance and Noise*; R. Cottis, S. Turgoose, Eds.; NACE International: Houston, 1999.
[10] http://www.microscopy.ethz.ch/se-detectors.htm (7 May/2012)
[11] Z. Cheng, M. Liu, *Solid State Ionics* **2007**, *178*, 925.
[12] J. R. McBride, K. C. Hass, B. D. Poindexter, W. H. Weber, *J. Appl. Phys.* **1994**, *76*, 2435.
[13] A. Banerji, V. Grover, V. Sathe, S. K. Deb, A. K. Tyagi, *Solid State Commun.* **2009**, *149*, 1689.
[14] A. Nakajima, A. Yoshihara, M. Ishigame, *Phys. Rev. B: Condens. Matter* **1994**, *50*, 13297.
[15] S. Askrabic, Z. D. Dohcevic-Mitrovic, M. Radovic, M. Scepanovic, Z. V. Popovic, *J. Raman Spectrosc.* **2009**, *40*, 650.
[16] S. Askrabic, Z. Dohcevic-Mitrovic, A. Kremenovic, N. Lazarevic, V. Kahlenberg, Z. V. Popovic, *J. Raman Spectrosc.* **2012**, *43*, 76.
[17] T. Taniguchi, T. Watanabe, N. Sugiyama, A. K. Subramani, H. Wagata, N. Matsushita, M. Yoshimura, *J. Phys. Chem. C* **2009**, *113*, 19789.
[18] R. J. Aaberg, R. Tunold, M. Mogensen, R. W. Berg, R. Odegard, *J. Electrochem. Soc.* **1998**, *145*, 2244.
[19] K. Vels Jensen, S. Primdahl, I. Chorkendorff, M. Mogensen, *Solid State Ionics* **2001**, *144*, 197.

Chapter 3

Effects of H_2S on anode materials

CONTENTS

1. Introduction

It is very essential to monitor the chemical composition and the morphology evolutions of a material *in situ* in order to find a link with its performances. However, a real time investigation is not simple because of the high functioning temperatures of a SOFC, i.e. 1000°C for traditional SOFC and 500-800°C for intermediate temperature SOFC [1].

In situ Raman spectroscopy has been applied successfully to probe the oxidation/reduction kinetics of Ni/NiO, and carbon formation/disappearance at the surface of a Ni-YSZ pellet at 715°C [2]. However, for the sulfidation process, little information has been obtained. No sulfides could be detected at elevated temperatures (>500°C). The formation of nickel sulfide and the morphology changes observed in *operando* or *ex situ* conditions were reported to happen in fact during the slow cooling process [3].

This chapter is thus dedicated to the use of *in situ* Raman spectroscopy and *in situ* optical imagery to study the sulfidation kinetics and the morphological changes of pure Ni and Ni-CGO upon being exposed to H_2S at various temperatures (from 200 to 800°C). The extent of poisoning when H_2S is present during the heating process was also evaluated. The ability to recover polluted anode materials was included as well. *Ex situ* analyses by X-Ray Diffraction (XRD) and Scanning Electron Microscope (SEM) are presented, showing detailed information about the morphological changes and the spatial distribution of the sulphur species.

2. Raman spectra of nickel sulfide compounds

Nickel sulfides exist in numerous defined compounds like NiS, NiS_2, Ni_3S_2, Ni_3S_4, Ni_9S_8 (see Figure 1)... Millerite (NiS), heazlewoodite (Ni_3S_2), polydymite (Ni_3S_4) and vaesite (NiS_2) are the most common minerals. Nickel (II) monosulfide NiS has two phases: β-NiS (or millerite, space group R3m) which is stable at low temperatures (below 380°C) and α-NiS (group $P6_3/mmc$) stable at higher temperatures [4,5]. Ni_3S_2 exists in two phases: low-temperature rhombohedral (or heazlewoodite) (below ~ 570°C) and high-temperature cubic phase. The rhombohedral phase has six Raman-active bands, while the cubic phase has only one due to its antifluorite structure [6].

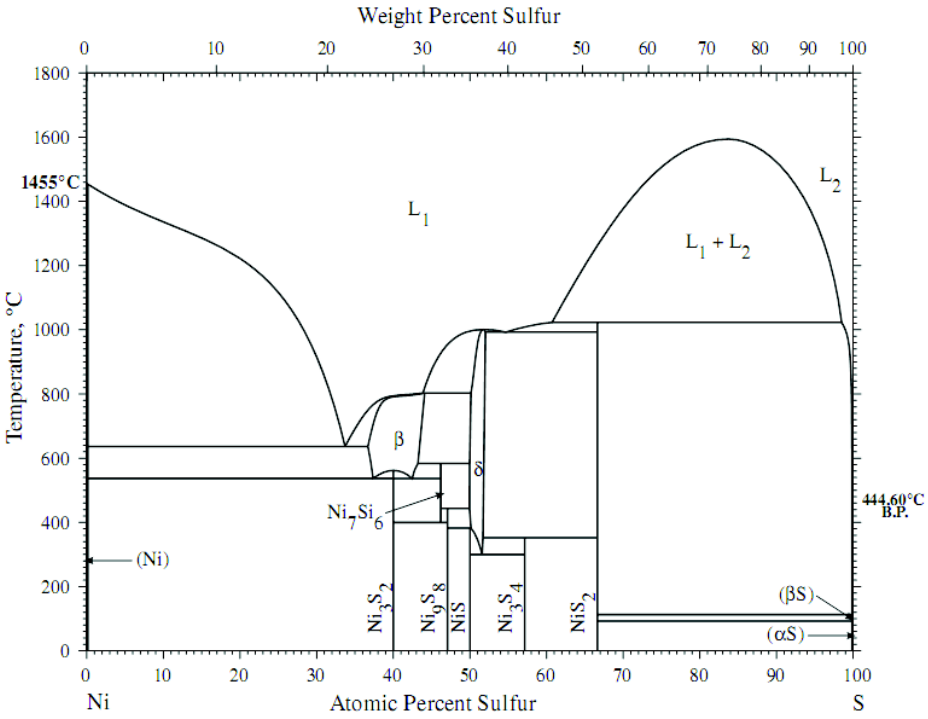

Figure 1. Ni-S phase diagram [7]

2.1. Ni_3S_2

A review by Cheng et al. [6] disclosed a huge inconsistence in the Raman spectrum of Ni_3S_2 obtained from different preparation methods. The authors pointed out that it is difficult to obtain high purity Ni_3S_2 with the right phase by conventional synthesis ways, e.g. solid state reaction. Instead they obtained Ni_3S_2 by exposing Ni pellet to a flow of H_2S at 440°C and reported the Raman spectrum of heazlewoodite Ni_3S_2 as in Figure 2. The same Raman shifts were obtained by density functional theory calculations [8].

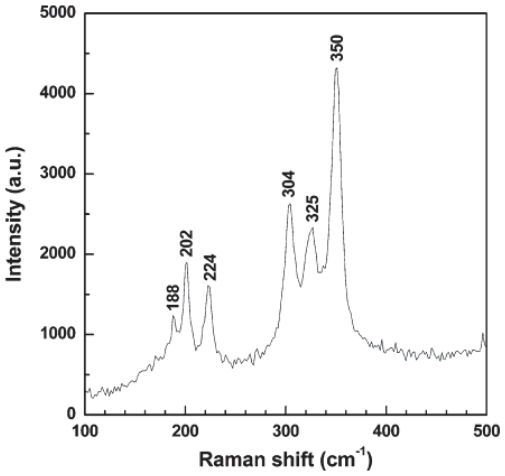

Figure 2. Room temperature Raman spectrum of Ni_3S_2 [6]

At high temperatures, the rhombohedral phase transforms to cubic phase. In the structure proposed by Cheng et al. [6], a single Raman band is expected. These authors observed a broad band at ~320 cm^{-1} at 567°C. However this band is broad and weak, and cannot be used to characterize Ni_3S_2 at high temperature [6].

2.2. NiS

Figure 3 displays the Raman spectra of NiS obtained from different preparation methods [3,5,9]. All the spectra are in agreement in terms of Raman shift but not in terms of relative intensity. This can be explained by different levels of crystallinity and/or different preferred crystal orientations.

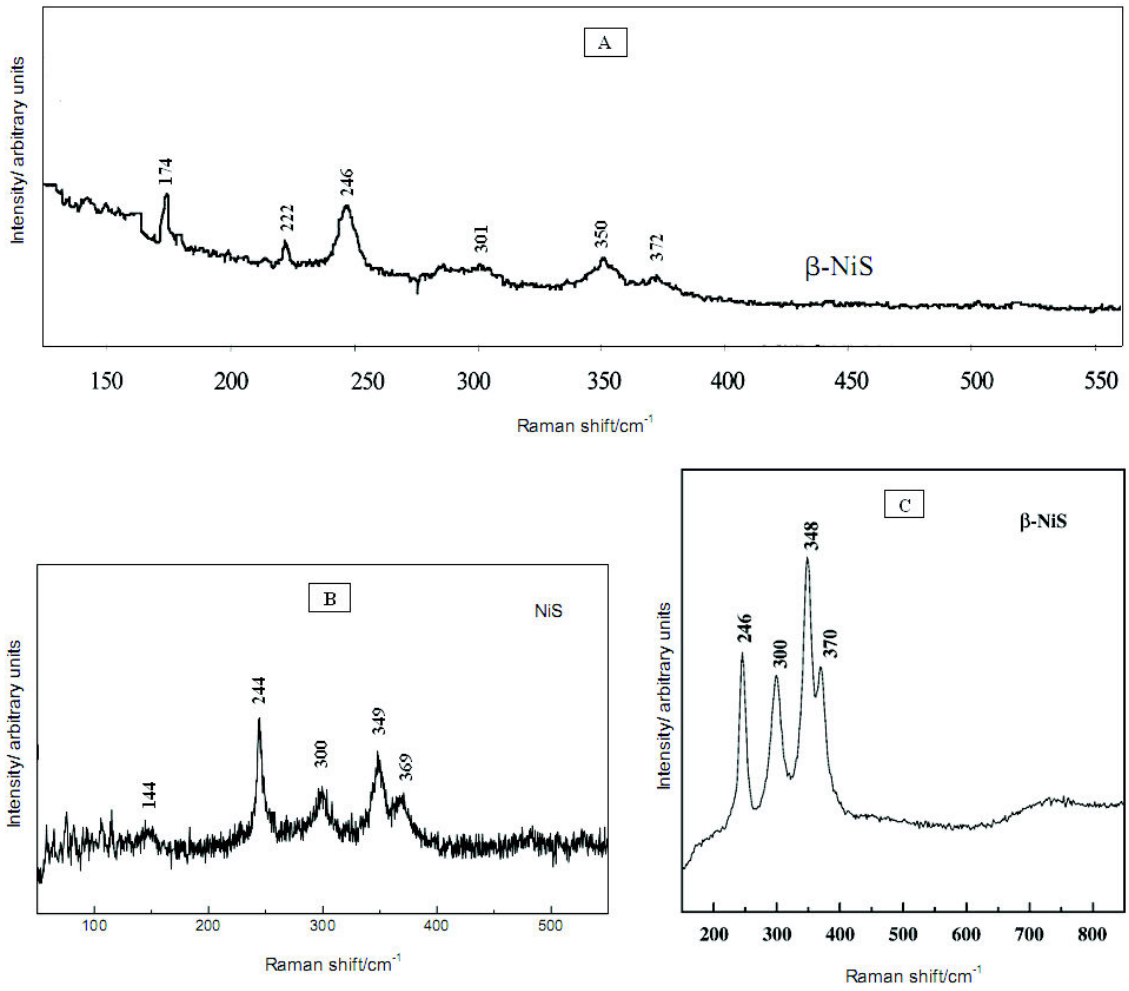

Figure 3. Room temperature Raman spectra of NiS: A) from commercial powder of millerite [5]; B) from solvothermal reaction [9] and C) from the reaction between Ni_{pellet} and H_2S_{gas} [3]

2.3. Thermal decomposition of NiS and Ni_3S_2

Since SOFCs operate at high temperatures, it is necessary to know how the sulfide compounds behave at such temperatures. A phase diagram though reports the thermodynamically stable phases under various conditions, it is valid for closed systems, while a SOFC is an open system with a large gas flow, allowing a mass exchange between the inside and the outside of the cell.

2.3.1. NiS

NiS formed at the surface of a Ni pellet was heated in flowing Ar to 600°C. Raman spectra of a 45 x 4 μm^2 area surface were recorded every 100°C during the heating/cooling processes. Figure 4 reveals that the spectra from 50 to 300°C are characteristic of NiS. From 400°C and above, they are characteristic of Ni_3S_2. On cooling from 600°C, only Ni_3S_2 peaks are observed. It is clear that a decomposition of NiS to Ni_3S_2 happened above 300°C. The reaction is fast and irreversible. It can be written as proposed by Kiuchi et al. [10]

$$3NiS \rightarrow Ni_3S_2 + 1/2S_2\ (g) \qquad (1)$$

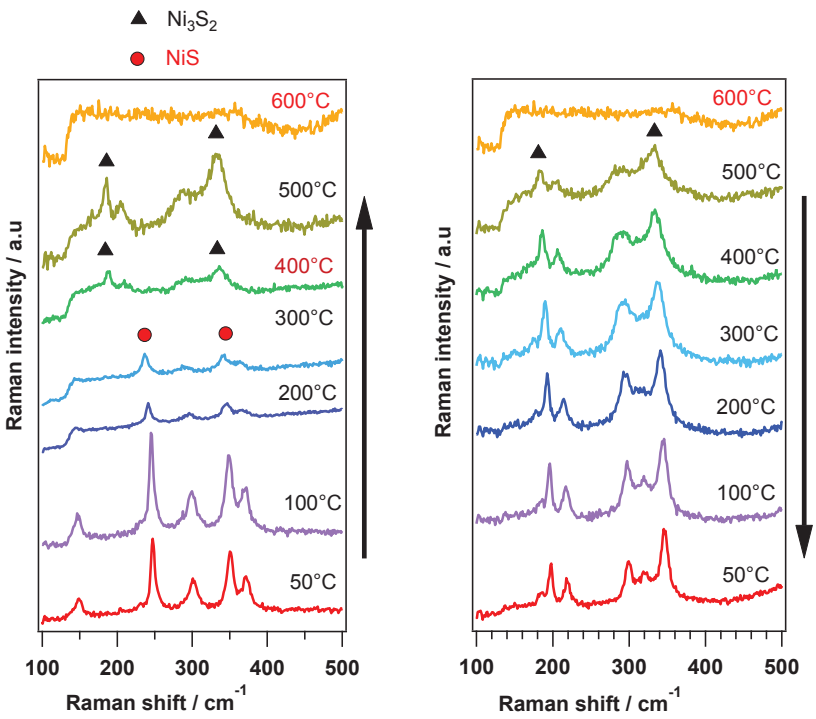

Figure 4. Raman spectra with chemical evolutions of NiS formed at the surface of a Ni pellet recorded at various temperatures in flowing Ar

2.3.2. Ni_3S_2

Ni_3S_2 formed at the surface of a Ni-CGO pellet was heated in flowing Ar to 715°C. The spectra obtained during the heating/cooling processes are shown in Figure 5. The treatment to 715°C seems not to decompose Ni_3S_2.

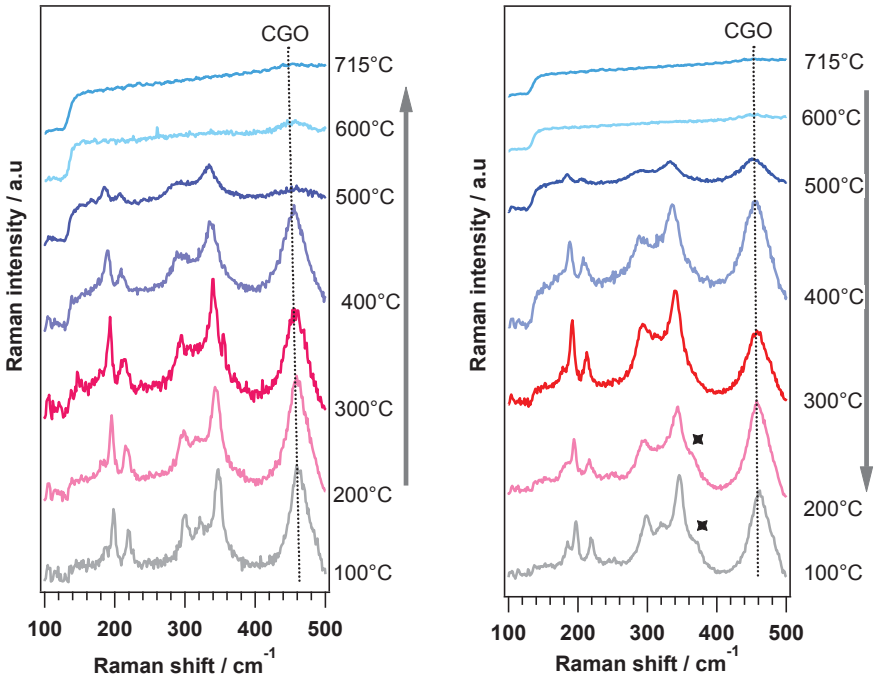

Figure 5. Raman spectra of Ni_3S_2 (formed at the surface of a Ni-CGO pellet) at different temperatures in flowing Ar

However, Ni_3S_2 decomposes partly during a thermal treatment at 850°C. The spectra recorded after cooling to 50°C on different positions show the presence of other nickel sulfides (Figure 6). The new spectra may be those of compounds less rich in sulfur e.g. $Ni_{3+x}S_2$ as suggested by the Ni-S phase diagram [11]. However, an *ex situ* analysis by XRD did not detect the presence of any new phase, probably because its quantity is too low to be detected.

To conclude, NiS is decomposed to Ni_3S_2 at ~400°C whereas Ni_3S_2 is more stable with temperature. It decomposes partly only at 850°C.

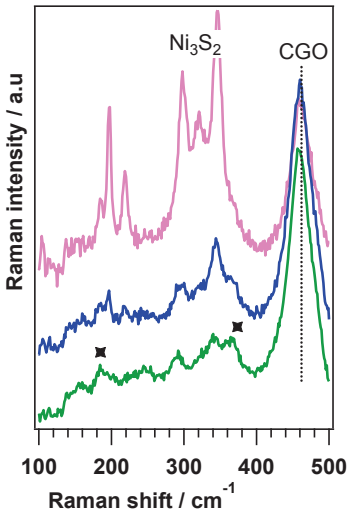

Figure 6. Raman spectra of Ni_3S_2 (formed at the surface of a Ni-CGO pellet) obtained at 50°C after a heat treatment at 850°C

2.4. Other nickel sulfides

Figure 7 displays the Raman spectra of other nickel sulfides taken from the literature: Ni_9S_8 [9], Ni_3S_4 [3], NiS_2 [5]. For Ni_7S_6, vibrational modes could not be seen by Raman spectroscopy [5].

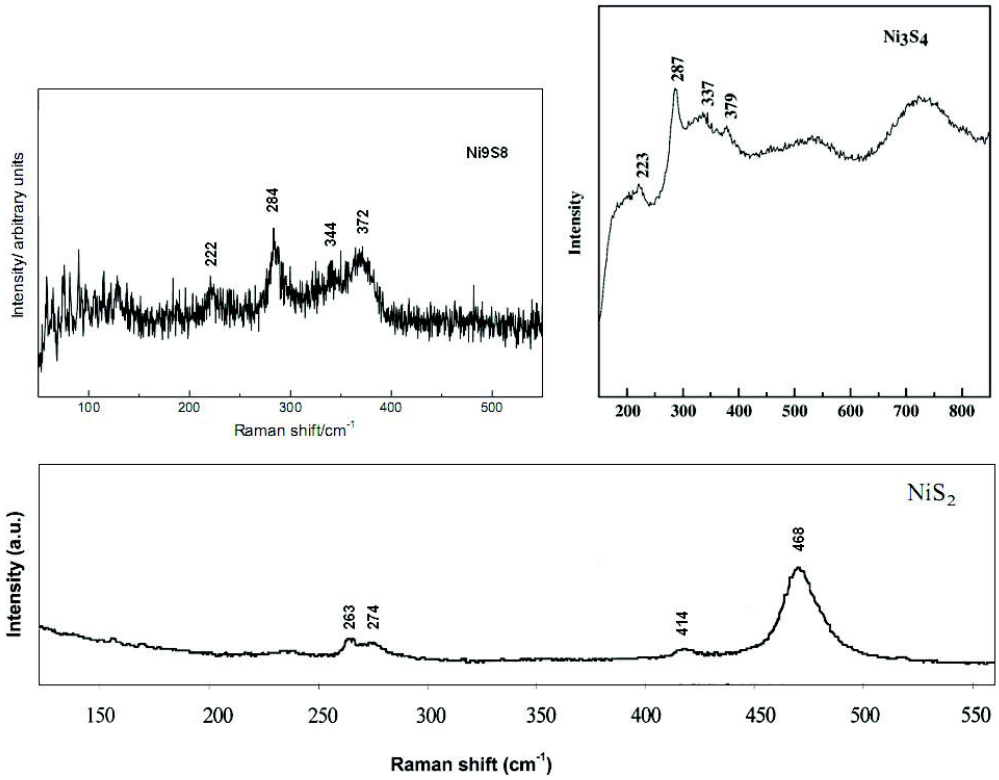

Figure 7. Room temperature Raman spectra of Ni_9S_8 [9], Ni_3S_4 [3], NiS_2 [5]

3. Impacts of H_2S on Ni pellet

The heating of a SOFC system to its high working temperature is done slowly with 2°C/min or 5°C/min to avoid any thermal shock. If there is any trace of pollutant in the gas, it may attack the SOFC anode during heating. The problem is the same when the SOFC is stopped for any reason. So it is necessary to investigate the effect of pollutants between room temperature and the working one.

Before examining the real system (Ni-CGO), it is important to know how pure nickel reacts with H_2S. Ni pellets were exposed to 300 ppm H_2S in 3%H_2/Ar from 200°C to 800°C. The pellet surface appearance and molecular scale changes were monitored *in situ* by an optical camera and Raman spectroscopy at each temperature as a function of time.

3.1. Identification of the reaction kinetics and products

3.1.1. *In situ* Raman spectroscopy

3.1.1.1. At 200°C

Figure 8 shows the Raman spectral changes of a Ni pellet surface at 200°C with H_2S-exposure time. Up to 0.8 h, no band is observed because pure nickel has no Raman spectrum. At 0.8 h, a large broad band emerges at ~344 cm^{-1}, then gradually develops into 3 separate peaks at 344, 318, 297 cm^{-1}. Concomitantly, two other peaks at 217 and 195 cm^{-1} also appear progressively. These bands are characteristic of Ni_3S_2. Up to 6.6 h, no other change is observed. From 7.3 h, a new band appears at 367 cm^{-1}. This band increases gradually while the Ni_3S_2 bands disappear. From 11.8 h, the spectrum characteristic of NiS, especially the band at 241 cm^{-1}, progressively appear. From 14.2 h, the spectra are characteristic of NiS.

So, it is clear that there is a progressive transformation from Ni_3S_2 to NiS. This would involve unidentified intermediate a Ni_xS_y species that gives the 367 cm^{-1} band.

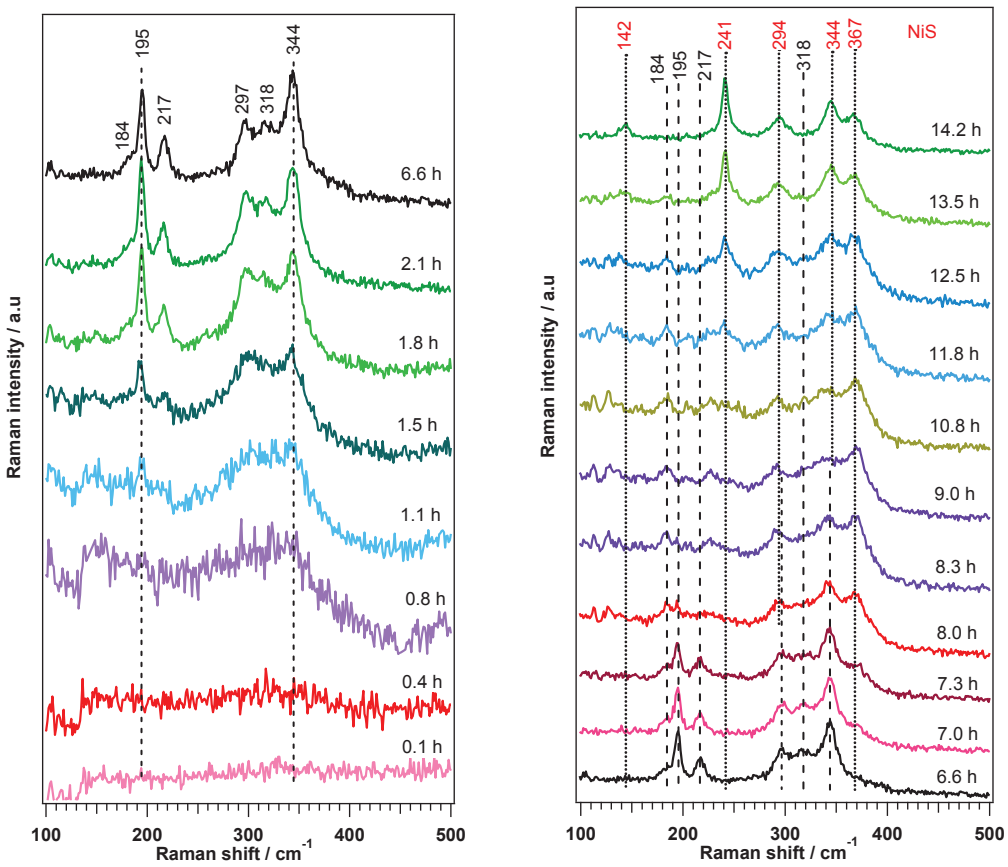

Figure 8. Raman spectra of a Ni pellet recorded at 200°C in flowing 300 ppm H_2S/3% H_2/Ar as a function of time

The relative quantity of Ni_3S_2 can be estimated based on the integrated intensity of the 195 cm^{-1} band since it has a high amplitude, is well-separated from the other peaks, and does not exist in NiS. For the same reasons, the 241 cm^{-1} band of NiS has been used to assess the relative quantity of NiS. The spectra were thus decomposed into individual Lorentzian-shaped peaks to obtain the integrated intensities. A baseline subtraction was performed previously. The fits were limited to the 140-440 cm^{-1} range.

As shown in Figure 9, the quantity of Ni_3S_2 rises sharply within the first two hours, then becomes rather stable in the next 4 hours. The transition of Ni_3S_2 begins as the intensity of the characteristic peak decreases from 6 h. From 8 h to 13 h, the spectra reflect Ni_xS_y intermediate species richer in S. From 13 h, the characteristic peak of NiS at 241 cm^{-1} becoming clear, it allows a precise quantification of NiS. The quantity of NiS increases fast during 3 hours to reach a plateau.

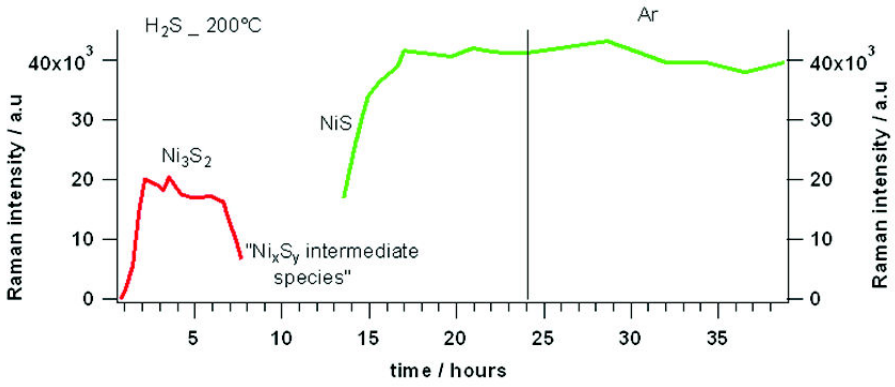

Figure 9. Evolution of the integrated intensities of the bands characteristic of Ni_3S_2 and NiS respectively, as a function of H_2S-exposure time at 200°C

It can be concluded that at 200°C, H_2S reacts very fast with Ni, within 2 hours the surface was saturated with Ni_3S_2. A longer exposure to H_2S enriches Ni_3S_2 to Ni_xS_y then NiS. This transformation happens from 7 h to 13 h, and ends with a saturation of NiS after 17 h.

3.1.1.2. At 300°C and 500°C

Figure 10 shows the evolutions of Raman spectra of Ni surface with time under 300 ppm H_2S at 300°C and 500°C. At 300°C during the first 1.5 hours, no Raman band is observed. At 1.8 h, broad bands emerged at ~320 and 192 cm^{-1}, then developed into characteristic peaks of Ni_3S_2 at longer time. Up to 63 h, there is no more change.

At 500°C, the appearance of Ni_3S_2 peaks can be first seen at 3.2 h. No changes have been observed after 61 h.

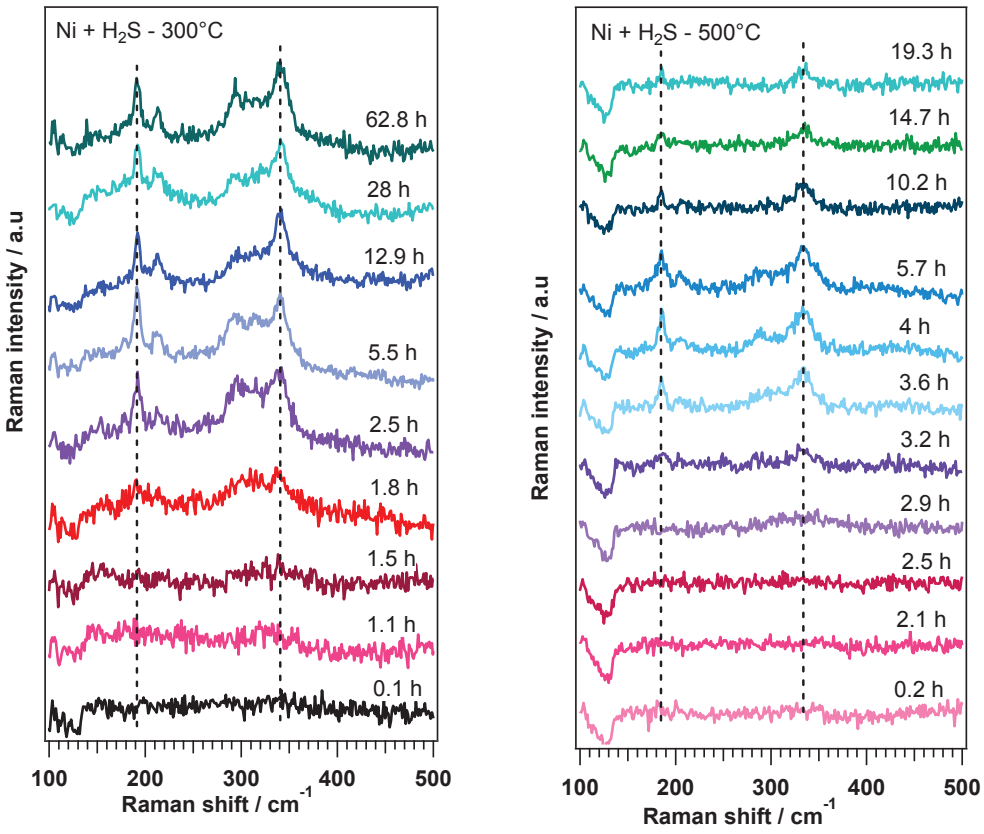

Figure 10. Raman spectra of Ni pellet recorded at 300°C (left) and 500°C (right) in flowing 300 ppm H_2S/3% H_2/Ar as a function of time

The evolution of Ni_3S_2 quantity at 300°C is estimated in the same way as 200°C and is shown in Figure 11. It can be seen that the accumulation of Ni_3S_2 at the surface occurs very fast to reach saturation. It must be noted that, due to the low resolution of the spectra, the quantity of Ni_3S_2 at 500°C could not be estimated.

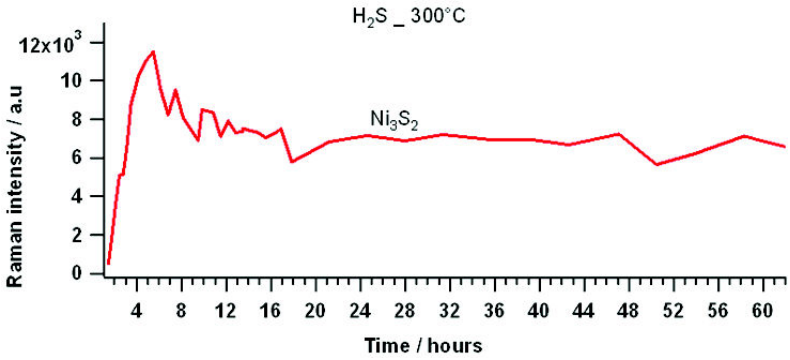

Figure 11. Evolution of the integrated intensities of the 195 cm^{-1} Ni_3S_2 band as a function of H_2S-exposure time at 300°C

3.1.1.3. At 800°C

Since no Raman spectrum of Ni_3S_2 could be recorded above 500°C, a spectrum has been obtained at 50°C after a thermal treatment at 800°C in flowing 300 ppm H_2S/3% H_2/Ar during 18 h. Before cooling fast to 50°C, the system was cleaned by flowing Ar during 1 h in order to avoid residual H_2S. In these conditions, no band have been observed (Figure 12), indicating the absence of nickel sulfide at the pellet surface.

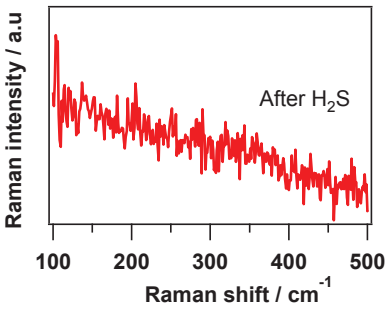

Figure 12. Raman spectrum recorded at 50°C of the Ni pellet surface after H_2S exposure at 800°C

3.1.2. Phase identifications by X-ray diffraction

The chemical nature of the products formed at the Ni surface has been confirmed by XRD (Figure 13).

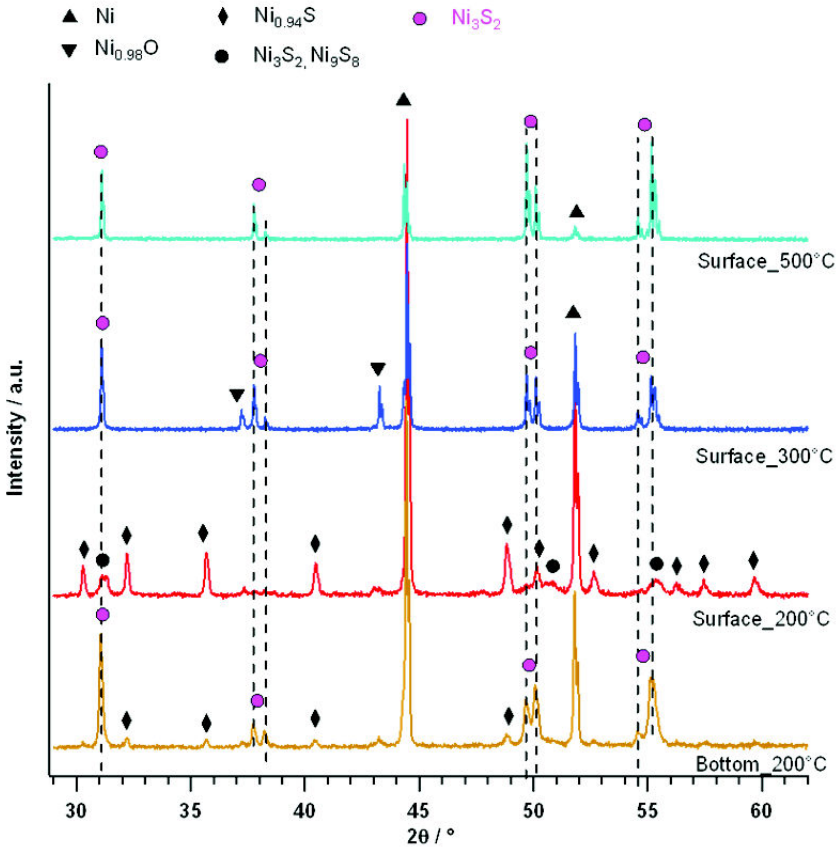

Figure 13. XRD spectra of Ni pellets after exposure to 300 ppm H_2S at various temperatures

An exposure to H_2S at 200°C leads to many kinds of nickel sulfides on the surface, with mostly $Ni_{0.94}S$, a very small amount of Ni_9S_8, and a trace of Ni_3S_2. On the back side, Ni_3S_2 predominates. When compared to the bottom surface, the top surface has a lower temperature and much more contact with H_2S, which facilitate sulfides with a high content of sulfur.

After exposure to H_2S at 300°C and 500°C, Ni_3S_2 also appears, while at 800°C, only Ni is detected on the two faces. It should be noted that intensity ratio of Ni to Ni_3S_2 at the pellet surface decreases with increasing temperature, which indicates that a larger percentage of Ni reacts with H_2S at 500°C than 300°C, and 200°C.

The presence of some peaks characteristic of NiO at 300°C is surprising, since the gas composition during the experiments is highly reducing. An oxygen contamination could have occurred between the end of the sulfidation process and the XRD analysis.

3.1.3. Conclusion on the reactivity of H_2S on Ni with temperature

At 200°C, Ni_3S_2 is formed first, then gradually transforms to a sulfur-richer phase. At 300 and 500°C, only Ni_3S_2 is formed during the examined time. At 800°C, no nickel sulfide is found by Raman spectroscopy.

Table 1 summarizes some kinetic information probed by Raman spectroscopy, i.e. waiting time to see the birth and the saturation of nickel sulfide crystals on Ni pellet surface. From 200°C to 500°C, the formation of Ni_3S_2 can be detected within 1-3 hours, while no crystal can be found after 18 h at 800°C. The saturation of the surface with Ni_3S_2 is obtained in less than 5 hours. This time scale lies inside the time needed to heat a SOFC to its working temperature of ~700°C. Therefore, poisoning may take place during the warming up stage, resulting to a fast degradation at the very beginning of SOFC operation.

Table 1. Velocity of the sulfidation of Ni surface by 300 ppm H_2S/3%H_2/Ar.

Temperature	Appearance/saturation time	Chemical formula by XRD
200°C	1.1 h / 2 h	Ni, $Ni_{0.94}S$, Ni_9S_8, Ni_3S_2
300°C	1.8 h / 4 h	Ni, Ni_3S_2
500°C	3.2 h /	Ni, Ni_3S_2
800°C	No nickel sulfide after 18 h	-

3.2. Surface morphology changes

3.2.1. *In situ* optical imagery monitor

Figure 14 presents the optical images of Ni pellet surfaces as a function of time and temperature in 300 ppm $H_2S/3\%H_2/Ar$.

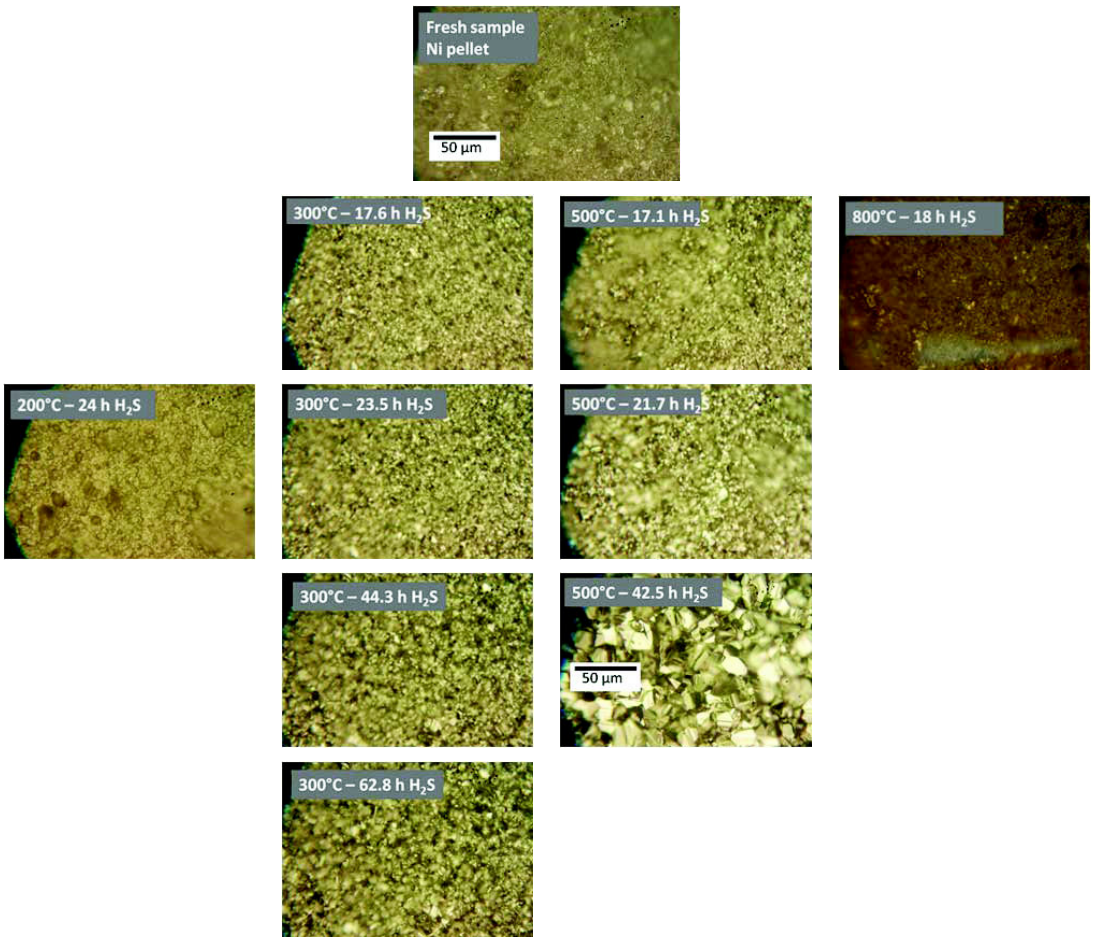

Figure 14. *In situ* images of the Ni pellet facial changes in flowing 300 ppm $H_2S/3\%H_2/Ar$ at various temperatures and times

After ~18 h in H_2S, bright crystals of nickel sulfide can be observed at 300°C and 500°C with the same size scale and larger than those at 200°C (after 24 h), while no change is seen at 800°C.

A longer contact with H_2S at 300°C up to about 63 h does not lead to a crystal growth, while at 500°C, the crystals grow much faster and very big facetted crystals are detected at 43 h. The continuous enlargement of nickel sulfide crystals at 500°C may imply a strong diffusion of bulk Ni to the surface to react with H_2S. It is important to emphasize that this is a sulfur-induced diffusion since there are no observable growths of Ni particles at 800°C.

In summary, the extent of morphological change increases with increasing temperature from 200°C to 500°C, but is minimum at 800°C.

3.2.2. Ex situ investigations by Scanning Electron Microscopy

Figure 15 shows the morphologies of the Ni surface exposed to 300 ppm $H_2S/3\%H_2/Ar$ at different temperatures. Before contact with H_2S, Ni particles are round and smooth with diameters of 1-2 µm. There exist also larger agglomerates due to coalescence effect.

After being exposed to H_2S at 200°C, the round grain changed into pillar form. The contact at 300°C does not lead to a large change in the particle size, but many threads and sticks of some nanometers appear at the surface. EDX elemental analyses indicate the presence of nickel, sulfur and traces of oxygen and carbon.

A surprising change happens at 500°C. No void can be seen at the surface. The initial small and smooth particles develop into big square particles of about 10 µm, on which appear round particles of about 30 nm. Such big crystals were also seen with optical imagery, and are made of nickel and sulfur from EDX analyses.

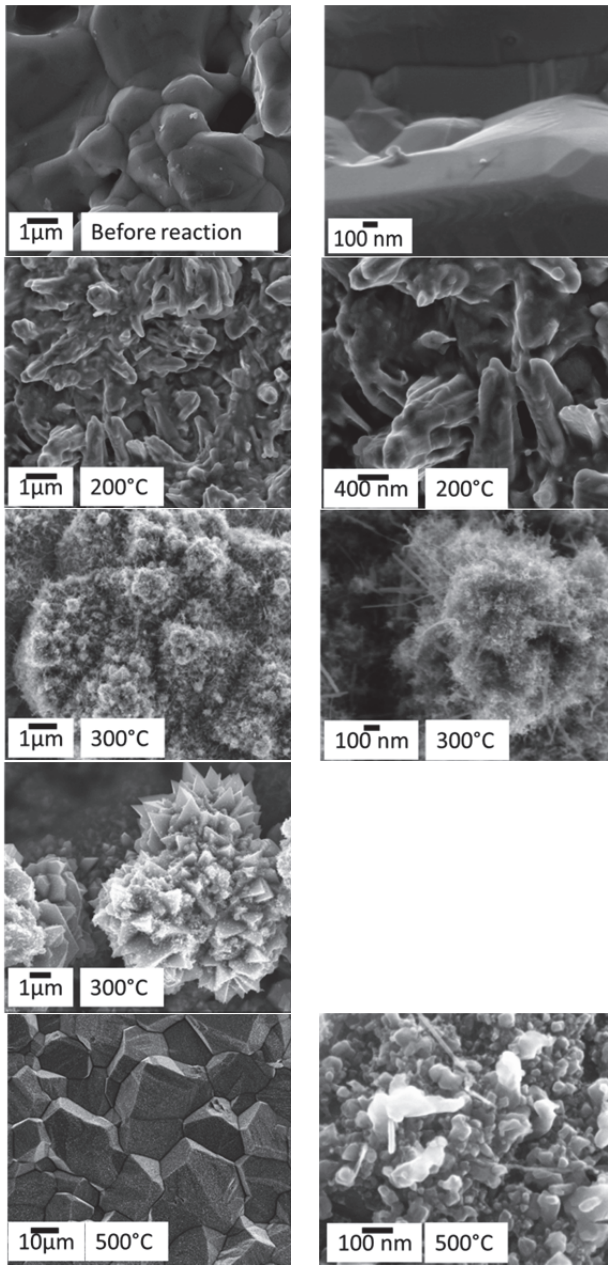

Figure 15. SEM images of the Ni pellet surface before (on top) and after exposure to 300 ppm $H_2S/3\%H_2/Ar$ at different temperatures

3.2.3. Conclusion

The morphology investigations regardless of *in situ* or *ex situ* nature show that the extent of sulfidation of Ni increases following the order: 800°C, 200°C, 300°C, 500°C. No sulfide and morphology change has been observed at 800°C, while the most severe sulfidation happens at 500°C. Ni diffusion was deduced from *ex situ* observation by Lussier et al. [12]. In this study, we showed an *in situ* proof for Ni diffusion. The appearance of a maximum sulfidation as a function

of temperature can be understood as resulting from the competition between a sulfur adsorption which is more favorable at low temperatures [13,14] and a sulfur-induced diffusion of Ni which is faster with increasing temperature. At 800°C, the adsorption is very limited, resulting in an weak sulfur-induced Ni diffusion. So, no nickel sulfide or no morphology change can be observed by *in situ* Raman spectroscopy and optical imagery. At 500°C, the adsorption is considerable and the sulfur-induced diffusion of Ni is fast, which lead to the formations of very big faceted crystals. At 200 and 300°C, although the adsorption is most favorable, the velocity of Ni diffusion is limited due to low temperature. Thus, the morphology is less affected by H_2S than at 500°C.

The surface morphology is transformed in diverse ways depending strongly on the temperature. Therefore, it is necessary to conduct the evaluation of H_2S impact at each temperature, since the extrapolation may not work well.

3.3. Impacts of H_2S on Ni pellet during the heating process

The warming up stage of SOFC system to high working temperature is done slowly with 2°C/min or 5°C/min in gaseous atmosphere. So, it is important to study the effect of H_2S during this sensitive step. For this purpose, a Ni pellet was heated up to 800°C in a flowing polluted gas of 300 ppm $H_2S/3\%H_2/Ar$ at 2°C/min. Figure 16 shows the *in situ* Raman spectra and optical images obtained at different temperatures during the heating step.

Raman spectra reveal that Ni_3S_2 is formed as early as at 200°C, and still exist up to 500°C. However, the formation of Ni_3S_2 crystals at these temperatures does not cause a visible morphology change in optical images. Above 600°C, the bands of Ni_3S_2 disappear. A morphology change starts at 700°C and is remarkable at 800°C with the formation of big agglomerates.

After 10 minutes at 800°C in H_2S, the gas was then changed to Ar. A long time of purging of 5 hours was used to ensure a complete removal of H_2S before cooling down. No futher change in the surface appearance could be noted during the decrease of temperature. Raman spectra recorded at ambiant atmosphere from different positions all reveal the presence of Ni_3S_2.

In conclusion, the big agglomerates seen at 800°C are nickel sulfides created early at lower temperatures. This implies the fact that the presence of H_2S during the heating may lead to a severe sulfidation and morphology change at high working temperature.

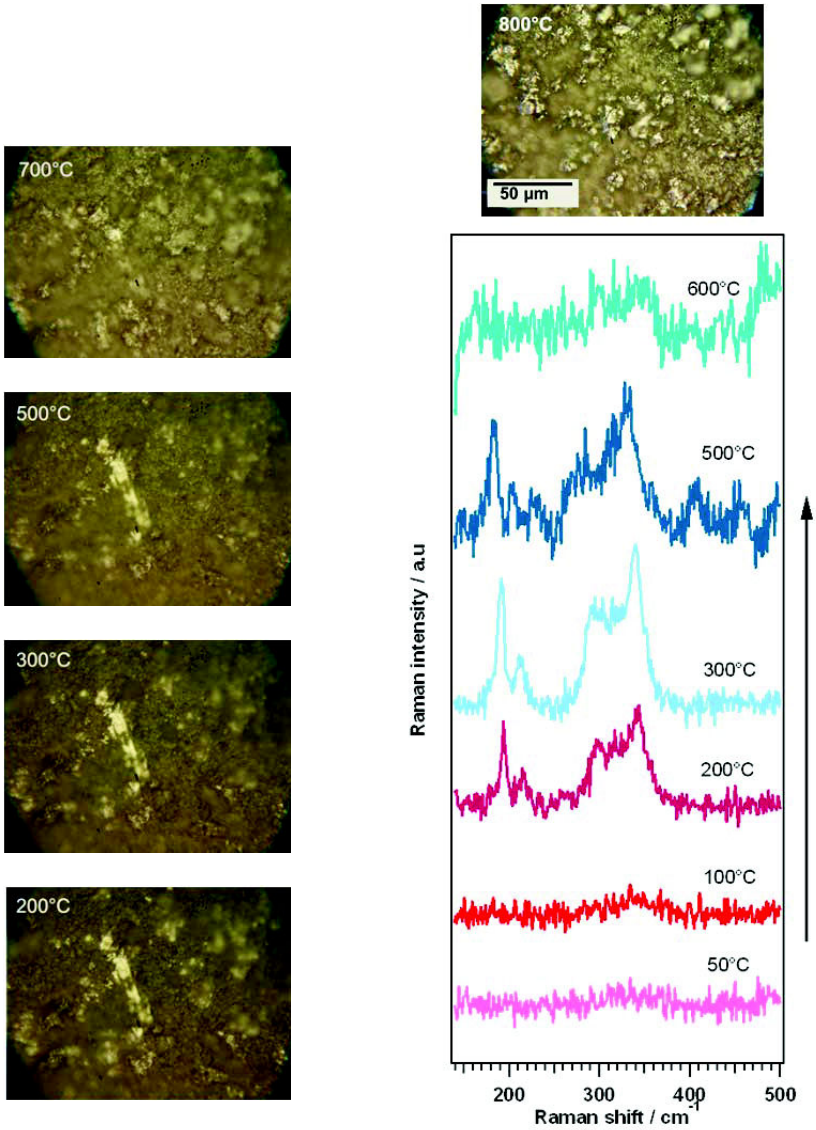

Figure 16. ***In situ*** **Optical images and Raman spectra of a Ni pellet surface at different temperatures during the heating in flowing 300 ppm H_2S/3%H_2/Ar**

4. Impacts of H_2S on Ni-CGO anode material

The SOFC performances depend strongly on the anode microstructure, in which an homogeneous distribution among nickel, ceramic phase (gadolinium-doped cerium oxide CGO or yttrium-doped zirconium oxide YSZ), and gas (porous) phases will insure long triple-phase boundaries for the oxidation of hydrogen. The experiments on Ni pellets have demonstrated that the sintering of Ni is accelerated in the presence of H_2S. Since the presence of a ceramic phase is expected to prevent the coalescence of nickel particles, this part will try to elucidate the poisoning extent of H_2S to Ni in the presence of a ceramic network. Due to the technical threshold of the halogen heating lamps, the temperature was limited to 715°C for long term experiments.

4.1. At 715°C and above

4.1.1. Formation of nickel sulfide crystals at 715°C

Since Raman spectra of nickel sulfide cannot be recorded above 500°C, *in situ* optical imagery was employed to monitor the interactions between H_2S and Ni-CGO at 715°C. Ni-CGO pellet was thus subjected to flowing 500 ppm H_2S/3%H_2/Ar during 14 h at 715°C.

Figure 17 shows the morphological changes of Ni-CGO as a function of time. At 5.2 h, bright dots appear at the surface and then gradually grow up into many different shapes with increasing time.

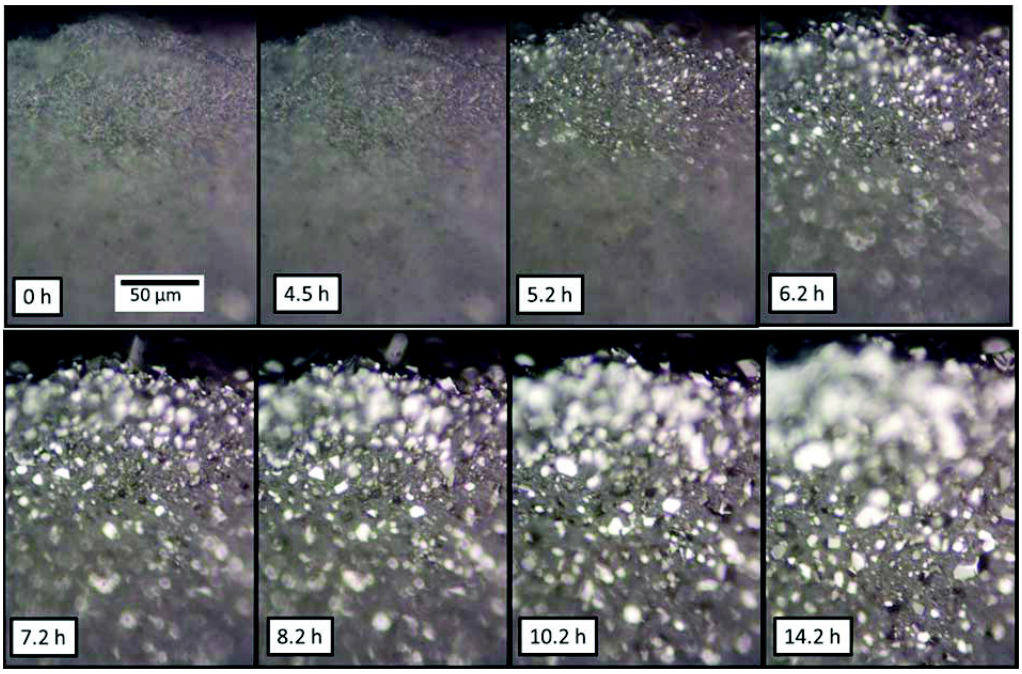

Figure 17. *In situ* optical images of the Ni-CGO surface at 715°C at different exposure times to 500 ppm H_2S in 3%H_2/Ar

When the pellet was cooled to 50°C in Ar, the surface appearance remained unchanged. Raman spectra at 50°C taken from the background of the surface and the bottom (laser in line mode) are presented in Figure 18. The bands characteristic of CGO can be seen at 461 cm^{-1} (main band) and at about 580 cm^{-1} (a double shoulder) [15]. The peaks of Ni_3S_2 are also clear.

Figure 19 displays the spectra of the big bright crystals. All the vibrational frequencies correspond well with Ni_3S_2.

It is evident that the crystals of nickel sulfide are really formed at the temperature of 715°C though no Raman spectrum could be obtained. The well-defined shapes are attained owing to slow crystal nucleation and growths when H_2S gas passes over the pellet surface.

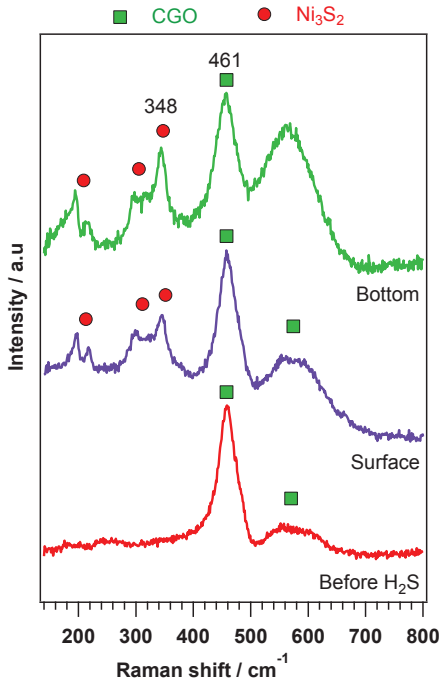

Figure 18. Spectra obtained from the surface and bottom of Ni-CGO pellet after 500 ppm H_2S/715°C/14 h

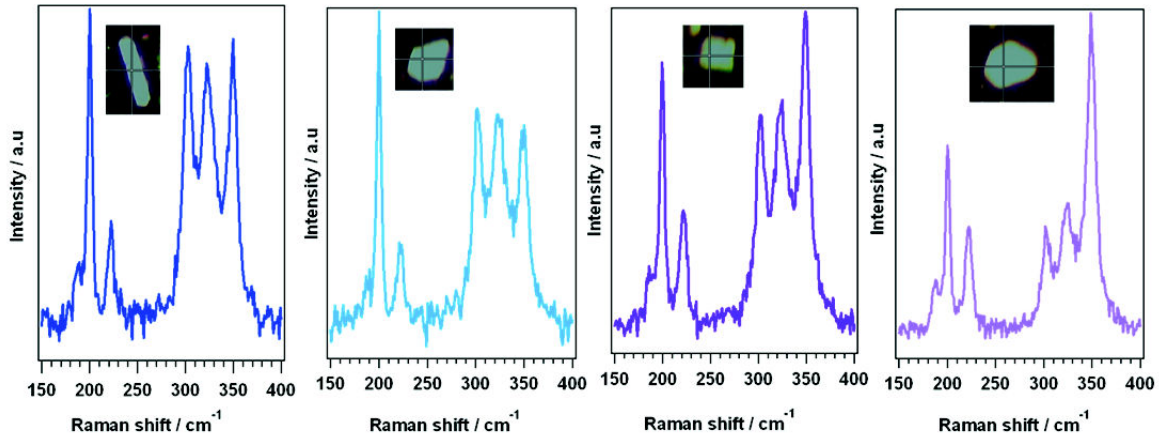

Figure 19. Raman spectra of different crystals on Ni-CGO surface recorded 50°C after 14.2 h of exposure to flowing 500 ppm H_2S in 3%H_2/Ar at 715°C

The velocity and extent of nickel sulfide growths vary according to the position on the pellet surface, in which nickel sulfides are formed and grow faster at the border of the pellet. The first bright crystals can be seen after about 2-3 h at the border, and about 7h at the center of the pellet (see Figure 20). This can be explained by 2 reasons:

i) the temperature at the edge is lower since the heat can dissipate faster to the gas surroundings;

ii) the pellet is less compact at the border than the center, so the crystals have larger spaces to develop.

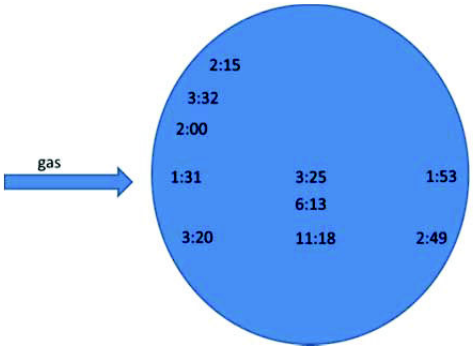

Figure 20. Time (hh:mm) needed to see first bright points on Ni-CGO surface in 500 ppm H_2S at 715°C

4.1.1.1. Spatial distribution of sulfide compounds inside the pellet

In order to know H_2S impact on the whole pellet, the quantification of the various elements was done by EDS-SEM. A much higher ratio of S to Ni (or Ce) is obtained on the pellet surface than on the bottom.

Figure 21 depicts the relative distribution of S as a function of depth from the surface (x= 0) to the bottom (x= L). The minimum quantity is seen at about 500 µm depth.

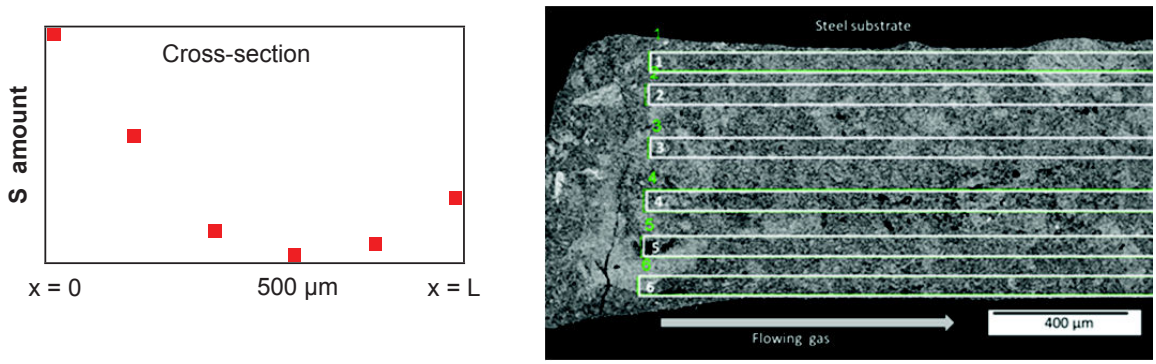

Figure 21. Evolution of S content (in normalized weight percentages) obtained from 6 zones on the cross-section of the pellet exposed to 500 ppm H_2S at 715°C in ~ 14 h

4.1.1.2. Conclusion

When Ni-CGO pellet was exposed to 500 ppm H_2S at 715°C during 14 h, two compounds CGO and Ni_3S_2 can be seen by Raman spectroscopy. The various forms of crystals may indicate preferred selective adsorptions of sulfur on different Ni planes.

A higher ratio of S to Ni (or Ce) is obtained on the pellet surface than on the bottom. The distribution of S quantity as a function of depth follows a parabolic shape, with minimum value at ~500 µm below the surface. This implies a limited effective diffusion length of H_2S. From a technical point of view, an anode-supported SOFC with a thickness more than 500 µm may be a good choice to protect the interface anode/electrolyte, since H_2S will attack the uppermost layers.

4.1.2. Disappearances of nickel sulfide crystals at higher than 715°C

Once nickel sulfide crystals have been formed in flowing 500 ppm H_2S at 715°C after 17.7 h, the temperature was raised fast to 750°C. As shown in Figure 22, the crystals in the pellet center disappear immediately.

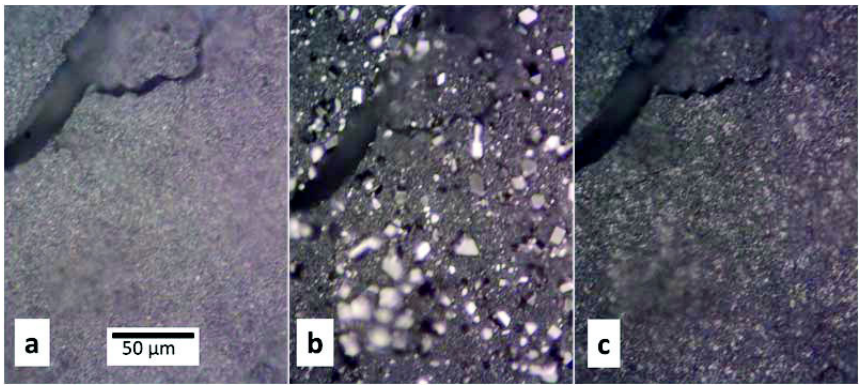

Figure 22. *In situ* optical images of Ni-CGO surface appearance in 500 ppm H_2S a) before H_2S contact; b) after 17.7 h at 715°C; c) when the temperature reached 750°C

At the pellet border, the crystals can still be observed after 3 hours at 750°C in flowing 500 ppm H_2S. Increasing the temperature up to 770°C for 40 min, 780 °C for 15 min and 790°C for 15 min, successively, leads to the progressive disappearance of the bright crystals as a function of time (see Figure 23 and Figure 24) in favor of black round spots. This shape could indicate the fusion of the crystals. The surface appearance without bright crystals remains unchanged during the cooling down to room temperature in Ar.

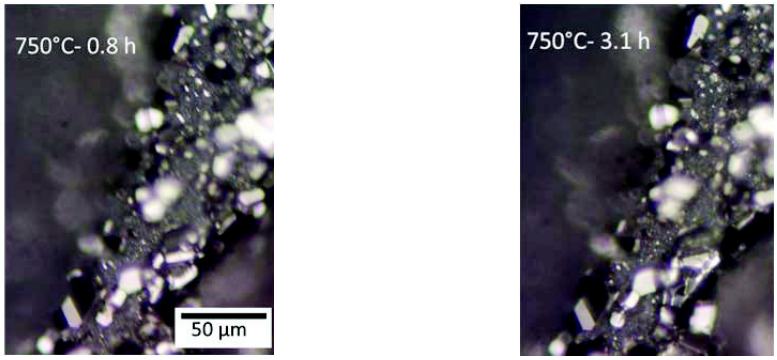

Figure 23. *In situ* images of nickel sulfide crystals at 750°C in 500 ppm H_2S as a function of time

Figure 24. *In situ* images of nickel sulfide crystals at 770°C in 500 ppm H_2S as a function of time. Yellow circles indicate the appearance of black round shapes

Figure 25 exhibits various spectra obtained at room temperature from the pellet surface and bottom at different positions before and after H_2S exposure. Besides CGO, Ni_3S_2 can be well identified. The two broad bands at 575 and 179 cm^{-1} and two small bands at 411, 262 cm^{-1} could be assigned to a cerium oxysulfide ($Ce_2O_{2.5}S$) [16]. The presence of $Ce_2O_{2.5}S$ has been then confirmed by XRD.

When compared to the main CGO band intensity (461 cm^{-1}), the intensities of $Ce_2O_{2.5}S$ bands are much lower at the surface than at the bottom. Thus cerium oxysulfide is created less at the surface than at the bottom.

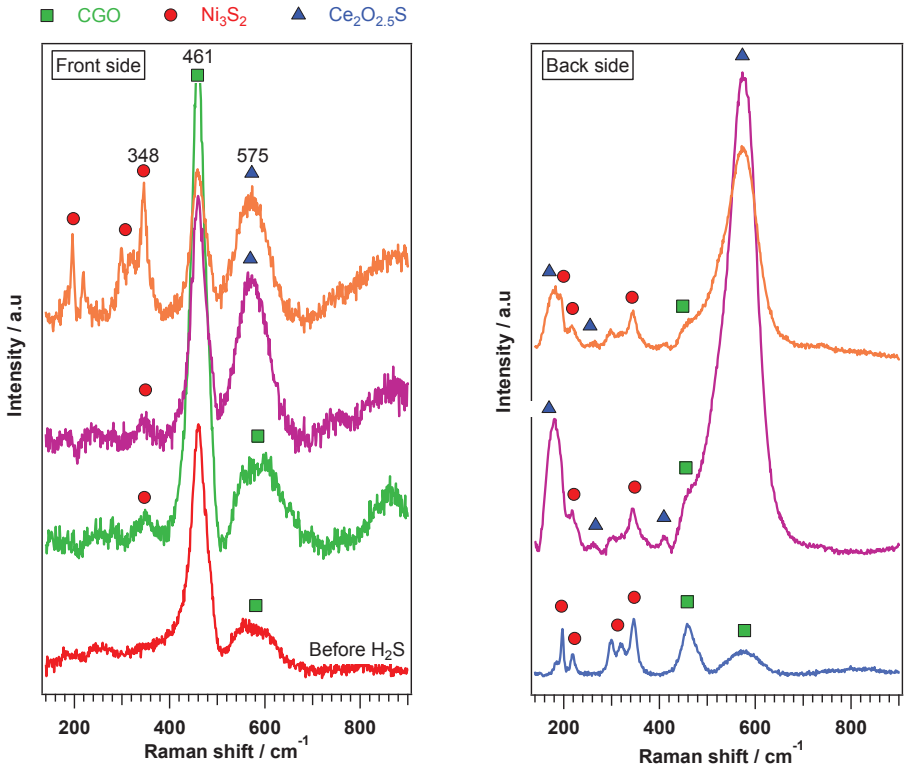

Figure 25. Raman spectra recorded at room temperature from the surface (left) and the bottom (right) of the Ni-CGO pellet being exposed to 500 ppm H_2S at 750-790°C

4.1.2.1. Spatial distribution of sulfide compounds inside the pellet

An elemental analysis (EDS) has revealed a much higher sulfur concentration at the bottom than at the surface. The situation is in contrast with the case at 715°C only (see part 4.1.1.1). This could be explained by the fact that due to the higher temperature of the bottom surface, CGO at the bottom reacts faster with H_2S. Alternately, the lower concentration of S at the surface could be related to the disappearance of nickel sulfide crystals above 715°C. This vanishing could be due to the fusion of nickel sulfides, since the phase diagram Ni-S indicates the presence of at least two liquidus curves in the range 637-1000°C [11]. So, when the crystals melt, they penetrate into the porous substrate, leading to a decrease of S detected at the surface by EDS-SEM. A decomposition of nickel sulfide as suggested in part 2.3.2 is likely to be another explanation.

Raman mapping was used to determine the distribution of Ni_3S_2 and $Ce_2O_{2.5}S$ inside the pellet. The mapping was performed along 7 lines at 11 points/line in the cross-section. The laser beam was used in line mode (line length ~45 µm) to obtain at each point an average concentration. The quantities of CGO, $Ce_2O_{2.5}S$ and Ni_3S_2 have been evaluated by the heights of

461 cm^{-1}, 575 cm^{-1} and 348 cm^{-1} bands respectively. Figure 26 reveals the distribution of each compound as a function of depth from the surface.

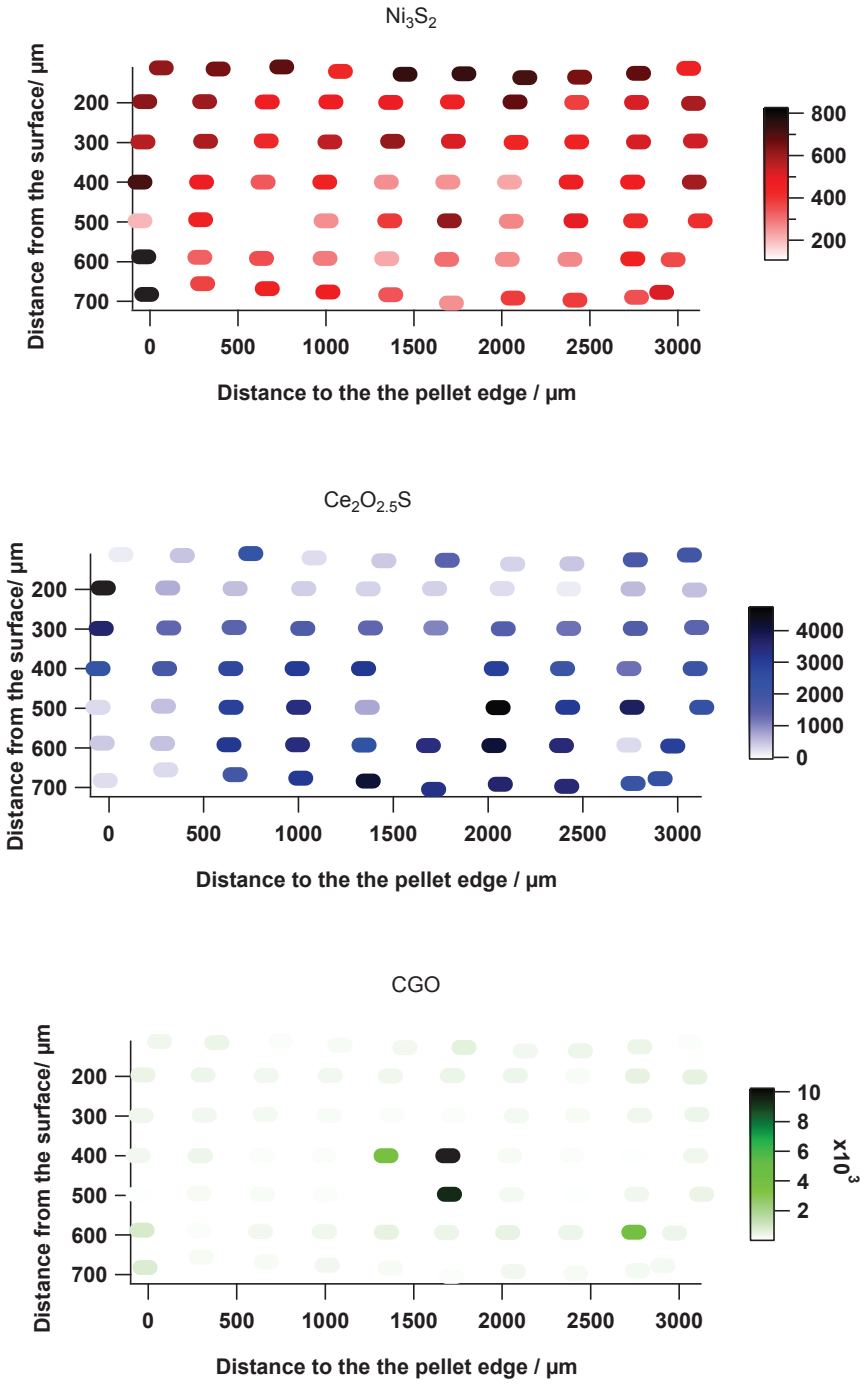

Figure 26. Distribution of each compound (Raman peak height) as a function of depth from the surface. Each point represents an area of 45 x 4 µm

It is clear that cerium oxide sulfide is more present near the bottom than near the surface while nickel sulfide can be found more near the surface.

4.1.2.2. Conclusion

When a Ni-CGO pellet was exposed to 500 ppm H_2S at 715°C, two compounds CGO and Ni_3S_2 have been detected by Raman spectroscopy. In the experiment when the temperature was raised to 790°C, much $Ce_2O_{2.5}S$ was found besides Ni_3S_2. This result has been confirmed by XRD. Higher quantity of Ni_3S_2 and lower quantity of $Ce_2O_{2.5}S$ on/near the surface than on/near the bottom have been obtained consistently from different experiments. These two observations help to conclude that high temperature facilitates the reaction between H_2S and CGO while impedes the reaction between H_2S and Ni.

4.1.3. Morphological changes under H_2S at above 715°C

The morphology of the surface after an exposure to H_2S of about 14 h at 715°C was determined by SEM (Figure 27). The big bright crystals of Ni_3S_2 mentioned above are facetted, with diameters varying between 2 and 10 µm, lying high above the surface. It is interesting to note that in the fresh sample, Ni particles have diameters of 0.5-1 µm and are surrounded by CGO particles (see Chapter 2). So, there must have had a strong diffusion of Ni toward the surface to gather and to form such big facetted crystals of Ni_3S_2.

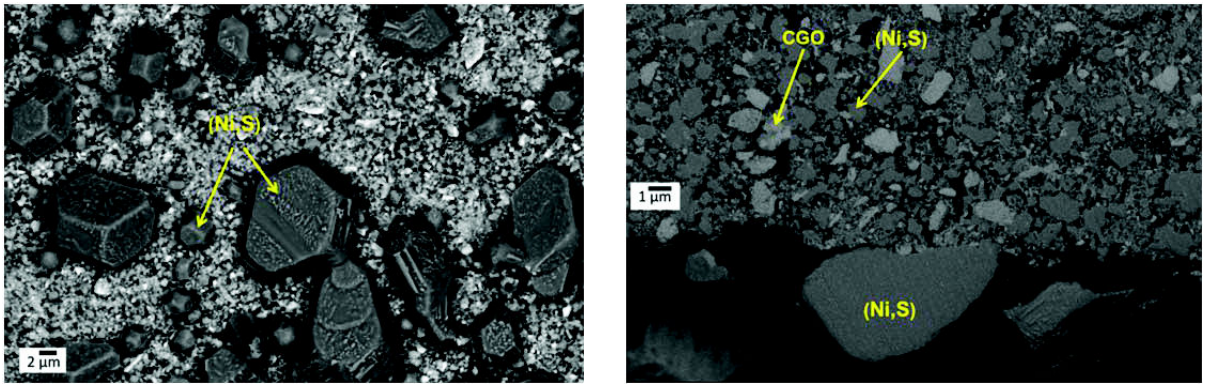

Figure 27. ESB images of the surface (left) and the cross-section (right) and of the pellet exposed to 500 ppm H_2S at 715°C during about 14 h

On the back side (Figure 28), the white small particles are CGO, and the larger, darker particles comprise Ni and S. There is not much difference with the morphology of the fresh sample. Great change comes only at the surface with the formation of various shapes of nickel sulfide crystals. An open contact to H_2S together with a lower temperature at the surface could facilitate the appearance of such big crystals.

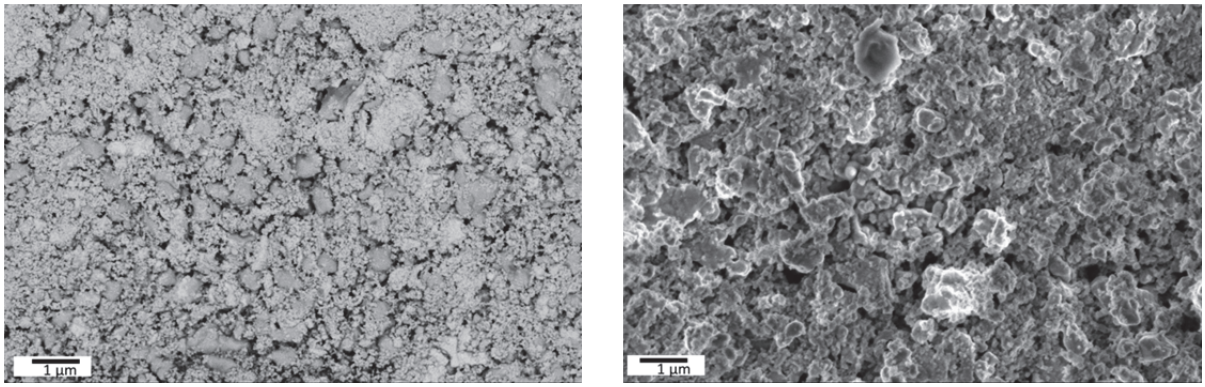

Figure 28. Back-scattered electrons (left) and secondary electrons (right) images of the back side of the pellet exposed to 500 ppm H_2S at 715°C in about 14 h

After the 750-790°C treatment, the morphology of the pellet surface is shown in Figure 29. There is not much contrast between Ni- and ceramic-based phases (compared to the images obtained after the treatment at 715°C). The differentiation is mostly based on the size of particle, with much smaller size corresponding to ceramic phase. This may be due to the change of CGO to cerium oxysulfide.

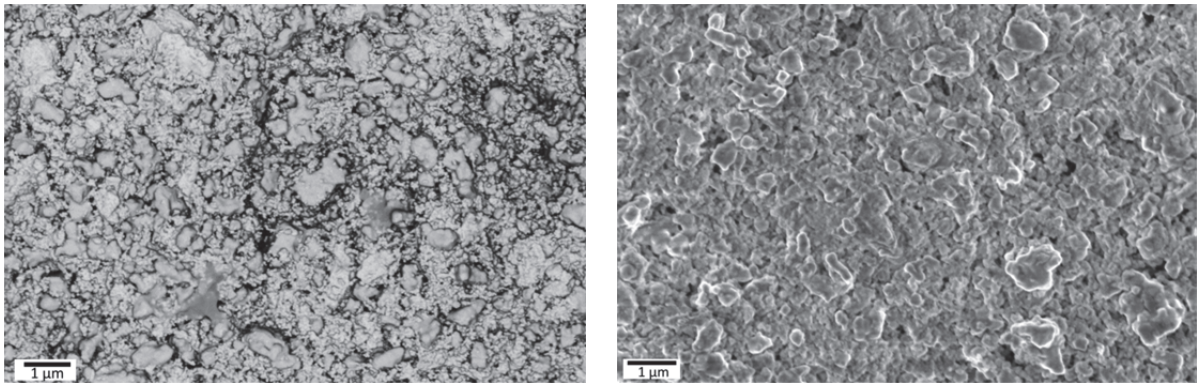

Figure 29. Back-scattered electrons (left) and secondary electrons (right) images of the surface of the pellet exposed to 500 ppm H_2S at 750 – 790 °C

4.2. At 500°C

In situ Raman spectra and optical images of the Ni-CGO pellet exposed to 500 ppm H_2S in 3%H_2/Ar at 500°C during 12.3 h are given in Figure 30.

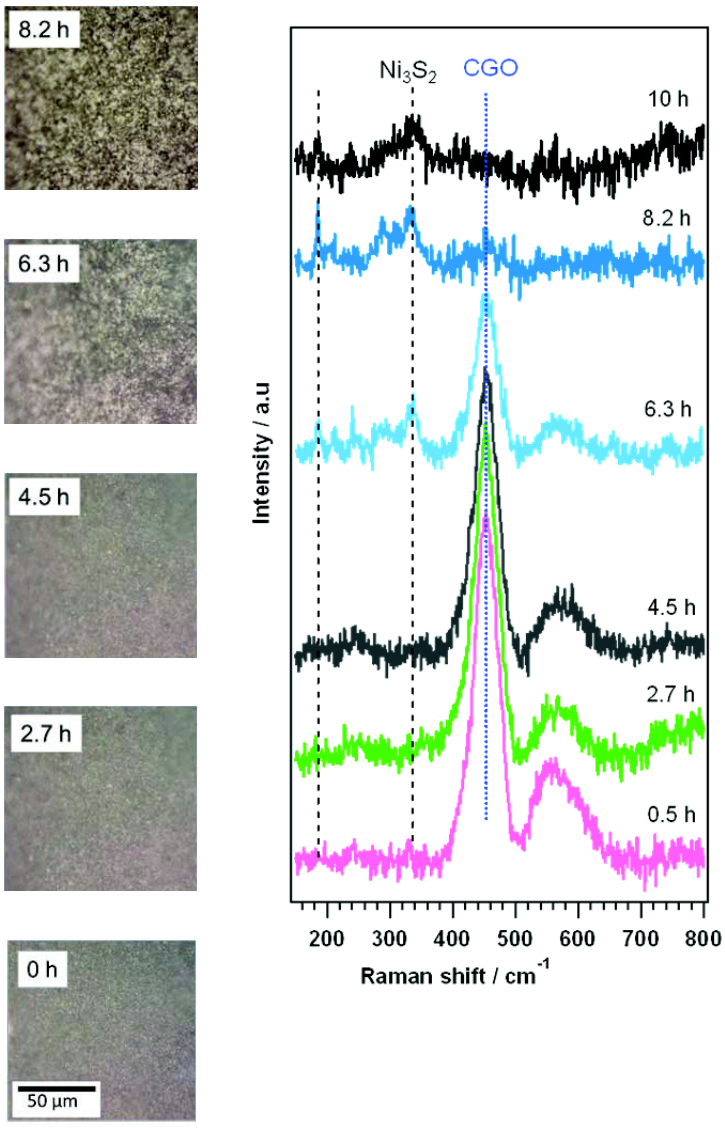

Figure 30. Evolution of the surface appearance and Raman spectra of Ni-CGO pellet at 500°C in 500 ppm H_2S

From 0.5 to 4.5 h, no morphology change has been observed and the Raman spectra are characteristic of CGO. At 6.3 h, new bands characteristic of Ni_3S_2 appear, together with bright dots. At 8.2 h, the Ni_3S_2 peaks intensities overweight those of CGO, while the surface transforms to a new bright texture. At 10 h, only Ni_3S_2 peaks are observed. So, it is clear that the bright dots come from Ni_3S_2 crystals which grow up as a function of time. *Ex situ* Raman spectra recorded in room condition show the presence of only Ni_3S_2 in the surface, and the presence of CGO and Ni_3S_2 at the bottom of the pellet.

SEM analyses have been conducted on the surface, the back side as well as the cross-section of the pellet (Figure 31). In the fresh sample, Ni particles have average diameters of 0.5-1 µm, and are surrounded by CGO particles. After being exposed to H_2S at 500°C, the surface

changed completely, from a porous structure to a dense continuous one with only nickel and sulfur elements.

An examination of the cross-section reveals that the entire surface is covered with a (Ni, S) layer of 1-2 µm thick. The morphology below the (Ni, S) layer retains a porous cermet structure similar to the reference. It can be supposed a strong diffusion of nickel from the interior to the pellet surface. The diffusion would be stimulated by a high affinity of nickel to sulfur, leading to a total destruction of the anode surface structure. The morphology of the back side seems to still reflect a homogenous distribution between nickel and CGO phase.

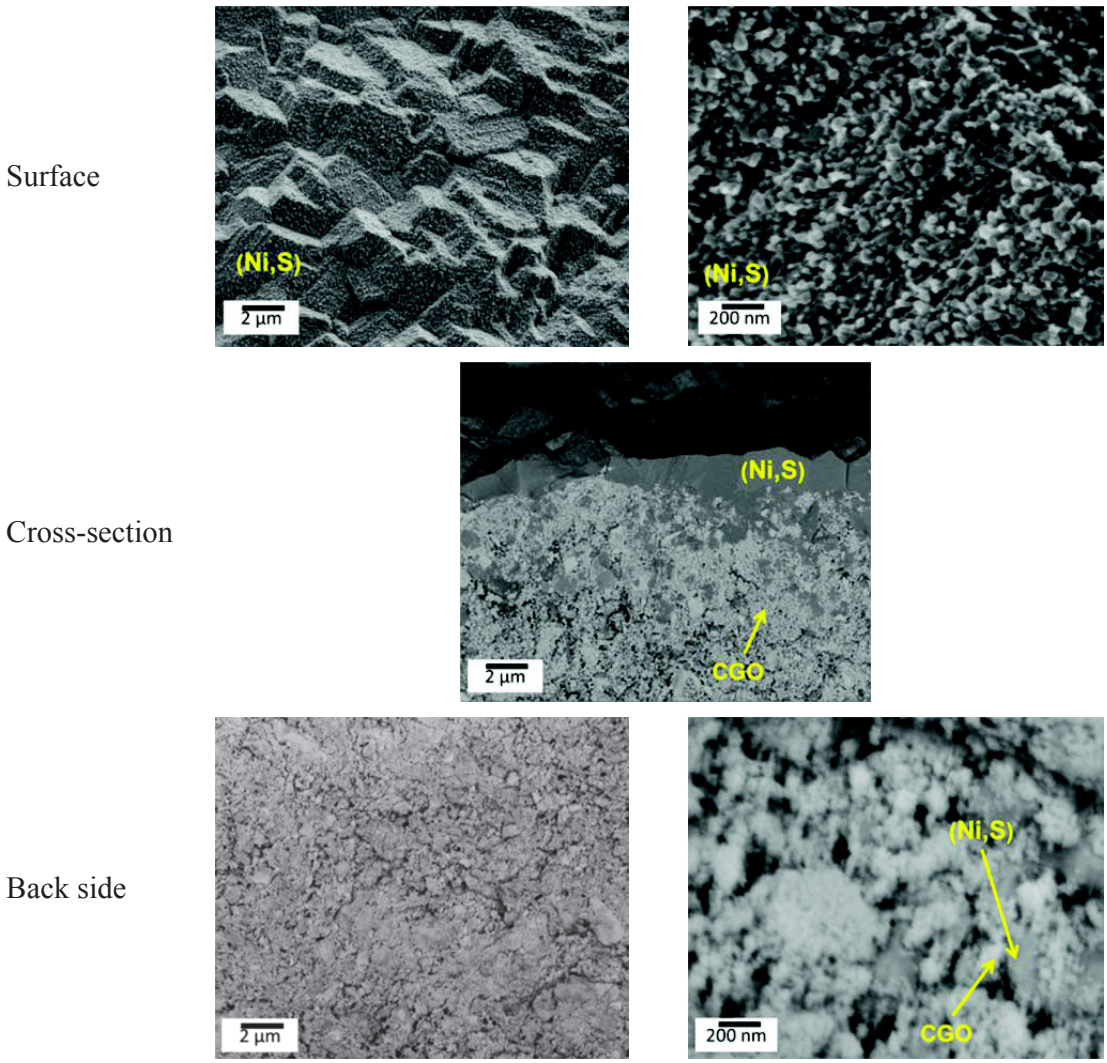

Figure 31. SEM images of the surface, the cross-section and the back side of the pellet exposed to 500 ppm H_2S at 500°C

In order to better understand the diffusion phenomenon, elemental quantitative analyses as a function of depth below the surface have been performed by EDS-SEM. The results are presented in Figure 32 in the form of peak height ratio of S to Ce (the Ce peak chosen was that at 4.7 keV since its height was constant). Below 30 µm, little or no S can be observed by EDS-SEM. It can

be explained either by H_2S gas-diffusion blocking effect due to a dense layer of nickel sulfide on the surface, or by limited exposure time.

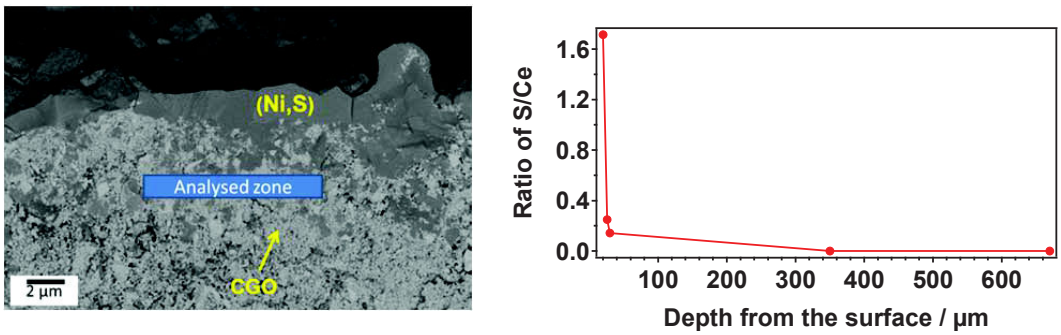

Figure 32. Evolution of the S/Ce ratio as a function of depth in the pellet exposed to 500 ppm H_2S at 500°C. The zone measured is marked in the left image

XRD was used to identify the nature of phases existing on the pellet surface/bottom (Figure 33). On the surface, the Ni_3S_2 peaks dominate, while the CGO peaks become very small and no peaks of Ni can be seen. These results confirm the formation of a Ni_3S_2 layer which contains CGO particles inside. The diffraction pattern of the back side is identical to that of the fresh sample with Ni and CGO peaks.

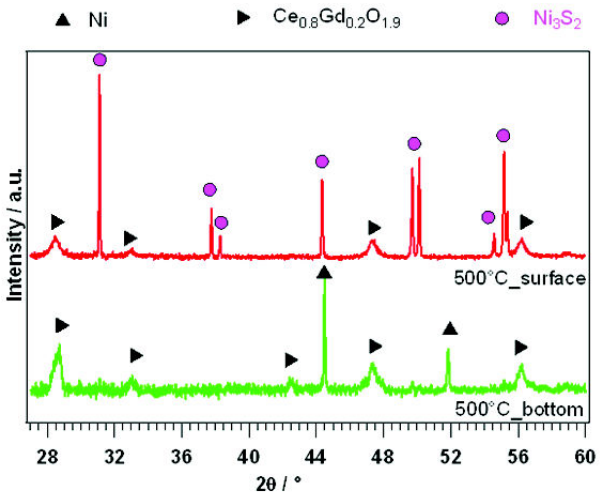

Figure 33. XRD analyses of the surface and the back side of the pellet exposed to 500 ppm H_2S at 500°C

In conclusion, an exposure to H_2S at 500°C leads to the formation of a dense Ni_3S_2 layer covering the porous cermet structure inside. Ni_3S_2 is the only sulfidation product, the quantity of S decreases abruptly to nearly 0 from about 30 µm below the surface.

4.3. At 200°C

At 200°C no morphology change can be seen by optical imagery during 11.5 h in 500 ppm H_2S.

XRD patterns of the pellet after treatment (Figure 34) have shown the presences of NiS and Ni_9S_8 at the surface, and Ni_3S_2 on the back side. No nickel could be detected by XRD on the pellet surface.

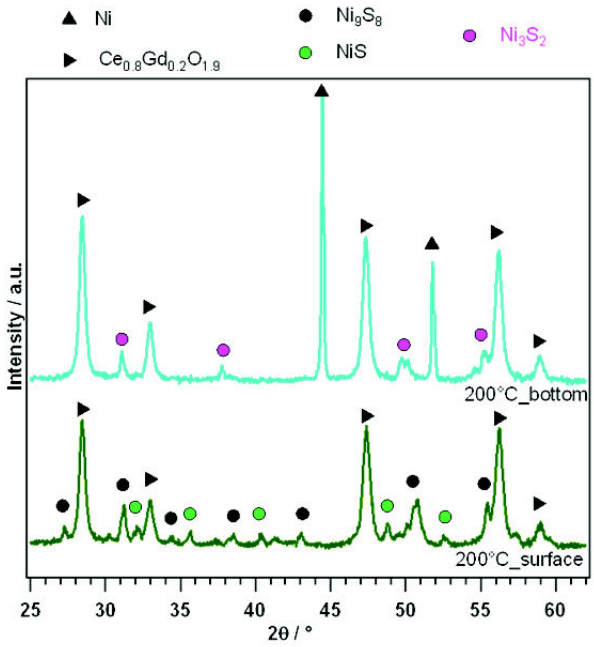

Figure 34. XRD analyst of Ni-CGO pellet exposed to 500 ppm H_2S at 200°C

Ex situ Raman spectra recorded as a function of depth below the surface are shown in Figure 35. As in the case of pure Ni, NiS is formed at the pellet surface. Going further inside the pellet, there appears Ni_3S_2, in addition to NiS. A phase less rich in sulfur like Ni_3S_2 is expected in the interior since the contact with H_2S is more limited with increasing depth. From a certain depth, no nickel sulfide is detected, the spectra being characteristic of CGO. On the back side of the pellet, due to limited contact with H_2S, mainly Ni_3S_2 is observed. EDS chemical analysis by SEM also confirmed a decrease of S as a function of depth below the surface, at the depth of ~350 µm almost no S is detected.

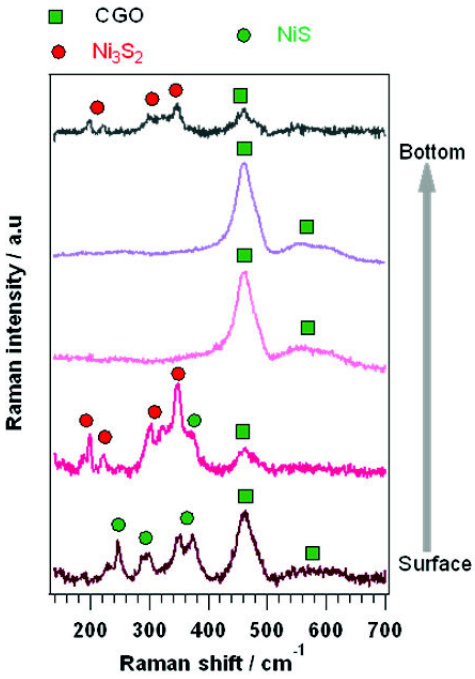

Figure 35. Raman spectra at different depths below the surface

After exposing to H_2S during 11.5 h at 200°C, SEM investigations have not revealed any clear morphological difference with the fresh sample.

One remarkable feature observed from SEM is a fracture near the surface as in Figure 36.

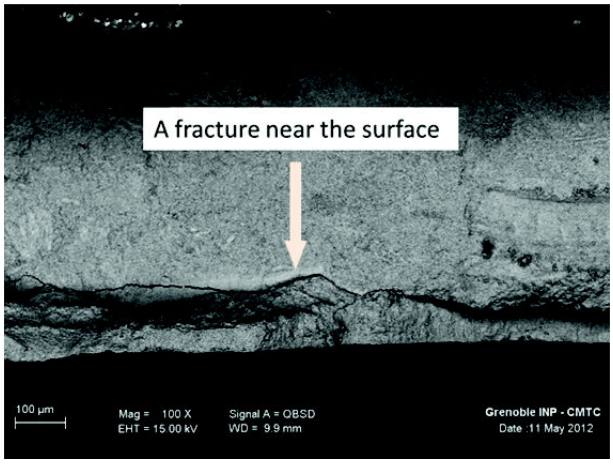

Figure 36. SEM image of the pellet surface showing a fissure near the surface of the pellet after an exposure to 500 ppm H_2S at 200°C

Quantifications along the direction perpendicular to the fissure were conducted at different positions of the cross-section. The results obtained are the same as displayed in Figure 37, S (in normalized mass %) profile is presented in red line. It can be seen that the quantity of sulfur diminishes strongly after the fracture. Therefore, it is more likely that the formation of NiS layer

creates a large volume expansion compared with the rest of Ni_3S_2 or Ni, thus bringing about a fissure.

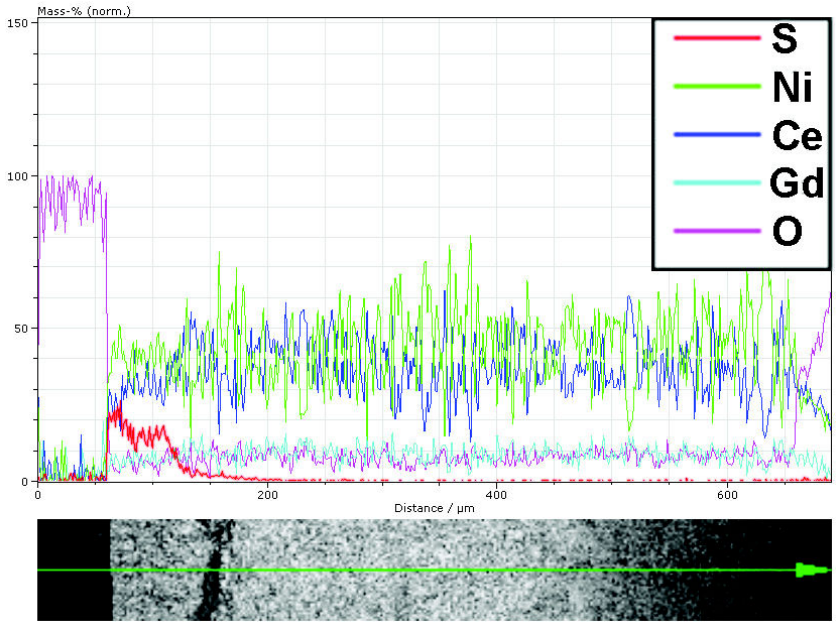

Figure 37. Relative quantifications along the green arrow from the surface to the bottom of the pellet exposed to 500 ppm H_2S at 200°C. Notice the S concentration changes (thick red line) with its disappearance after the crack

To conclude, an exposure to H_2S at 200°C results in the formation of NiS at the surface to a certain depth, of Ni_3S_2 with lower S-content at deeper layers, and no sulfide product at deeper distance from the surface. A fissure formed near the surface may be caused by volume expansion when Ni is transformed into NiS and Ni_3S_2.

5. Removal of nickel sulfides

It is important to study the ability to remove sulfur species out of the surface in order to recover the anode performance. Oxygen has been suggested to transform nickel sulfide into nickel oxide; however the oxidation/reduction cycles of Ni/NiO were reported to be detrimental to the thermomechanical stability of the anode [17,18]. Since the study on the decomposition of nickel sulfides in part 2.3.2 has pointed out that Ni_3S_2 is decomposed partly at 850°C in Ar, we will try first with high temperature and then with hydrogen gas to eliminate sulfur species.

5.1. At 850°C in Ar

A Ni-CGO pellet with bright crystals of Ni_3S_2 at the surface was heated fast to 850°C in Ar (ramp rate of 120°C/min). The surface appearance was monitored continuously by *in situ* optical imagery and some steps are shown in Figure 38.

The melting and shrinkage of nickel sulfide crystals become observable from about 800°C. After 3 minutes at 850°C, liquid drops can be clearly seen, which may indicate the fusion of the crystals. After 1.1 h, the quantity of big crystals decreases abruptly. From 5.2 h to 7.3 h, the surface changes to a new texture with many yellow points. This configuration is preserved during the cooling to room temperature.

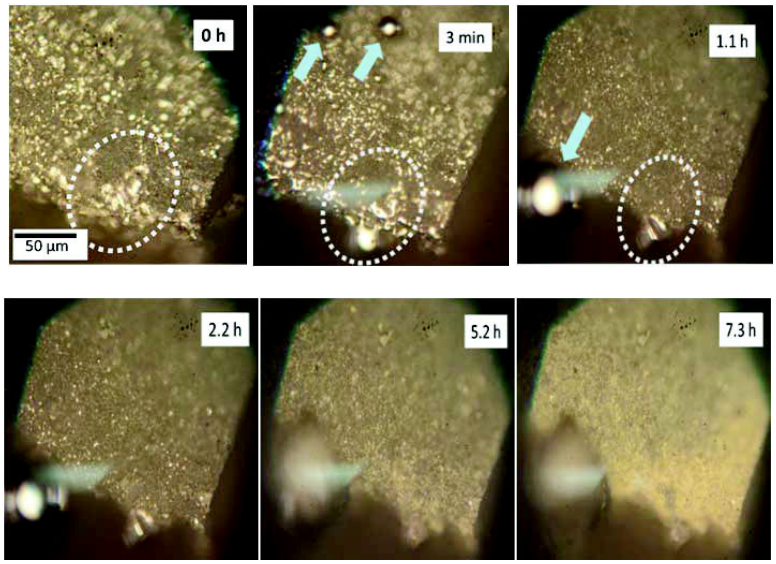

Figure 38. Evolution of surface appearance of Ni_3S_2-Ni-CGO pellet as a function of time at 850°C in Ar during 7.3 h

Figure 39 displays Raman spectra and corresponding recorded zones before (A) and after heating at 850°C (B, C, D). The yellow dots seen at 7.3 h in Figure 38 are spongy light green points in Figure 39B with the Raman peaks of CGO and NiO. The spectra taken on other zones (C, D in Figure 39) still show the presence of nickel sulfide, but with much lower Raman intensity. The presence of nickel oxide is not surprising: the Ar gas contains more than 10 ppm O_2, which means that the atmosphere is oxidizing for Ni.

After 7.3 h in Ar at 850°C, the quantity of nickel sulfide crystals at the surface decreases strongly as indicated from optical images and Raman intensity. Besides the decomposition, the fusion of the crystals could play an important role. When melting, they penetrate into the pellet substrate, leading to a decrease of the surface quantity. Detailed investigation of element/compounds distribution in the pellet interior by EDX-SEM or Raman mapping needs to be done to verify the contributions of decomposition and melting effects. Longer time of experiment is also necessary.

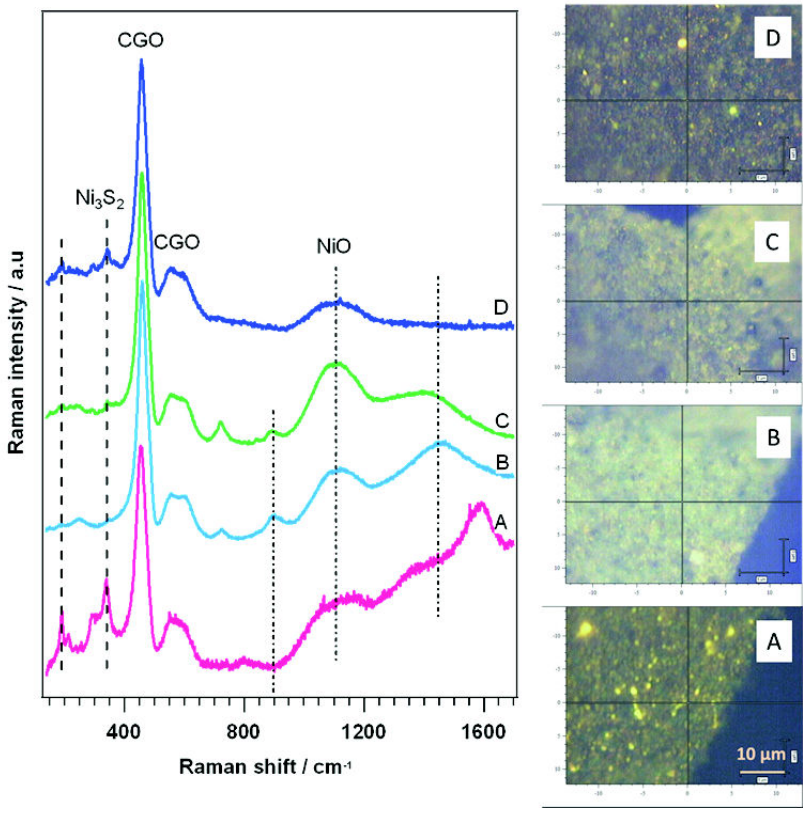

Figure 39. The morphology and corresponding Raman spectra of various positions on Ni_3S_2-Ni-CGO pellet surface before (A) and after heat treatment at different positions (B, C, D) at 850°C in Ar during 7.3 h

5.2. At 715°C in 3%H_2/Ar

A Ni_3S_2-Ni-CGO pellet was kept at 715°C in flowing 3%H_2/Ar. The surface appearance was monitored by *in situ* optical imagery, and is exhibited in Figure 40. A strange evolution happens with a vanishing of separated bright crystals, and a formation of much larger bright agglomerates. This transformation happened mostly in the first 3 hours. After 14 h, the pellet was cooled down to 50°C in the same flowing gas.

Raman spectra of the surface (Figure 41**)** show that at 50°C only the bands of CGO are observed, no Ni_3S_2 could be detected, and the big bright agglomerates seen in optical images are Ni. Investigations of the cross-section and the back surface also show the presence of CGO and Ni bands without nickel sulfide. The result was also confirmed by EDS-SEM and XRD.

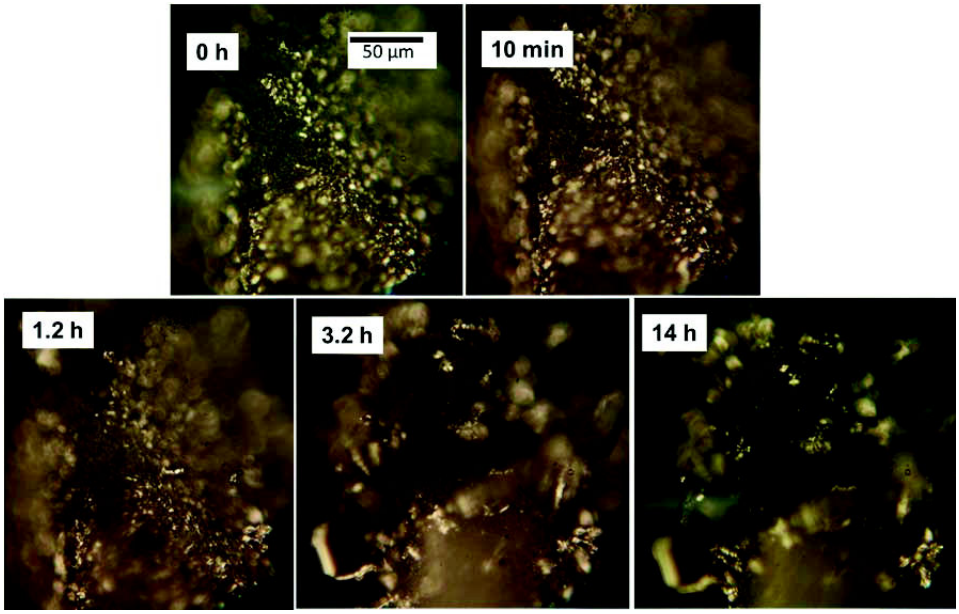

Figure 40. *In situ* optical images of a Ni_3S_2-Ni-CGO pellet as a function of time at 715°C in flowing 3%H_2/Ar

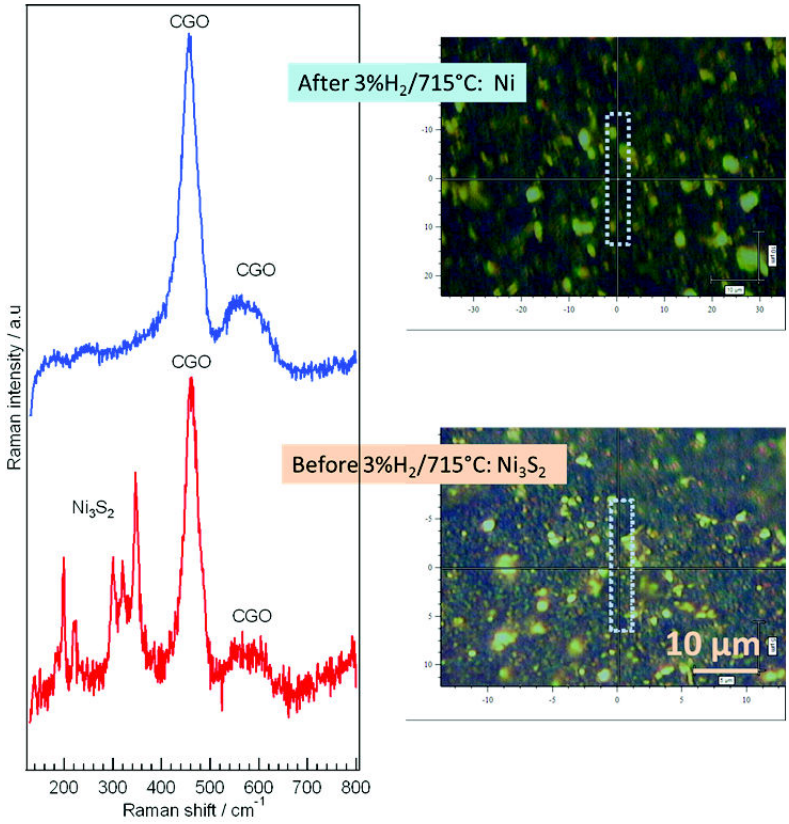

Figure 41. Raman spectra obtained before and after treatment in 3%H_2/Ar for 14 hours at 715°C

The morphology of the sample after treatment is shown in Figure 42. A porous structure with homogeneous distribution of Ni and CGO particles is obtained after sulfur removal.

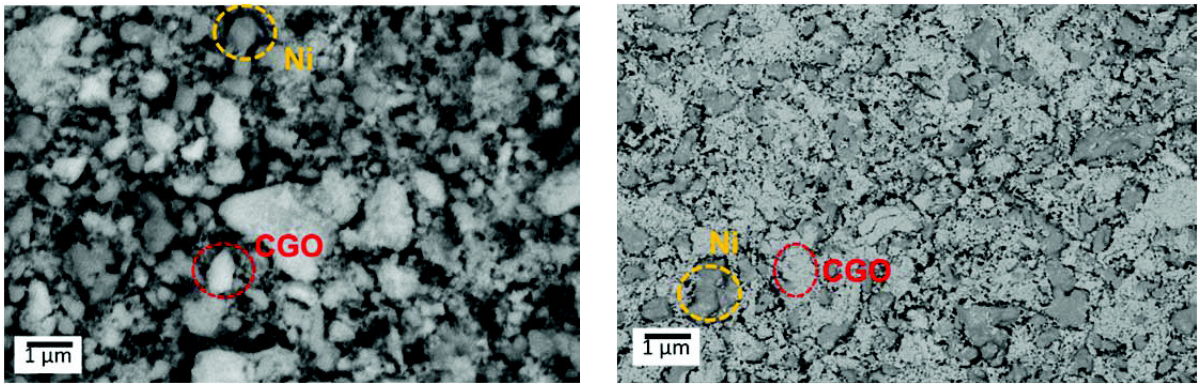

Figure 42. Morphology of the surface of Ni_3S_2-Ni-CGO pellet after being heated in 3%H_2/Ar at 715°C (left) and Ni-CGO fresh pellet (right)

In conclusion, the treatment of sulfur-containing pellet in 3%H_2 at 715°C is effective to remove sulfur and recover Ni. However, the morphology cannot be recovered completely because there exist observable agglomerates of Ni.

6. Conclusion

Nickel sulfides thermal stability:

In flowing Ar, NiS is decomposed partly to Ni_3S_2 at ~400°C whereas Ni_3S_2 is more stable with temperature. It decomposes partly at higher temperature of 850°C.

Interactions between H_2S and Ni:

a. The sulfidation of nickel can be written as following:

From 200 to 500°C, $3\ Ni + 2\ H_2S \rightarrow Ni_3S_2 + 2\ H_2$ (2)

At 200°C, $x\ Ni_3S_2 + (3y - 2x)\ H_2S \rightarrow 3\ Ni_xS_y + (3y - 2x)\ H_2$ (3)

At 200°C, $Ni_xS_y + (x - y)\ H_2S \rightarrow x\ NiS + (x - y)\ H_2$ (4)

At 800°C, no nickel sulfide is found by Raman spectroscopy, XRD.

b. From 200°C to 500°C, the formation of nickel sulfides can be detected within 1-3 hours, while no crystal can be found after 18 h at 800°C.

c. The saturation of the surface with Ni_3S_2 is obtained in less than 5 hours. This time scale lies inside the time needed to heat a SOFC to its working temperature of ~700°C. Therefore, the

poisoning may take place during the warming up stage, resulting to a fast degradation at the very beginning of SOFC operation.

d. The extent of morphological change increases with increasing temperature from 200°C to 500°C, but is minimum at 800°C. The effect of H_2S thus is said to be most severe at 500°C.

e. The extent of H_2S poisoning depends on the relative weight between 2 important factors:
   - adsorption of H_2S onto Ni, which is more favorable at lower temperature;
   - diffusion of Ni toward sulfur, which is faster at higher temperature.

   At 800°C, the adsorption is very limited. So, no nickel sulfide or no morphology change can be observed. At 500°C, the adsorption is important and the sulfur-induced diffusion of Ni is fast, which lead to the formations of very big facetted crystals.

f. H_2S can poison the anode by:
   - formation of nickel sulfides grains;
   - changing the morphology because of the H_2S-induced diffusion of Ni towards the surface.

Interactions between H_2S and Ni-CGO:

a. The sulfidation of Ni-CGO pellet depends strongly on the temperature:
   - at 200°C: NiS, Ni_3S_2 or no sulfide product have been observed as a function of depth below the surface; no observable morphology change but a fissure near the surface;
   - at 500°C: dense Ni_3S_2 layer on the pellet surface, covering the porous cermet structure inside;
   - at 715°C: big nickel sulfide crystals of 2-10 μm on the surface.

The most severe change of morphology happens at 500°C. The same phenomenon was observed with pure Ni.

b. The distribution of S as a function of depth follows a parabolic shape, with minimum value obtained at a certain depth below the surface. This implies a limited effective diffusion length of H_2S. From a technical point of view, an anode-supported SOFC may be a good choice to protect the interface anode/electrolyte, since H_2S will attack the uppermost layers.

c. High temperatures facilitate the reaction between H_2S and CGO. When a Ni-CGO pellet was exposed to 500 ppm H_2S at 715°C, two compounds CGO and Ni_3S_2 were detected. When the temperature was raised to 750-790°C, a lot of $Ce_2O_{2.5}S$ was found.

d. Treating the Ni_3S_2-containing pellet in 3%H_2 at 715°C helps to remove sulfur and recover cermet morphology partly.

REFERENCES

[1] S. P. Jiang, S. H. Chan, *J. Mater. Sci.* **2004**, *39*, 4405.

[2] M. B. Pomfret, J. C. Owrutsky, R. A. Walker, *The Journal of Physical Chemistry B* **2006**, *110*, 17305.

[3] Z. Cheng, M. Liu, *Solid State Ionics* **2007**, *178*, 925.

[4] F. Guillaume, S. Huang, K. D. M. Harris, M. Couzi, D. Talaga, *J. Raman Spectrosc.* **2008**, *39*, 1419.

[5] D. W. Bishop, P. S. Thomas, A. S. Ray, *Materials Research Bulletin* **2000**, *35*, 1123.

[6] Z. Cheng, H. Abernathy, M. Liu, *J. Phys. Chem. C* **2007**, *111*, 17997.

[7] H. Okamoto, *J. Phase Equilib. Diffus.* **2009**, *30*, 123.

[8] J.-H. Wang, Z. Cheng, J.-L. Bredas, M. Liu, *The Journal of Chemical Physics* **2007**, *127*, 214705.

[9] G. Shen, D. Chen, K. Tang, C. An, Q. Yang, Y. Qian, *J. Solid State Chem.* **2003**, *173*, 227.

[10] H. Kiuchi, K. Funaki, T. Tanaka, *MTB* **1983**, *14*, 347.

[11] H. Rau, *J. Phys. Chem. Solids* **1976**, *37*, 929.

[12] A. Lussier, S. Sofie, J. Dvorak, Y. U. Idzerda, *Int. J. Hydrogen Energy* **2008**, *33*, 3945.

[13] D. S. Monder, K. Karan, *J. Phys. Chem. C* **2010**, *114*, 22597.

[14] C. H. Bartholomew, P. K. Agrawal, J. R. Katzer, *Adv. Catal.* **1982**, *31*, 135.

[15] J. R. McBride, K. C. Hass, B. D. Poindexter, W. H. Weber, *J. Appl. Phys.* **1994**, *76*, 2435.

[16] C. Sourisseau, R. Cavagnat, R. Mauricot, F. Boucher, M. Evain, *J. Raman Spectrosc.* **1997**, *28*, 965.

[17] M. Pihlatie, A. Kaiser, M. Mogensen, *Solid State Ionics* **2009**, *180*, 1100.

[18] M. Pihlatie, A. Kaiser, P. H. Larsen, M. Mogensen, *J. Electrochem. Soc.* **2009**, *156*, B322.

Chapter 4
Effect of H_2S on electrochemical properties of SOFC anode

CONTENTS

1. Introduction

The oxidation of fuel on a SOFC anode comprises a complex series of physical, chemical, and electrochemical processes. To increase the anode conversion efficiency and its resistance towards pollutants, it is necessary to identify the rate-determining processes as well as the most H_2S-sensible processes. Many studies have been done, from a real anode to simplified geometry one; however, the reported results do not reveal a clear picture on the oxidation pathways [1-5]. The anode electrochemical properties seem to be specific to a lab since they depend on many parameters like anode microstructure (therefore anode preparation methods/environment), measurement configuration/parameters, fuel composition, temperature, and impurities [6,7].

The most widely investigated concentration and temperature ranges are 0.1-10 ppm H_2S and 700-1000°C, since they are the most realistic and applicable conditions of SOFC operation [8]. However, in these conditions, it is difficult to couple electrochemical techniques with molecular scale investigation by Raman spectroscopy, since no Raman spectra of nickel sulfides can be obtained at temperatures higher than 500°C. Together with the fact that the poisoning effect is the most severe at 500°C, we chose to work at 500°C. The samples used were the commercial half-cells Ni-YSZ/YSZ. An advantage of using commercial cells is a much better reproducibility from sample to sample. This advantage becomes very important when comparisons must be made between different treatments. Unfortunately, half cells with Ni-CGO anodes were not available. Therefore, we chose to use cells with Ni-YSZ anodes, despite the fact that it would have been more coherent to continue with the half-cells Ni-CGO/CGO.

The chapter first looks back in the literature on the H_2S-induced changes of electrical parameters and on the proposed equivalent electrical circuits. Next, it presents a theoretical impedance model based on the Volmer-Heyrovsky reaction mechanism which allows to reproduce the experimental impedance spectra. The behaviors of the anode in clean fuel and in polluted fuel are then discussed based on the evolutions of impedance spectra shapes, and on the fitted parameters. Correlations between electrical properties and the build-up of nickel sulfide detected by Raman spectroscopy are also disclosed.

2. Review of impedance studies on the effects of H_2S on SOFCs

The electrochemical properties of SOFCs have mostly been studied by complex impedance, dc polarization, and current interruption techniques. In most cases, the poisoning effect of H_2S was determined through changes in the cell power output, cell voltage/current at constant current/voltage, or anode polarization resistance [9-12].

Table 1 indicates how impedance spectra have been used to extract electrical properties and to clarify the rate-determining processes at a SOFC anode from the literature. It can be seen that the interpretations of impedance spectra by electrical equivalent circuits are still ambiguous and divergent, e.g. the low frequency part was assigned to either gas phase diffusion or adsorption of charged/uncharged species, and no further information was obtained. This reflects the complex nature of the oxidation mechanism at the anode. The situation is still more complicated in the presence of H_2S.

Table 1. Interpretations of impedance data from the literature.

Cell	EIS	Interpretation	Ref.	Remarks
NiO-CGO (35 µm)/YSZ (140 µm)/ NiO-CGO (35 µm)	* 4%H_2O-H_2, 9 ppm H_2S, 850°C during 1.5 hours * OCP 10^5-10^{-1} Hz	* $R_sL(RQ)_1(RC)_2W$ * LF: gas diffusion across a stagnant gas layer adjacent to anode ➔ finite-length Warburg Diffusion resistance R_W are expected not to change with few ppm pollutant added * HF + MF: probably originate from processes at surface or bulk of anode * R_s = electrolyte + contact res. * $R_{pol} = R_1 + R_2 + R_W$ * No variation of R_1, R_2, R_w under 9 ppm H_2S	[13]	No assignment for HF, MF
Ni-CGO (~800 nm)/ CGO/ Ni-CGO	* H_2:N_2=1:4, 3% H_2O 450-600°C * OCP 10^5-1 Hz	* HF intercept = electrolyte resistance R_s (depends on electrolyte material, scales linearly with electrolyte thickness, independent of dc bias) * Electrode pol. resistance R_p = difference between LF intercept and electrolyte resistance. * R_p is mainly determined by the grain size and microstructure of the cermets * R_p of nano-grained thin film electrodes ≈ state-of-the-art thick film cermet anodes	[14]	No ECQ

Cell	EIS	Interpretation	Ref.	Remarks
Ni wire/YSZ/ Pt, Pt ref	* Air (cathode side) * H_2-H_2O (anode side) * 1000°C * OCP, polarized electrode 10^5-5.10^{-3} Hz	* Ignore diffusion limitations * Equivalent circuit comprising two adsorbed species A, B can well reproduce spectra * $R_p = R_{ct} + R_2R_3 /(R_2 + R_3)$ R_{ct}: charge-transfer resistance R_2, R_3 are defined by combinations of the linearization coefficients, implying interactions between processes involving the species A and B, i.e. adsorption, desorption, charge transfer reaction and, possibly chemical reactions between the adsorbed species * R_p, R_{ct}, R_2, R_3 vary with pH_2O, pH_2 ➔ A, B most probably are adsorption products formed by H_2 and H_2O * $R_{ct} << R_p$ ➔ charge transfer process does not govern Faradaic impedance, instead chemical processes related to 2 adsorbed species .	[1]	Rate limiting processes are unknown
Ni-YSZ(30 µm)/YSZ/ Pt, Pt ref.	2 or 1 atm setup * air * H_2-H_2O varied * 850-1000°C * OCV, 50mV 65.10^3-10^{-2} Hz	* $R_sL(RQ)_{HF}(RQ)_{MF}(RC)_{LF}$ L is not restricted in any fit R_s = electrolyte resistance between reference and anode * HF (>1 kHz): sensitive to cermet structure (particle size) and temperature, insensitive to pH_2, pH_2O and anodic overvoltage Q = double-layer capacitance of Ni/YSZ interface R_{HF} = transfer resistance of charged species (proton, O^{2-}) across Ni/YSZ and in YSZ. * MF (100Hz-10Hz) and LF (10Hz-0.1Hz): exhibit no thermal activation, sensitive to pH_2, pH_2O and anodic overvoltage * MF (100Hz-10Hz): gas diffusion in a millimeter thick volume above the anode surface. Gas diffusion is observed on high-performance Ni-YSZ anode only, since diffusion resistance is very small <0.15 Ω cm^2 at 1000°C in H_2 with 3%H_2O. Gas diffusion inside the porous anode is negligible. * C_{LF} = 0.5 to 2.5 F/cm^2, very sensitive to H_2O ➔ indicating absorbed charged species.	[15,16]	
Ni-YSZ/YSZ (3 mm)/Ni-YSZ	* 20%H_2-4%H_2O-Ar * OCP * 800°C 10^4-10^{-3} Hz	3 semicircles * HF (10kHz): sensitive to electrode morphology, not to P_{H2} or H_2O * MF (100Hz): depend on P_{H2} and H_2O ➔ main rate-limiting process, may be H_2 oxidation. * $R_{pol} = R_{HF} + R_{MF}$ * LF (1Hz): LF contribution is very small➔cannot estimate with accuracy➔negligible	[17]	

Cell	EIS	Interpretation	Ref.	Remarks
Ni,Pt,Au wires/ $YSZ_{single\ crystal,smooth\ surface}$ / Pt, Pt ref.	* x%H_2-1%H_2O * 600-850°C * polarizing cycle included -500 - 500 mV 64.10^3-5.10^{-2} Hz	$R_s(C_1[R_1(R_2Q_2)])$ * R_s ➔ bulk conductivity of electrolyte * HF (peak frequency 10^4 -10^3 Hz): nonfaradaic processes C_1=20-200 µF/cm^2 ➔ double-layer + adsorption capacitance * LF (peak frequency 0.5 -50 Hz): R_2Q_2, may related to adsorbed oxide species * Inductive loop attributed to the passivation of Ni at overpotentials higher than 200 mV	[3]	Focus on HF only.
Ni-YSZ (35µm)/ YSZ (0.9 mm) /Pt, Pt ref	* 2 atm * 10-98%H_2-2%H_2O * 800-1000°C, OCP * 1000°C, different current densities 10^5-1 Hz	$R_s(RQ)_1(RQ)_2$ * total electrode resistance = distance between low and high frequency intercept * HF: conductivity ($1/R_1$) depends on T, η ; C_1= 88 µF/cm^2, independent of P_{H2}, P_{O2} ➔ Hydrogen transfer from Ni to YSZ surface, followed by a charge transfer process on YSZ electrolyte * LF: conductivity ($1/R_2$) is independent of T, η but depend on P_{H2O}, C_2 = 0.4 F/cm^2 ➔ adsorption or surface diffusion process on Ni surface of uncharged hydrogen species	[5]	
NiO-CGO/ YSZ/ LSM-YSZ	* 2 atm * cell exposed to 49%H_2 -2%H_2O-0.5 ppm H_2S, recovered in clean fuel successively at 0.05, 0.10, 0.15 A cm^{-2} * 715°C 10^4-5.10^{-2} Hz	$R_s(RQ)_{HF}(RQ)_{LF}$ * HF: R_{HF} unchanged during the experiment * R_s increases with time ➔ background degradation in the cell * LF (1Hz): R_{LF} decreases as current increased; resistance increase under H_2S is less at higher current density operation since higher current brings more O^{2-} to oxidize sulfur: $S_{ads} + 2O^{2-} \rightarrow SO_{2gas} + 4e^-$	[8]	

3. General analysis of impedance spectra obtained at 500°C

3.1. Typical shapes of impedance spectra

Figure 1 shows typical Impedance Spectra (IS) of the half-cell at different polarizing voltages at 500°C in the flow of 3%H_2/3%H_2O in Ar. At least three relaxation processes corresponding to three local maxima can be identified in three frequency ranges from Bode plots:

1. High frequencies range (HF): above 6-10 kHz
2. Medium high frequencies range (MF): 10 kHz-10 Hz
3. Low frequencies range (LF): below 10 Hz

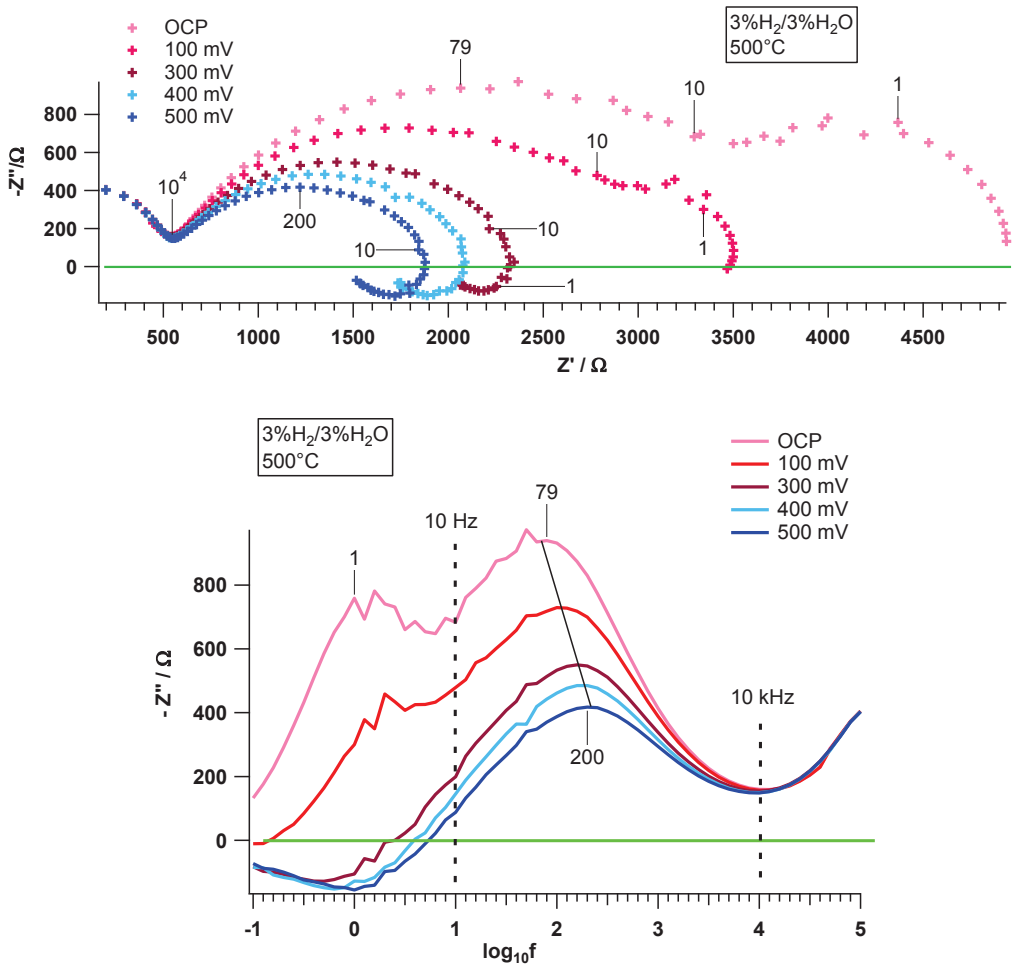

Figure 1. Nyquist and Bode plots at various dc polarizing voltages at 500°C in flowing 3%H_2/3%H_2O in Ar

The HF part is an incomplete arc and independent of dc applied voltage. The same shape was obtained and was attributed to the electrolyte by Muecke et al. [14]. While the physical meaning of MF is still not clear from literature, the LF part is mostly suggested to be due to adsorption of either charged/uncharged species or surface diffusion of hydrogen species (see Table 1). As the voltage increases, the spectrum decreases in size. Above 300 mV, the LF capacitive arc

transforms to an inductive one. This inductive loop was also observed by Kek et al. at higher than 200 mV, but was not treated further [3]. The shape of LF part is very similar to the one constructed by a second-order concentration impedance developed by Diard et al. [18]. This impedance is derived from Volmer-Heyrovsky reaction mechanism and is discussed in detail in the following section.

A classic, but not often used, method to check if the impedance diagram is complete is to compare the ω→0 real part of the impedance with the first derivative of the U(I) curve. Figure 2 shows both values as a function of the applied voltage. The two values are coincident for 300-500 mV, indicating that the frequency ranges used can cover well all the processes. At OCP and 100 mV, however, the values read from LF intercept are higher than those obtained from U(I) curve. This is an indication that the the two impedance spectra may not be complete within the frequency range used.

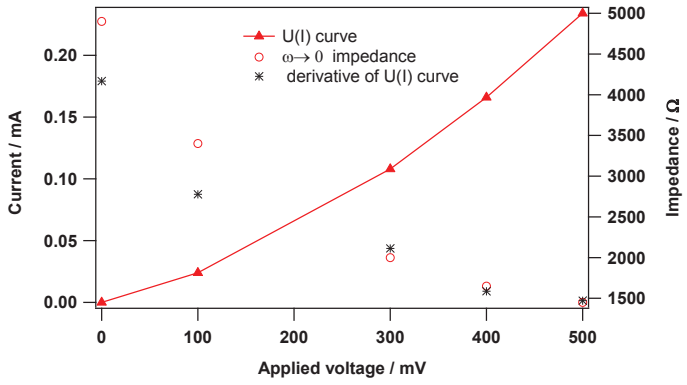

Figure 2. The ω→0 real part of the impedance and the first derivative of the U(I) curve at different applied voltages at 500°C in flowing 3%H_2/3%H_2O/Ar

3.2. Structure and shape of concentration impedance

The Volmer-Heyrovsky reaction mechanism includes at least two monoelectronic steps, an electrolyte species A^+, and adsorbed phases including free sites s, two adsorbed species with different chemical nature A_s, A_{2s}. The mechanism is written in reduction direction as follows:

$$A^+ + s + e^- \overset{K_1}{} A_s \qquad (1)$$

$$A^+ + A_s + e^- \overset{K_2}{} A_{2s} \qquad (2)$$

$$A_{2s} \overset{k_3}{} A_2 + s \qquad (3)$$

The rate of each step is described as:

$$v_1 = K_1 \Gamma \theta_s \quad (4)$$

$$v_2 = K_2 \Gamma \theta_{As} \quad (5)$$

$$v_3 = k_3 \Gamma \theta_{A_{2s}} \quad (6)$$

$$[A^+] = \text{const} \quad (7)$$

$$K_1 = k_1 [A^+] exp \frac{1-b_1 F}{RT} \eta \quad (8)$$

$$K_2 = k_2 [A^+] exp \frac{1-b_2 F}{RT} \eta \quad (9)$$

where:

Γ: total number of free and adsorbed sites

θ_i: coverage fraction of adsorbate i

b: symmetry factor in the anodic direction

η: overpotential applied to the working electrode

The density of the faradaic current is:

$$i_f = -F(v_1 + v_2) \quad (10)$$

Eq. 10 shows that the current density is a function of the electrode overpotential η, coverage fraction of free site s and adsorbed A_s

$$\Delta i_f = \frac{\partial i_f}{\partial \eta} \Delta \eta + \frac{\partial i_f}{\partial \theta_s} \Delta \theta_s + \frac{\partial i_f}{\partial \theta_{As}} \Delta \theta_{As} \quad (11)$$

Consequently, the Faradaic impedance Z_f is the sum of transfer resistance R_t, impedance of free sites Z_s and impedance of adsorbed A Z_{As}:

$$Z_f = \underbrace{\frac{1}{\left(\frac{\partial i_f}{\partial \eta}\right)}}_{R_t} \underbrace{- \frac{\left(\frac{\partial i_f}{\partial \theta_s}\right)}{\left(\frac{\partial i_f}{\partial \eta}\right)} \frac{\Delta \theta_s}{\Delta i_f}}_{Z_s} \underbrace{- \frac{\left(\frac{\partial i_f}{\partial \theta_{As}}\right)}{\left(\frac{\partial i_f}{\partial \eta}\right)} \frac{\Delta \theta_{As}}{\Delta i_f}}_{Z_{As}} \quad (12)$$

Z_s and Z_{As} are called concentration impedances whose normalized forms are rational functions of p (Eq. 13). The denominators are second-order functions of p since the adsorbed phase includes three species. The numerators are first-order in p when the two symmetry factors are different.

$$Z_x = \frac{R_x(1+\tau_3 p)}{1+2\zeta\tau p+(\tau p)^2} \qquad (13)$$

Where x represents s or A_s, τ is time constant, ζ is a damping coefficient and R_x is concentration resistance.

When the two poles are real (as |ζ| is greater than 1), the concentration impedance is expressed as:

$$Z_x = \frac{R_x(1+\tau_3 p)}{(1+\tau_1 p)(1+\tau_2 p)} \qquad (14)$$

In frequency domain, p is equal to jω and τ to 1/(2πf).

The Nyquist shape depends on the relative magnitude among three time constants/characteristics frequencies as displayed in Figure 3, while R_x is a proportionality factor.

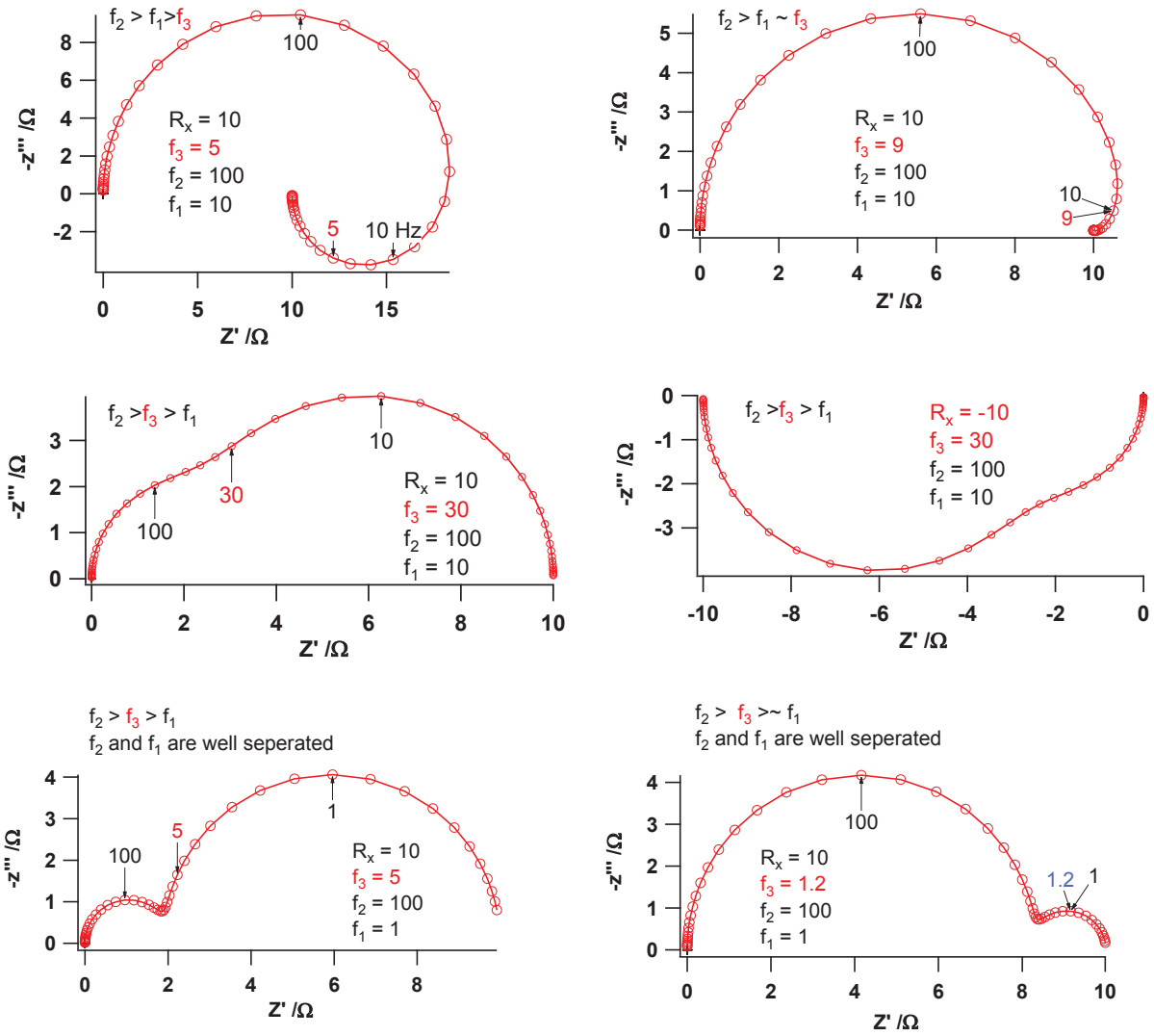

Figure 3. Some possible shapes of second-order concentration impedance calculated from Eq. 14 using Igor software

3.3. Proposed equivalent circuit

By conducting a semi-empirical study, Vogler et al. [19] suggested a possible oxidation process based on eqs. 15-20. According to the authors, the bulk-surface exchange step to create surface adsorbed species O_{YSZ}^{2-} (Eq. 15) and the dissociative adsorption of H_2 on Ni surface to create H_{Ni} (Eq. 16) almost do not limit the cell current. The rate-determining processes were proposed to be hydrogen spillovers to YSZ surface (Eq. 17, 18), water desorption from YSZ (Eq.19), surface diffusion of adsorbed hydroxyl ions on YSZ and water dissociation on YSZ (Eq.20).

$$\boldsymbol{O_{o\,YSZ}^{X} + s_{YSZ} \rightarrow O_{YSZ}^{2-} + V_{o\,YSZ}^{\cdot\cdot}} \quad (15)$$

$$\boldsymbol{H_{2,gas} + 2s_{Ni} \rightarrow H_{Ni}} \quad (16)$$

$$\boldsymbol{H_{Ni} + O_{YSZ}^{2-} \overset{K_1}{} OH_{YSZ}^{-} + e_{Ni}^{-} + s_{Ni}} \quad (17)$$

$$\boldsymbol{H_{Ni} + OH_{YSZ}^{-} \overset{K_2}{} H_2O_{YSZ} + e_{Ni}^{-} + s_{Ni}} \quad (18)$$

$$\boldsymbol{H_2O_{YSZ} \overset{k_3}{} H_2O_{gas} + s_{YSZ}} \quad (19)$$

$$\boldsymbol{H_2O_{YSZ} + O_{YSZ}^{2-} \rightarrow 2OH_{YSZ}^{-}} \quad (20)$$

We assume that the governing processes on the anode are eq. 17-19. Since there are almost no concentration gradients for large distances from the TPB [19], the concentrations of H_{Ni} and O^{2-}_{YSZ} at the TPB can be assumed to be constant. Then, the oxidation process is controlled by 2 monoelectronic steps with H_{Ni} acting as A^+ species in the above Volmer-Heyrovsky model and $OH_{YSZ}^{-}, H_2O_{YSZ}, s_{YSZ}$ as three main adsorbed phases. This mechanism turns out to be that of Volmer-Heyrovsky. So the faradaic impedance will include a charge transfer resistance and one or two concentration impedances $Z_{conc.}$ of the form:

$$\boldsymbol{Z_{conc,x} = \frac{R_{conc,x}(1+\tau_3 p)}{(1+\tau_1 p)(1+\tau_2 p)} = \frac{R_{conc,x}\ 1+j\frac{f}{f_{conc,num}}}{1+j\frac{f}{f_{conc,den1}}\ \ 1+j\frac{f}{f_{conc,den2}}}} \quad (21)$$

Where x = s_{YSZ}, OH_{YSZ}^{-}; $f_{conc,num}$ and $f_{conc,den}$ are characteristic frequencies of the numerator and the denominator respectively.

As the impedance spectra obtained in our study consist of at least 3 arcs, we propose the following equivalent circuit to interpreter the spectra:

$$\mathbf{R_1(R_2C_2)(R_3Q_3)Z_{conc}}$$

where $R_1(R_2C_2)$ represents the high frequency range (> 10 kHz) relating to ohmic drop in the electrolyte between WE and REF; (R_3Q_3) is "depressed parallel RC" as described in Chapter 2, representing the charge transfer process at medium frequency range; it consists in a capacitance C_3 which is assigned to the double layer capacitance of zirconia electrolyte and a charge transfer resistance R_3. Z_{conc} is the concentration impedance of adsorbed species at low frequency range.

It should be mentioned that compared to what proposed by Vogler et al. [19], two rate-determining processes (OH^-_{YSZ} surface diffusion and water dissociation on YSZ) are ignored here. In Ni, all the diffusion/chemical reactions happen fast, imposing almost no influence on the overall kinetics. This hypothesis needs to be reconsidered once H_2S is added to the clean fuel, because Ni may become nickel sulfide which has lower conductivity and catalytic activity compared to pure Ni [20], resulting to a slow-down of Ni-related processes. Therefore, the oxidation model and the equivalent circuit above may need to be modified.

4. Characterization of anode initial state at 500°C in clean fuel

Two half-cells of the same series supplied by Kerafol have been used; one for the study at 500 mV (500mV-cell) and one for the study in OCP conditions (OCP-cell). Each cell has been first characterized at 500°C at different polarizing voltages in clean fuel, i.e. in flowing $3\%H_2/3\%H_2O/Ar$.

4.1. 500mV-cell

Figure 4 displays the impedance spectra of 500mV-cell at different polarizing voltages. As the voltage increases, the $\omega \rightarrow 0$ resistance decreases strongly, indicating a considerable decrease of the cell polarization resistance. The MF peak frequency shifts to higher values (from 63 Hz to 200 Hz) while the LF part changes from capacitive to inductive one. The HF part remains unchanged and is independent of the applied voltages (at a given temperature).

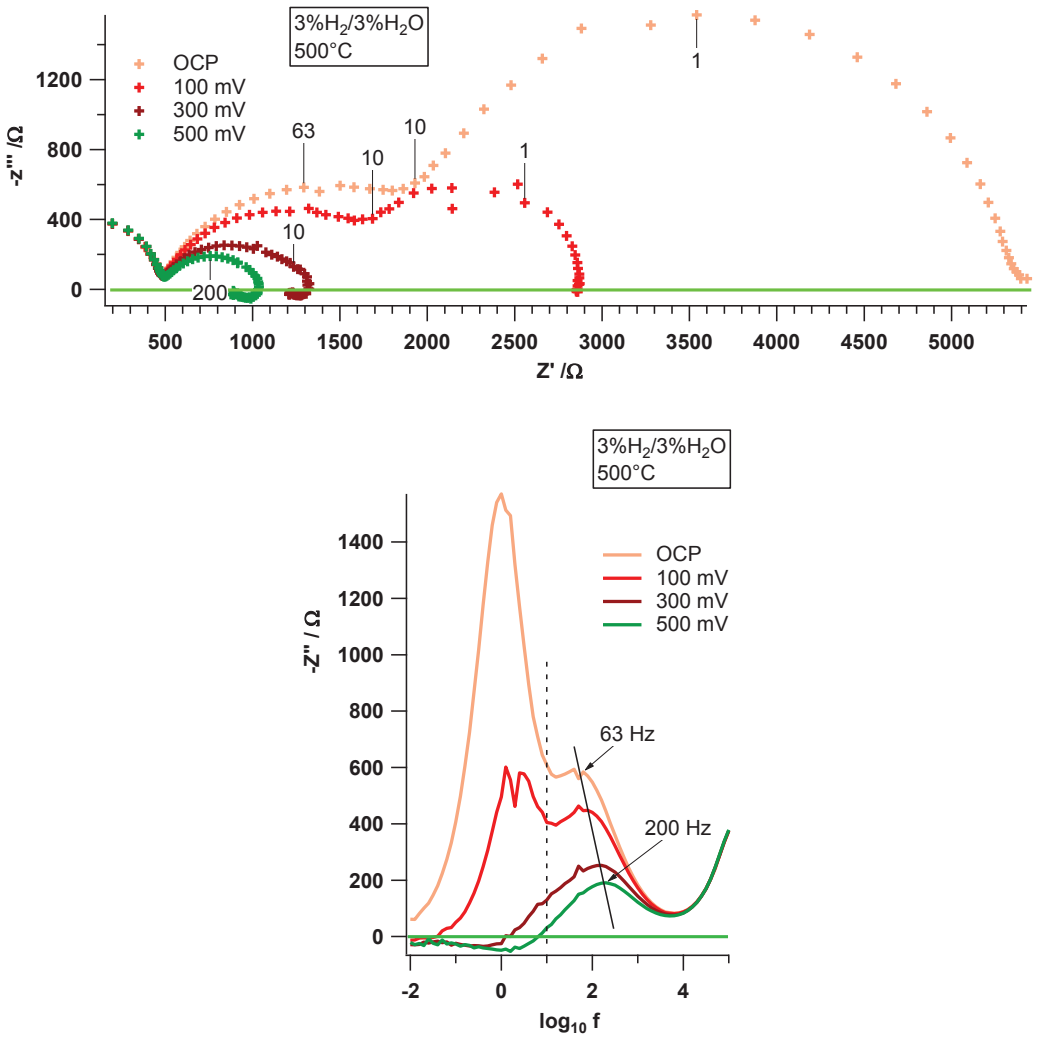

Figure 4. Nyquist and Bode plots at dc voltages from OCP to 500 mV of 500 mV-cell

The spectra have been interpreted by the circuit $R_1(R_2C_2)(R_3Q_3)Z_{conc}$ mentioned above. Good fits to experimental data have been obtained as shown in Figure 5.

The intercept of HF part with the real axis at about 10^4 Hz, i.e $R_1 + R_2$, is attributed mostly to the non-zero electrolyte resistance which induces an ohmic drop between the reference and the working electrodes. From the values of $R_1 + R_2$, the activation energy measured in the temperature range of 500-715°C and the ionic conductivities at various temperatures are calculated and given in Table 2. In our case, the electrolyte resistance is assimilated to a cylinder having the area of the working electrode and the thickness of the electrolyte. The values obtained in our work are in the same order of magnitude as the reported values for tetragonal zirconia. Since this HF part does not change with the applied voltage, it is ignored in further analysts.

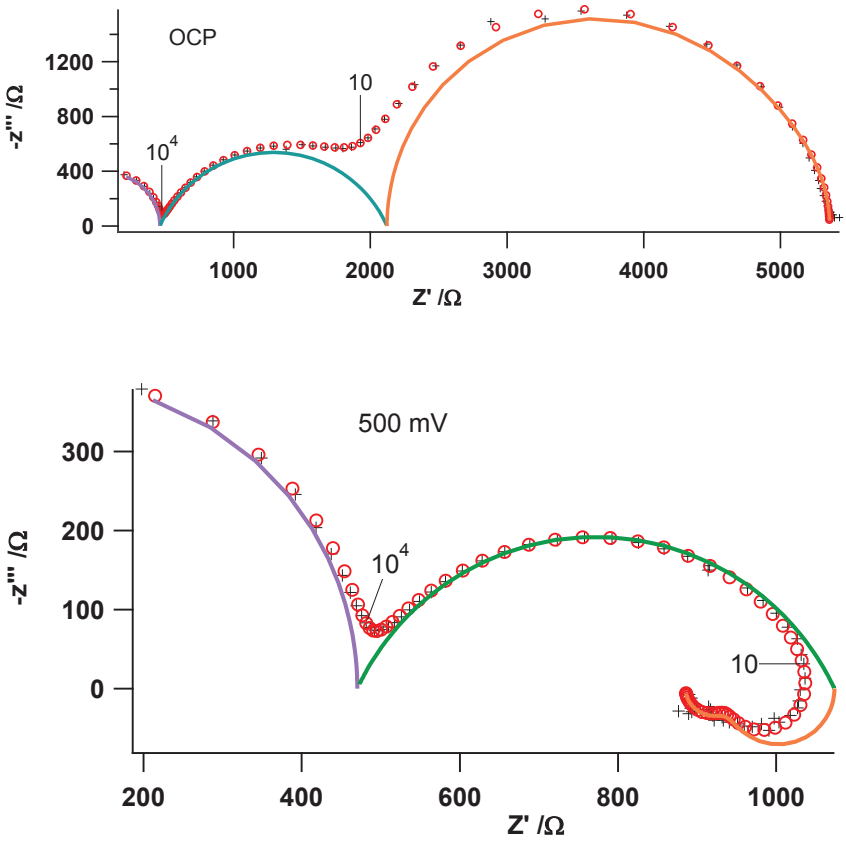

Figure 5. The fitted results for IS at OCP and 500 mV (Black mark: experimental data, red circle: fitted data, colored lines: sub-circuits)

Table 2. Ionic conductivity of 3YSZ (S/cm) of 500 mV-cell

Ref.	Our work	[21]	[22]	[23]
1000°C	4.3×10^{-2} E_a = 79 kJ/mol	4.9×10^{-2} E_a = 77 kJ/mol	6.5×10^{-2} E_a = 72 kJ/mol	6.3×10^{-2}
800°C	1.1×10^{-2}		1.8×10^{-2}	1.6×10^{-2}
500°C	3.2×10^{-4}			

The values of each circuit elements corresponding to MF and LF parts are given in Table 3. The transfer resistance R_3 decreases and the corresponding characteristic frequency f_3 increases with polarizing voltages. So higher voltage will create higher driving force for electron transfer, so the resistance decreases and the relaxation process happens faster. The double layer capacitance C_3 remains constant. For the concentration impedance, the negative value of R_{conc} implies the formation of inductive loop at 300, 500 mV. The value of this resistance also decreases with voltages.

Table 3. Fitted parameters characterizing the initial state of the 500 mV-cell

mV	R_3/Ω	f_3/Hz	n_3	C_3 /10^{-6} F	R_{conc}/Ω	$f_{conc,num}$ /Hz	$f_{conc,den1}$ /Hz	$f_{conc,den2}$ /Hz
OCP	1661.58	63.26	0.73	1.51	3238.52	0.26	0.24	1.02
100	1373.01	76.45	0.71	1.52	1012.57	0.05	0.05	1.74
300	911.75	104.31	0.65	1.67	-167.55	0.03	0.02	0.53
500	603.38	178.83	0.72	1.47	-187.95	0.13	0.10	1.9

4.2. OCP-cell

Figure 6 presents the impedance spectra obtained from the OCP-cell at various dc polarization voltages at 500°C. The same evolution of spectrum shape in function of voltage is seen as with the 500mV-cell.

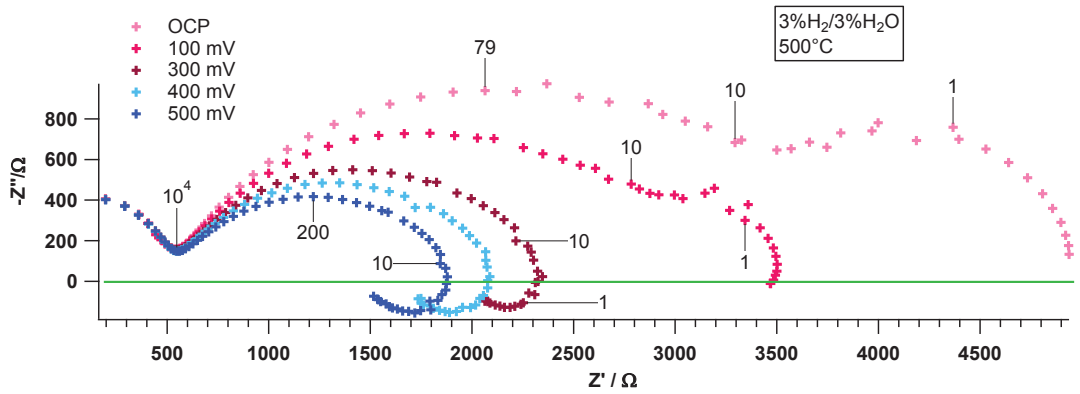

Figure 6. Nyquist plots at various polarizing voltages at 500°C in clean fuel of the OCP-cell

The fitted parameters are given in Table 4. As expected, the charge transfer resistance R_3 decreases and f_3 increases with increasing polarizing voltages. However, the frequency power n_3 is low (~0.65), which indicates that the MF arc may include two processes with the same order of magnitude of relaxation frequencies. Compared to the 500mV-cell, R_3 of OCP-cell is nearly 2 times higher, while the characteristic frequency is nearly the same.

Table 4. Fitted parameters characterizing the initial state of the OCP-cell.

mV	R_3/Ω	f_3/Hz	n_3	$C_3/10^{-6}$ F	R_{conc}/Ω	$f_{conc,num}$/Hz	$f_{conc,den1}$/Hz	$f_{conc,den2}$/Hz
OCP	3277.82	72.57	0.66	0.67	1228.13	1.62	0.81	2.54
100	2584.17	100.98	0.65	0.61	377.29	0.11	0.14	1.89
300	1958.10	136.92	0.65	0.59	-426.26	0.29	0.20	1.04
400	1721.22	156.91	0.66	0.59	-497.56	0.48	0.31	1.62
500	1505.28	182.64	0.65	0.58	-494.82	0.42	0.30	1.79

4.3. Discussion

The electrolyte resistances of 3YSZ, characterized by R_1+R_2, are very close for OCP-cell and 500 mV-cell. The activation energy for the ionic conduction and the ionic conductivity of 3YSZ agree well with those from the literature.

Since the two cells are in the same series supplied by Kerafol, they are expected to have the same resistance. However, a size difference observed in impedance spectra for MF and LF parts may indicate that the cell electrochemical properties depend on the preparation of the anode/cathode/reference electrodes. Also, it is known that a critical parameter of fuel cell efficiency is the load applied to the current collectors. In our case the load applied to the platinum grid above the working electrode cannot be controlled.

5. Effect of H_2S on 500 mV-polarizing cell (500mV-cell) at 500°C

5.1. Aging behavior in clean fuel

The cell was polarized permanently at 500 mV during ~157 h in $3\%H_2/3\%H_2O$/Ar, and the impedance spectra were recorded with a dc bias of 500 mV/ref. A qualitative analyst from Figure 7 shows that the MF and LF parts enlarge continuously with time, indicating an increase of cell impedance even in clean fuel at 500°C. Bode plot reveals a clear shift of the MF peak frequency to lower values (from 200 to 100 Hz), thus a slower kinetic of the MF process.

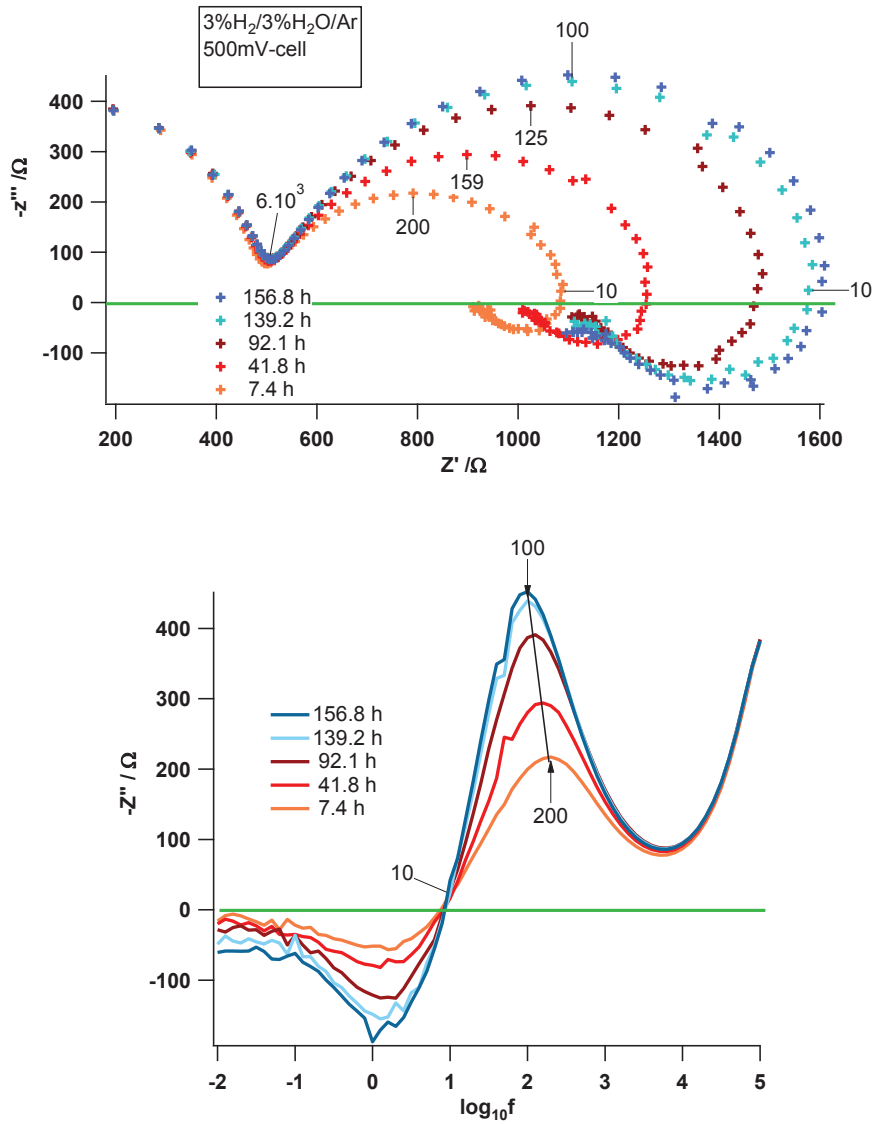

Figure 7. Nyquist and Bode plots of 500mV-cell recorded at 500°C in clean fuel as a function of time

The spectra were fitted to the previously proposed equivalent circuit (see part 3.3). An example given in Figure 8 shows that the circuit chosen can reproduce the experimental data quite well.

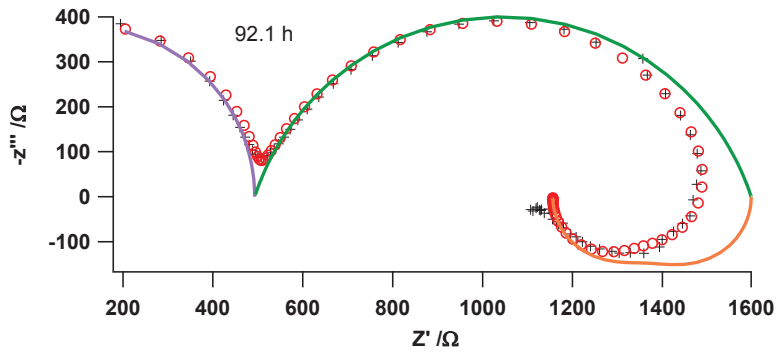

Figure 8. The fitted result for spectrum after 92.1 h in clean fuel of 500 mV-cell (Black mark: experimental data, red circle: fitted data, colored lines: sub-circuits)

Some fitted values are given in Table 5. The frequency power n_3 is about ~0.8, thus $(RQ)_3$ could be considered to represent one process i.e. charge transfer as proposed.

Table 5. Fitted parameters characterizing the 500 mV-cell in clean fuel with time.

Time/h	R_3/Ω	f_3/Hz	n_3	C_3 10^{-6} F	R_{conc}/Ω	$f_{conc,num}$ /Hz	$f_{conc,den1}$ /Hz	$f_{conc,den2}$ /Hz
7.4 h	655.34	186.46	0.75	1.30	-204.84	0.46	0.31	2.98
41.8 h	836.08	154.90	0.78	1.23	-297.71	0.50	0.34	3.17
92.1 h	1104.41	121.13	0.80	1.19	-441.11	1.26	0.75	5.05
139.2 h	1231.41	100.99	0.80	1.28	-550.02	1.17	0.73	4.79

Detailed evolutions of sub-circuit parameters are shown in Figure 9. The current flowing through the cell at 500 mV is also shown. It can be seen that the current diminishes continuously during 90 h before becoming rather stable. This trend can be well explained by the increase of the transfer resistance R_3, which shows the same trend vs time. The characteristic frequency f_3 and the concentration resistance R_{conc} also decrease fast at first and then slower. It should be noted that R_{conc} shows negative values, which reflects the adsorption phenomenon. The fitted parameters all demonstrate the degradation of the half-cell, which may be due to the loosening of the contact between current collector and anode as observed by Brightman et al. [8]. Others possibilities to take into account are the partial oxidation of nickel at high potentials (see 9. Discussion) and/or the instable nature of the porous structure.

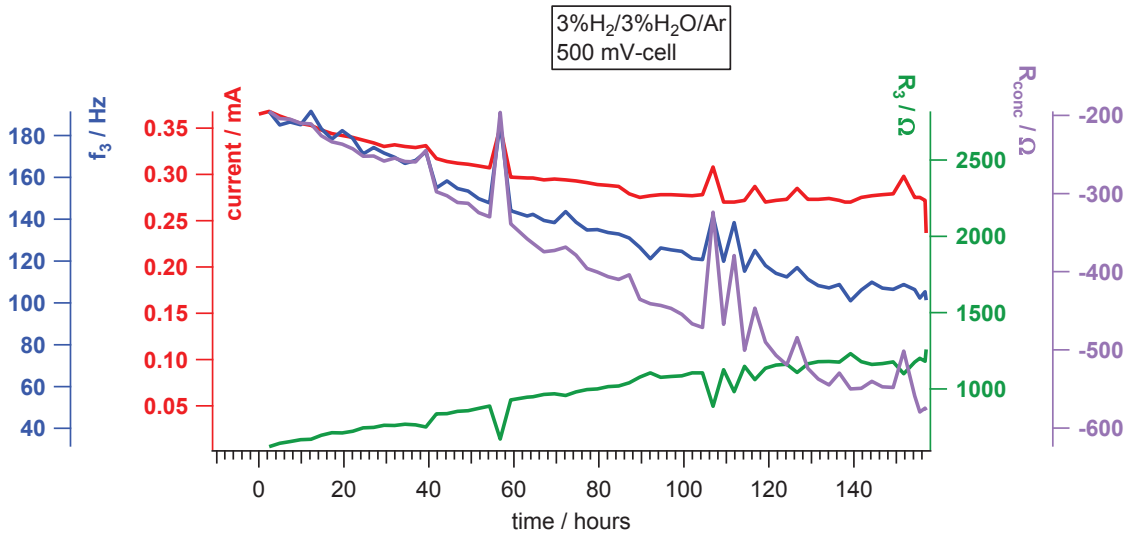

Figure 9. Correlations between the current and circuit parameters of 500 mV-cell in clean fuel at 500°C

5.2. Effect of H_2S on the electrical properties

As soon as H_2S was introduced to the system (200 ppm), a remarkable change happens with the LF part of the impedance diagram. From Figure 10, it seems that the inductive loop at the beginning rolls clockwise to become a capacitive arc at 1.3 h, and then the arc continues to turn to form distorted inductive arcs from 2.5 h. From 16 h on, the spectra become enormously big, indicating a very high resistance of the sample. The continuous transformation of impedance shapes may indicate different extent of H_2S poisoning, e.g. the position and the thickness of nickel sulfide layer.

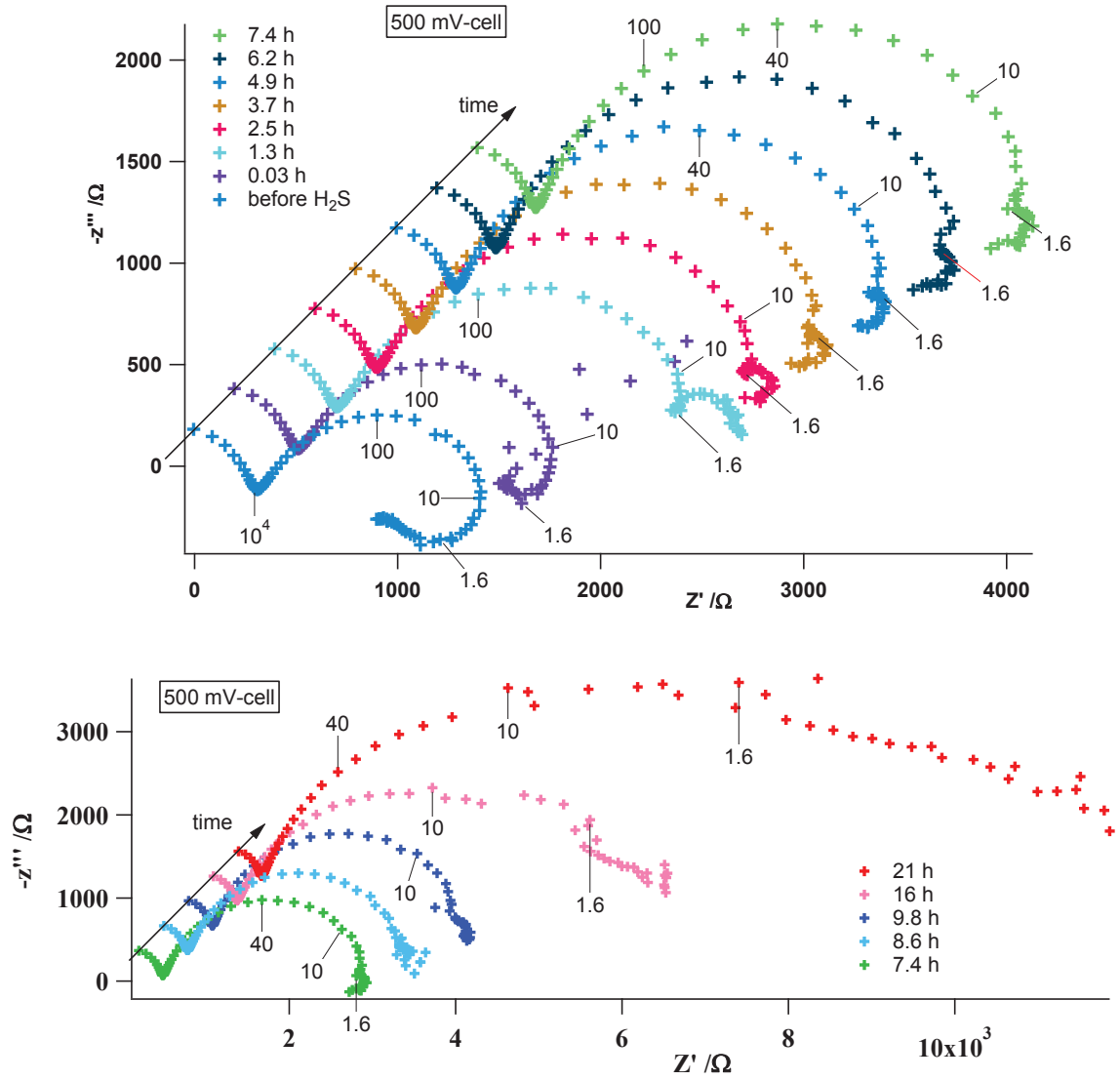

Figure 10. Nyquist plots of the 500mV-cell recorded in 200 ppm H_2S at 500°C as a function of time

The fits to the equivalent circuit were done for the spectra in the first 7.4 h only since after that the LF shape becomes undefined. Well fits were obtained as displayed in Figure 11.

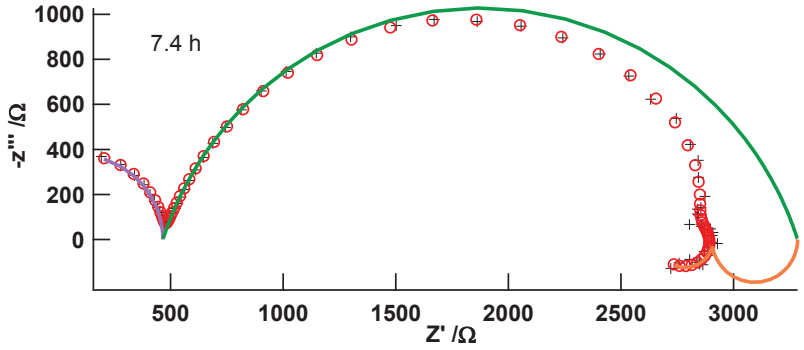

Figure 11. The fitted result for the impedance spectrum of 500mV-cell recorded at 7.4 h in 200 ppm H_2S at 500°C (black mark: experimental data, red circle: fitted data, colored lines: sub-circuits)

Table 6 shows the values of each electrical element under 200 pmm H_2S. Some of these values are then compared with those before H_2S exposure in Figure 12

Table 6. Fitted parameters for the 500 mV-cell in H_2S-containing fuel as a function of time.

Time/h	R_3/Ω	f_3/Hz	n_3	C_3 /10^{-6} F	R_{conc}/Ω	$f_{conc,num}$ /Hz	$f_{conc,den1}$ /Hz	$f_{conc,den2}$ /Hz
3.7 h	2426.61	40.14	0.78	1.63	-618.20	0.02	0.02	5.86
4.9 h	2441.83	39.42	0.80	1.65	-550.15	0.03	0.01	4.48
6.2 h	2566.51	36.48	0.81	1.70	-564.32	0.03	0.02	4.25
7.4 h	2818.85	31.25	0.80	1.81	-623.77	0.02	0.02	4.39

Figure 12 shows that when H_2S was added, the current went down abruptly with a decrease of about 48% after 7.4 h, and 81.5% after 19 h in 200 ppm H_2S. During the first 7.4 h, the sharp decrease of the current can be explained by a strong increase of the transfer resistance R_3 and a sharp decrease of the corresponding characteristic frequency. The contribution of the concentration resistance to the current deterioration is very moderate as compared to that of the transfer resistance. After 7.4 h, it was impossible to fit the data; however, the impedance in the frequency range corresponding mostly to the adsorption process grows very fast.

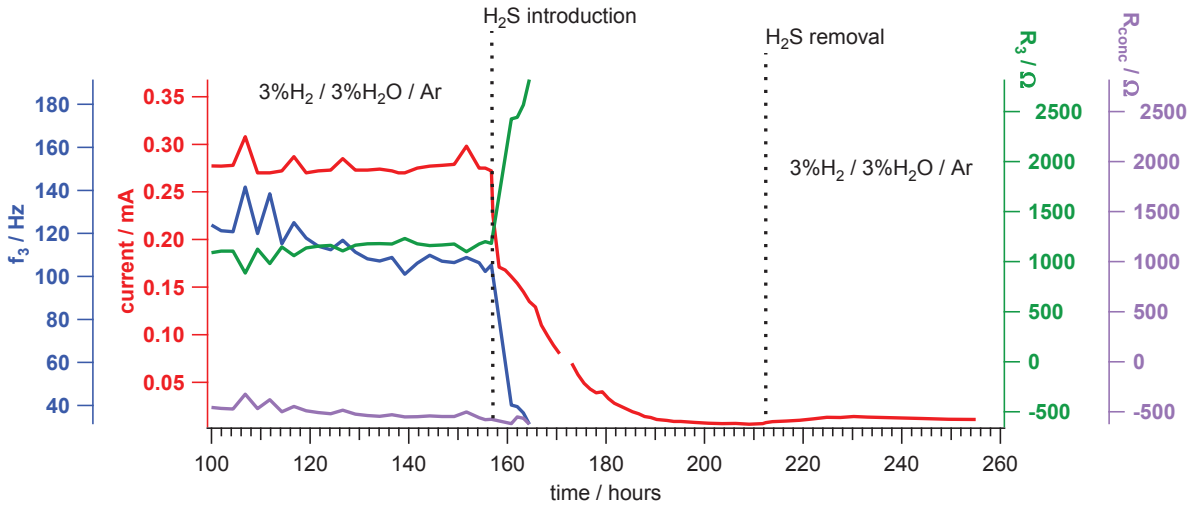

Figure 12. Evolutions of current, resistances, and characteristic frequency of 500 mV-cell before, during and after 200 ppm H_2S contact at 500°C

5.3. Conclusion

In clean fuel of 3%H_2/3%H_2O/Ar at 500°C, the current of 500 mV-cell diminishes continuously at first and then becomes rather stable. The trend can be well explained by the increase of the transfer resistance R_3 and the decrease of the characteristic frequency f_3. However, the concentration resistance R_{conc} decreases with time and has negative values. The fitted parameters demonstrate the slow degradation of the half-cell. The contact with H_2S during the first 7.4 h causes the current to decrease 48% and the transfer resistance to increase 3 times. The overall resistance becomes infinitive after ~20 h. The loss of anode performance is irreversible.

6. Effect of H_2S on cell in open circuit condition (OCP-cell) at 500°C

6.1. Aging behavior in clean fuel

The cell was kept permanently under open circuit condition during about 190 hours in clean fuel of 3%H_2/3%H_2O/Ar and the impedance was measured at zero bias every hour. As shown in the Nyquist plot of Figure 13, the impedance increases continuously with time. Bode plot indicates that the fastest enlargement comes from the LF semi-circle, while the HF part remains unchanged. Slower kinetics of MF and LF processes may be envisaged through the shifts of peak frequencies to lower values with time as shown in the Bode plot of Figure 12.

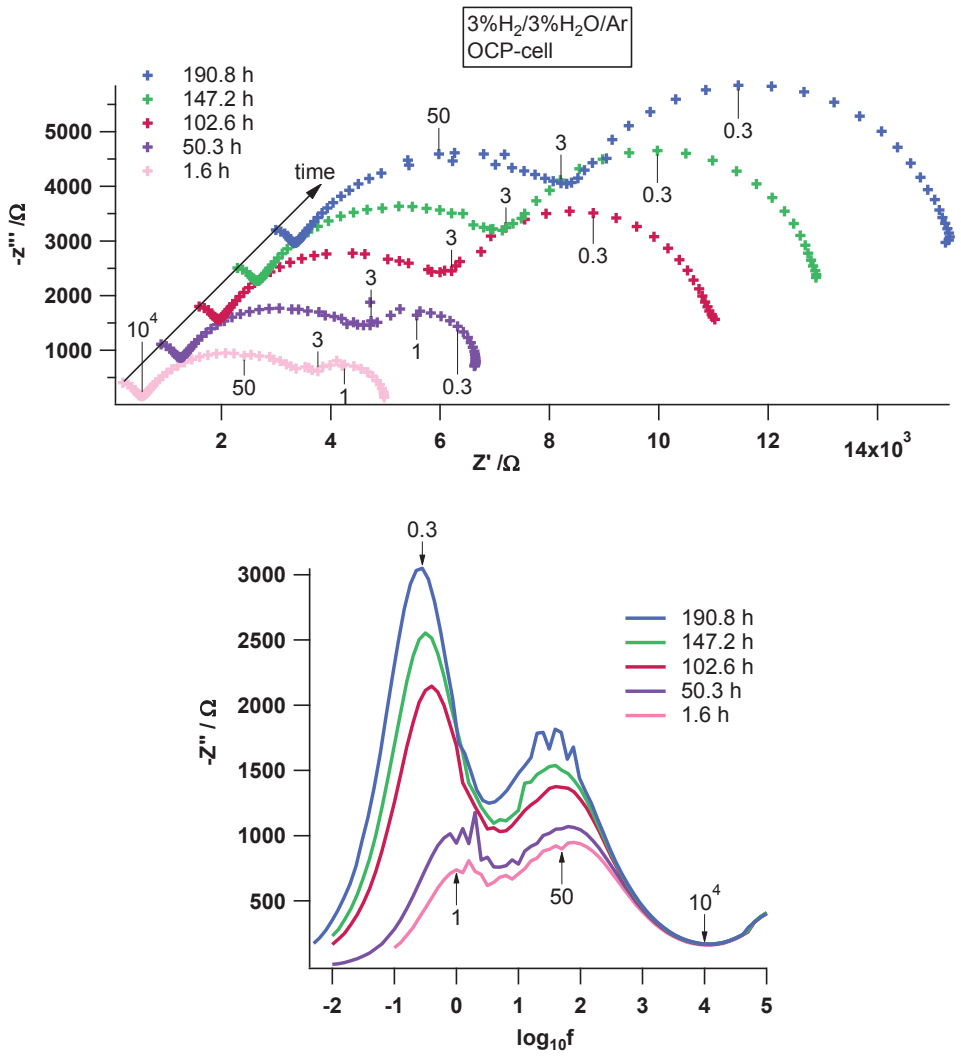

Figure 13. Nyquist and Bode plots of OCP-cell recorded at 500°C in clean fuel as a function of time

In order to find the evolutions of anode processes, the spectra were fitted to the equivalent circuit. Some fitted values are listed in Table 7.

Table 7. Fitted parameters for OCP-cell in clean fuel as a function of time.

Time/h	R_3/Ω	f_3/Hz	n_3	C_3 10^{-6} F	R_{conc}/Ω	$f_{conc,num}$ /Hz	$f_{conc,den1}$ /Hz	$f_{conc,den2}$ /Hz
1.6 h	3193.78	78.00	0.67	0.64	1337.33	2.49	0.85	4.96
50.3 h	3640.84	66.47	0.67	0.66	1828.71	0.76	0.56	1.16
102.6 h	4652.52	46.79	0.67	0.73	4405.22	0.16	0.14	0.43
147.2 h	4991.88	43.41	0.69	0.73	5269.39	0.18	0.14	0.39
190.8 h	5517.92	39.14	0.69	0.74	6451.64	0.11	0.10	0.30

Figure 14 displays the overall evolutions of the circuit parameters during ~190 hours in clean fuel. The transfer resistance R_3, the concentration resistance R_{conc} increase linearly with time. The characteristic frequency of the transfer process f_3 decreases with time, inferring a slowdown of the kinetics of the MF process. The time constants related to adsorption processes also decrease as read from Table 7. So as with 500 mV-cell, a gradual degradation of OCP-cell performance happens in clean fuel during 190 hours.

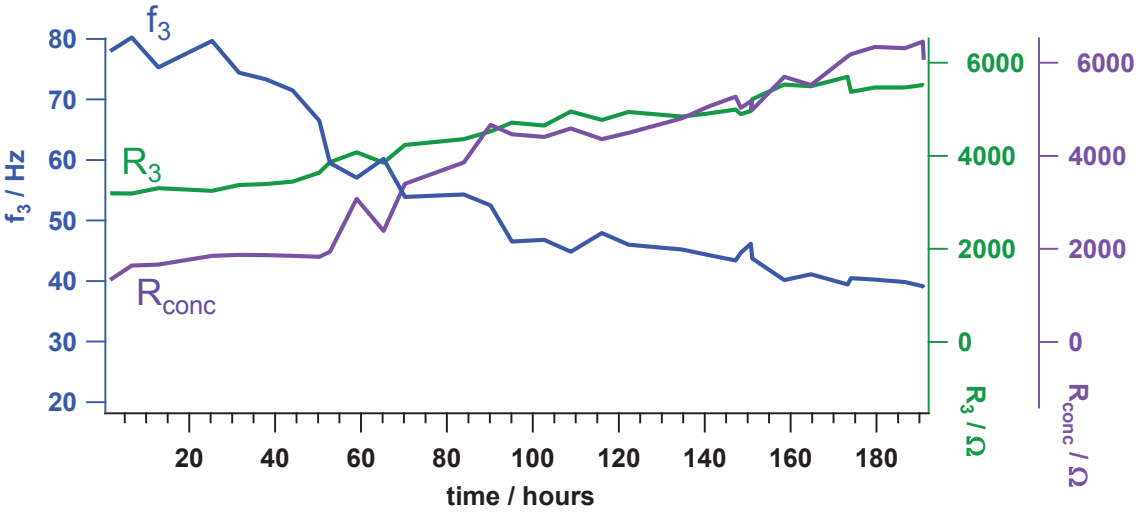

Figure 14. Evolutions of electrical parameters of OCP-cell as a function of time in clean fuel at 500°C

6.2. Effects of H_2S on electrical properties

Figure 15 shows the spectra obtained every hour after H_2S was introduced into the fuel stream. While the HF and MF showed almost no change, the LF capacitive loop changed surprisingly following three stages. During S_1 (first 5 h), the LF capacitive semicircle shrank quickly into a small distorted inductive loop. During S_2 (6-16 h), the distorted loop became spherical and symmetric; then it decreased in size with time. During S_3 (from 16 h on), the LF inductive loop developed into a capacitive loop intersecting with the MF loop. From 24.2 h on, the spectrum remained the same with 2 imbricated capacitive loops, the LF arc enlarging with H_2S exposure time.

The three stages may indicate the extent of H_2S poisoning since the LF part is supposed to relate to the adsorbed species like OH^-_{ads} and vacant sites at the TPB.

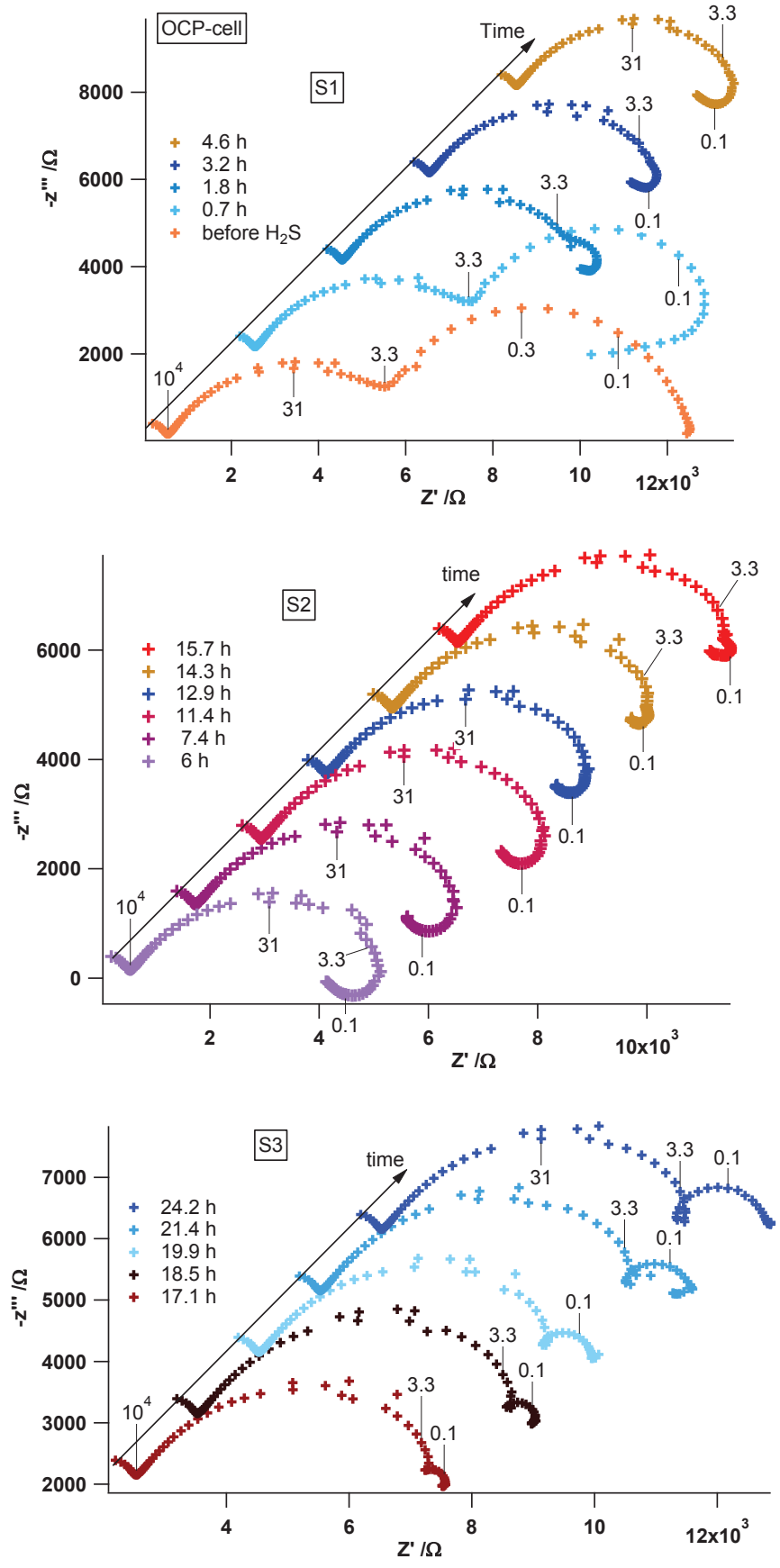

Figure 15. Nyquist plots of the OCP-cell recorded in 200 ppm H_2S at 500°C as a function of time

The fits were tried with the same circuit of $R_1(RC)_2(RQ)_3Z_{conc}$ as displayed in Figure 16. The fitted parameters are given in Table 8.

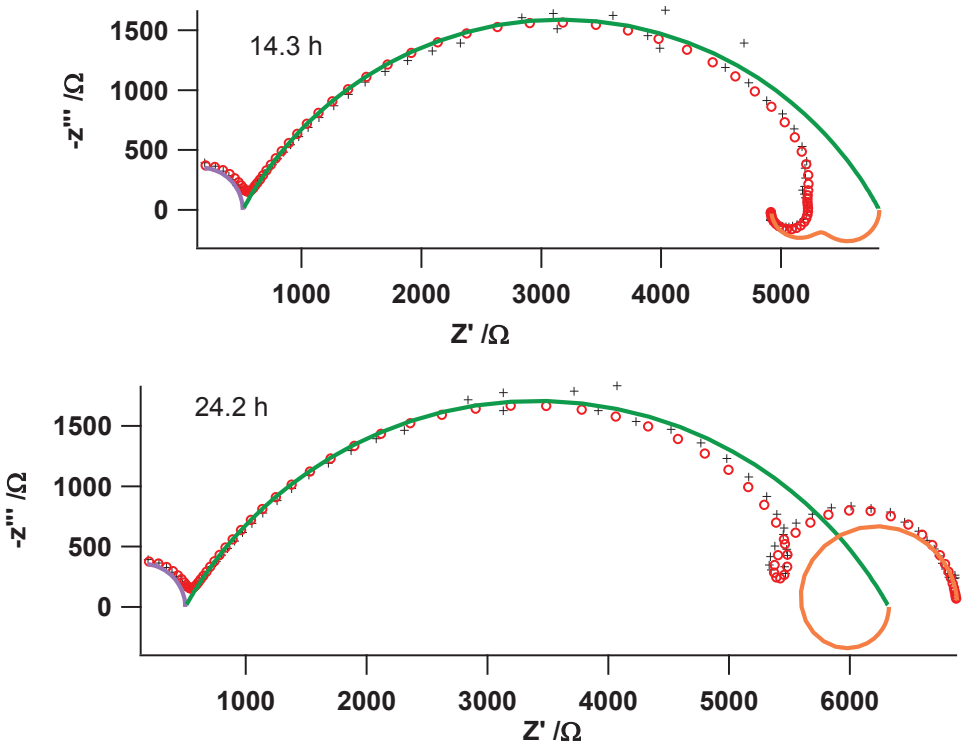

Figure 16. The fitted result for the impedance spectra of OCP-cell recorded at 14.3 and 24.2 h in H_2S at 500°C (black mark: experimental data, red circle: fitted data, colored lines: sub-circuits)

Table 8. Fitted parameters for OCP-cell in H_2S as a function of time.

Time/h	R_3/Ω	f_3/Hz	n_3	C_3 10^{-6} F	R_{conc}/Ω	$f_{conc,num}$ /Hz	$f_{conc,den1}$ /Hz	$f_{conc,den2}$ /Hz
10.1 h	5330.50	32.6	0.69	0.90	-1213.5	0.14	0.08	0.6
20 h	5611.60	27.5	0.67	1.03	-107.3	0.03	0.21	1.58
29.8 h	6144.20	22.6	0.65	1.10	1319.6	-0.12	1.65	0.09
36.8 h	6542.00	19.0	0.63	1.30	1429.4	-0.11	1.5	0.09
48 h	6021.00	24.5	0.66	1.10	1870	-0.21	1.5	0.09

Figure 17 shows the evolutions of the circuit parameters in the presence/absence of H_2S. Under H_2S, the characteristic frequency f_3 decreases faster, while R_3 increases slightly; nevertheless, it fluctuates much with time indicating the continuous changing of the anode. The transformation of

the LF capacitive loop into an inductive one during S_1 period is marked by negative values of the concentration resistance. During S_2, R_{conc} increases, and turns to positive values in S_3 period. It then becomes rather stable after 26 h exposure to H_2S, indicating the saturation of H_2S poisoning effect.

As H_2S was removed from the gas stream, f_3 slightly improves its value, implying a partial recovery of the charge transfer process; while R_{conc} still keeps its value, indicating a permanent poisoning of H_2S to the adsorption process.

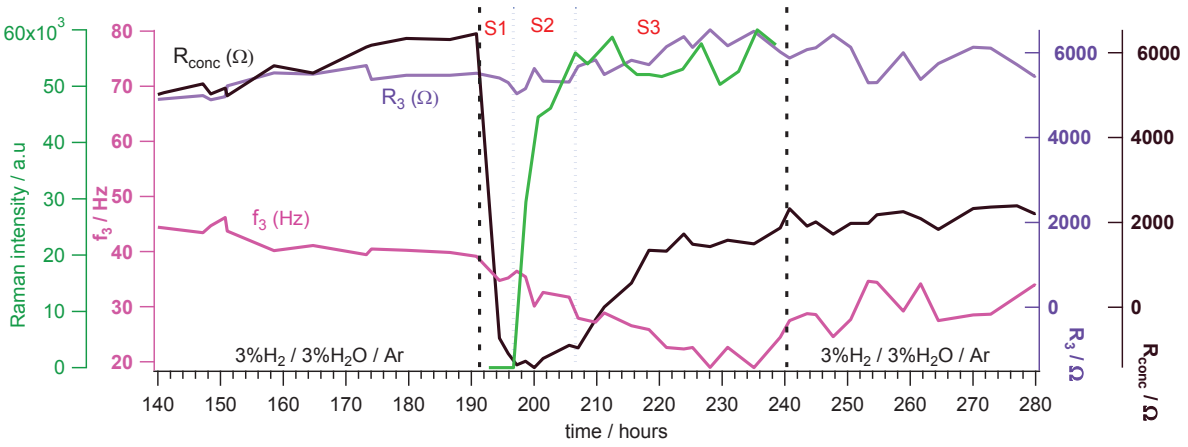

Figure 17. Evolutions of electrical parameters of OCP-cell as a function of time in 200 ppm H_2S at 500°C

6.3. Conclusion

For OCP-cell, during ~190 hours in clean fuel of 3%H_2/3%H_2O/Ar at 500°C, both the transfer resistance R_3 and the concentration resistance R_{conc} increase linearly with time. The characteristic frequency of the transfer process f_3 decreases with time. A gradual degradation of OCP-cell performance happens in clean fuel as with 500 mV-cell. Under H_2S, the charge transfer process slows down monotonously. The concentration resistance related to the adsorption process evolves complicatedly at first 20 hours, reflecting the extent of H_2S poisoning. Then it becomes rather stable, indicating a saturation of H_2S-effect. A partial recovery has been observed after H_2S removal, due to a recovery of the charge transfer process.

7. Correlation between nickel sulfide quantity and electrical changes

In situ Raman spectra of the anode surfaces of OCP-cell and 500 mV-cell were taken every 30 minutes after the introduction of 200 ppm H_2S, and are displayed in Figure 18. For the OCP-cell, the peaks corresponding to Ni_3S_2 can be seen clearly after 7.4 h. The quantity of Ni_3S_2 was determined using the area of the characteristic band at ~185 cm^{-1}. For the 500 mV-cell, the Raman intensity of nickel sulfide peaks was very weak and noisy, which makes the quantification impossible.

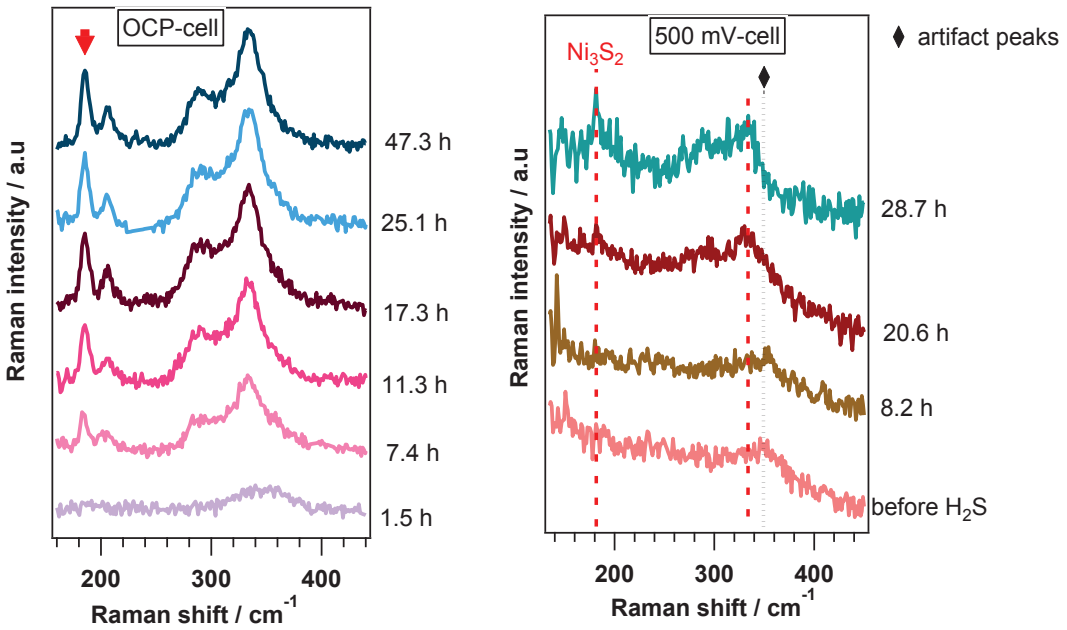

Figure 18. Raman spectra of anode surface versus exposure time to H_2S at 500°C. The arrow indicates the band used for Ni_3S_2 quantification

The evolution of nickel sulfide quantity on OCP-cell surface is shown together with the variations of electrical parameters in Figure 19. It can be seen that period S_1 corresponds well to the time where the peaks of Ni_3S_2 have not yet been observed on the anode surface. Therefore, the spectra during S_1 may indicate the onset of nickel sulfide nucleation or the adsorption of sulfur species on the anode surface. The S_2 stage correlates with the accumulation of Ni_3S_2 on the anode surface, while S_3 lies inside the saturation of Ni_3S_2 on the surface. The formation of the two intersected capacitive arc at ~20 h (see Figure 15, S_3) may signal the saturation of Ni_3S_2 in the range detected by Raman spectroscopy. The following enlargement may imply a continuous build-up of nickel sulfide deep inside the bulk anode.

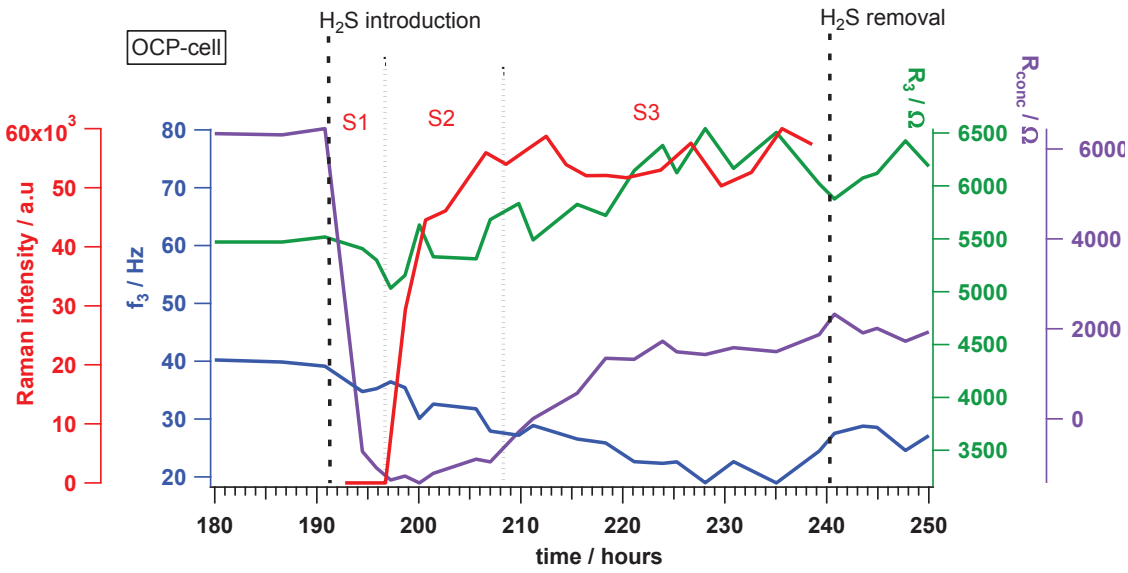

Figure 19. Evolutions of electrical parameters and nickel sulfide quantity of OCP-cell as a function of time in 200 ppm H_2S

For the 500 mV-cell, it is very surprising that the Raman intensities of nickel sulfide are very small despite the fact that cell resistance becomes enormously large after about 20 h exposed to H_2S (see Figure 10). It may be an experimental problem since the Raman measurements were done with an old objective that appeared later to be defective. Indeed, *ex situ* measures in room condition show no considerable difference in Raman intensities of nickel sulfide formed on the surfaces of the OCP- and the 500-mV cell.

8. Effect of H_2S on morphology change

The morphological differences between OCP-cell and 500mV-cell subjected to 200 ppm H_2S at 500°C are displayed in Figure 20.

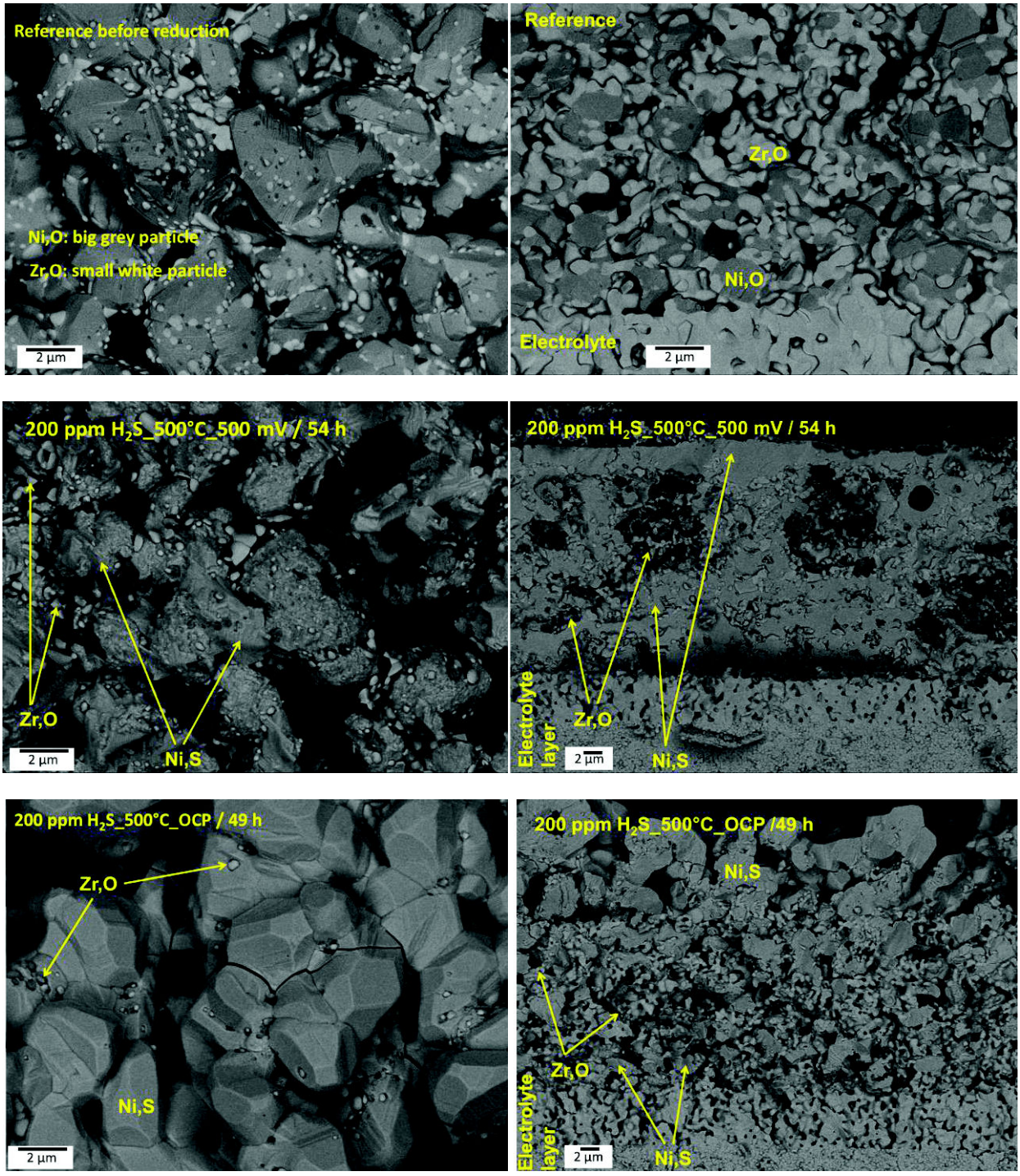

Figure 20. Backscattered-electron images of the anode surfaces (left column) and the cross-sections (right column) of the cells after H_2S-exposure

Compared with the reference, the 500mV-cell surface structure does not change much: the small particles of YSZ can be seen mixed with the (Ni, S) particles; while in case of the OCP-cell, they are buried inside big facetted agglomerates of (Ni, S). A look into the cross-sections reveals that in the OCP-cell, coalescence happens horizontally throughout the surface while the vertical interior still keeps its porous structure. In the 500 mV-cell, although no big agglomerate is seen at the surface, the interior is dense with (Ni, S). This can be understood by accepting that the coalescence develops perpendicularly with the surface into the electrolyte substrate rather than horizontally on the surface, thus link all the particles from the anode surface to the electrolyte substrate. The same morphology as the 500 mV-cell was obtained with a cell polarized at 100 mV.

9. Discussion

The results obtained with the two cells can be summarized as follows:

For both cells, the high frequency part of the impedance remains constant all over the experiments. As a consequence, we can assume that the bulk properties of the electrolyte and the electronic contact resistances (e.g. between the Pt grid and the Ni-YSZ electrode) remain constant.

The double layer capacitance C_3 is almost constant. In solid electrolytes, the double layer capacitance is attributed to charged species appearing at the surface of the solid electrolyte [24,25]. As it is roughly constant, we may consider that the surface of the electrolyte (Y-TSZ for the electrolyte itself and YSZ in the composite electrode) does not change much, either because of the current flowing through the cell or because of the atmosphere.

During the ageing in clean fuel, the transfer resistance R_3 evolves similarly for the two samples: it increases by a factor of 1.6 for the OCP-cell and by a factor of 1.9 for the 500 mV-cell after about 140 h. On the contrary, the concentration resistances R_{conc} evolves very differently: in the case of the OCP-cell, it increases from 1300 to 6400 Ω, while for the 500 mV-cell it decreases from -200 to -550 Ω, thus compensating the increase of R_3.

In contact with 200 ppm H_2S, these parameters evolve again very differently. For the OCP-cell, a large decrease of R_{conc} is first observed, followed by a partial recovery; while R_3 remains roughly constant. As a consequence, the polarization resistance $R_3 + R_{conc}$ is lower after 50 h in H_2S than before. For the 500 mV-cell, we observe at first an increase of R_3 during 7 h, then a large increase of R_3 and R_{conc}.

Different electrical behaviors between OCP and polarizing conditions may come from the role of a partial oxidation of Ni. Thermodynamic data for H_2O and NiO formation at 298 K, extracted from [26] are as follows:

$Ni + 1/2O_2 = NiO$ (22) $\Delta H_f^o = -239.7$ kJ mol^{-1}; $S^o = -94.45$ J mol^{-1} K^{-1}

$H_2 + 1/2O_2 = H_2O$ (23) $\Delta H_f^o = -241.8$ kJ mol^{-1}; $S^o = -44.45$ J mol^{-1} K^{-1}

Assuming that these values are temperature independent, the oxygen partial pressure of NiO stability is given by:

$$P_{O_2\,(NiO)} = \exp\frac{2\Delta H^o_{f,NiO}}{RT}\ \exp\frac{-2\Delta S^o_{NiO}}{R} \qquad (24)$$

The oxygen partial pressure resulting from the H_2/H_2O gas composition is given by:

$$P_{O_2\,(gas)} = \left(\frac{P_{H_2O}}{P_{H_2}}\right)^2 \exp\frac{2\Delta H^o_{f,H_2O}}{RT}\ \exp\frac{-2\Delta S^o_{H_2O}}{R} \qquad (25)$$

These two oxygen partial pressures are shown in Figure 21 as a function of temperature, with $P_{H_2O}=P_{H_2}$. As the curve for the gas composition is lower than that of NiO stability, NiO is unstable at all temperatures.

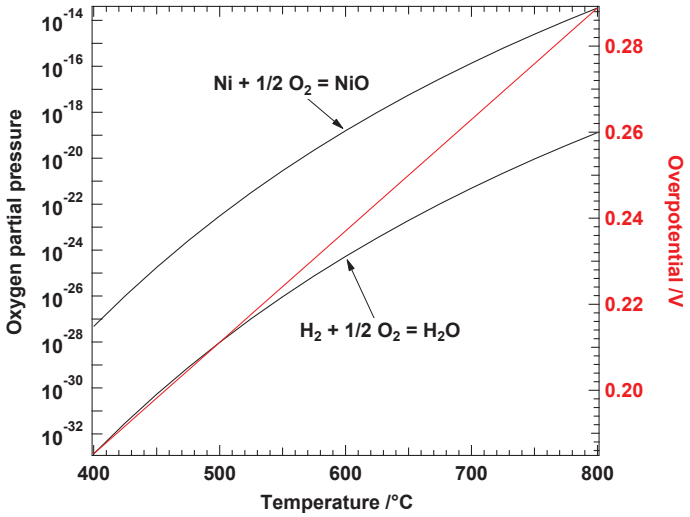

Figure 21. Thermodynamical stability of NiO and H_2O for $P_{H_2O}=P_{H_2}$ (black lines) and overpotential needed to stabilize NiO from an atmosphere with $P_{H_2O}=P_{H_2}$ (red line).

Positively polarizing the electrode is the same as increasing the oxygen partial pressure at this electrode.

$$\eta = \frac{RT}{4F} ln \frac{P_{O_{2,W}}}{P_{O_{2,REF}}} \qquad (26)$$

$$\eta = E_w - E_{ref} - RI \qquad (27)$$

where RI is the ohmic drop between reference and working electrodes and $P_{O_{2,REF}}$ is the oxygen partial pressure in the absence of current, i.e. P_{O_2}(gas).

The overpotential needed to stabilize NiO is also shown in Figure 21. It can be seen that a 500 mV applied voltage, with a 0.3 mA current and a 500 Ω resistance, is sufficient to stabilize NiO. Hence The Ni surface is at least partially covered with an oxide film.

An experiment at 100 mV polarization gave no reliable impedance results, probably because of a current leakage between one of the electrodes and the electric circuit of the heating lamps. However, a post-mortem SEM analysis revealed a H_2S contamination identical to that observed with the 500 mV-cell. Since a 100 mV polarization does not stabilize NiO, the presence of oxide is not sufficient to differentiate results at OCP and under polarizations. New experiments have to be made to assess the effect of NiO on the H_2S corrosion of the cell.

10. Conclusions

A background degradation of cell in open circuit or polarizing conditions was observed in clean fuel of 3%H_2/3%H_2O/Ar at 500°C. It results from the increase of the charge transfer resistance and the decrease of corresponding characteristic frequency. This could be due to the instability of the porous cermet structure, in which the small particles always tend to coalesce, thus reduce the number of active sites.

The second-order concentration impedance can help to fit well an equivalent circuit to complicated experimental data. The introduction of this element emphasizes the important role of adsorption on the active TPB length which is usually ignored in the reported impedance investigations.

For OCP-cell, correlations between electrical properties and nickel sulfide quantity have been well observed. The saturation of nickel sulfide at the surface corresponds to an impedance shape of two intersected capacitive arcs. The concentration resistance evolves the same trend with the nickel sulfide quantity.

For 500 mV-cell, the abrupt loss of cell current is explained by a strong increase of charge transfer resistance during the first 7 h. The strong enlargement of the impedance spectrum from 16 h in H_2S may correspond to the densification of the whole bulk anode of (Ni, S) phase.

Compared to OCP condition, the presence of a polarization will facilitate the formation of nickel sulfide deep inside the anode at the interface anode/electrolyte rather than at the anode surface. We have tentatively explained these two behaviors by the presence of NiO at high polarizations, but experiments are still needed to confirm this hypothesis.

REFERENCES

[1] R. J. Aaberg, R. Tunold, R. Ødegård, *Solid State Ionics* **2000**, *136–137*, 707.
[2] A. Bieberle, L. J. Gauckler, *Solid State Ionics* **2000**, *135*, 337.
[3] D. Kek, M. Mogensen, S. Pejovnik, *J. Electrochem. Soc.* **2001**, *148*, A878.
[4] K. V. Jensen, R. Wallenberg, I. Chorkendorff, M. Mogensen, *Solid State Ionics* **2003**, *160*, 27.
[5] S. P. Jiang, S. P. S. Badwal, *Solid State Ionics* **1999**, *123*, 209.
[6] M. Mogensen, K. V. Jensen, M. J. Jorgensen, S. Primdahl, *Solid State Ionics* **2002**, *150*, 123.
[7] P. Holtappels, I. C. Vinke, L. G. J. de Haart, U. Stimming, *Journal of The Electrochemical Society* **1999**, *146*, 2976.
[8] E. Brightman, D. G. Ivey, D. J. L. Brett, N. P. Brandon, *Journal of Power Sources* **2011**, *196*, 7182.
[9] K. Sasaki, K. Susuki, A. Iyoshi, M. Uchimura, N. Imamura, H. Kusaba, Y. Teraoka, H. Fuchino, K. Tsujimoto, Y. Uchida, N. Jingo, *Journal of The Electrochemical Society* **2006**, *153*, A2023.
[10] Y. Shiratori, T. Oshima, K. Sasaki, *International Journal of Hydrogen Energy* **2008**, *33*, 6316.
[11] J. F. B. Rasmussen, A. Hagen, *Fuel Cells (Weinheim, Ger.)* **2010**, *10*, 1135.
[12] J. W. Yun, S. P. Yoon, S. Park, H. S. Kim, S. W. Nam, *Int. J. Hydrogen Energy* **2011**, *36*, 787.
[13] P. V. Aravind, J. P. Ouweltjes, N. Woudstra, G. Rietveld, *Electrochem. Solid-State Lett.* **2008**, *11*, B24.
[14] U. P. Muecke, K. Akiba, A. Infortuna, T. Salkus, N. V. Stus, L. J. Gauckler, *Solid State Ionics* **2008**, *178*, 1762.
[15] S. Primdahl, M. Mogensen, *J. Electrochem. Soc.* **1997**, *144*, 3409.
[16] S. Primdahl, M. Mogensen, *J. Electrochem. Soc.* **1999**, *146*, 2827.
[17] M. Guillodo, P. Vernoux, J. Fouletier, *Solid State Ionics* **2000**, *127*, 99.
[18] J. P. Diard, G. B. Le, C. Montella, C. Montero-Ocampo, *J. Electroanal. Chem.* **1993**, *352*, 1.
[19] M. Vogler, A. Bieberle-Hütter, L. Gauckler, J. Warnatz, W. G. Bessler, *Journal of The Electrochemical Society* **2009**, *156*, B663.
[20] J.-H. Wang, Z. Cheng, J.-L. Bredas, M. Liu, *The Journal of Chemical Physics* **2007**, *127*, 214705.
[21] S. P. S. Badwal, M. V. Swain, *J Mater Sci Lett* **1985**, *4*, 487.
[22] O. Yamamoto, Y. Takeda, R. Kanno, K. Kohno, T. Kamiharai, *J Mater Sci Lett* **1989**, *8*, 198.
[23] X. Wang, N. Nakagawa, K. Kato, *J. Electrochem. Soc.* **2001**, *148*, A565.
[24] R. B. Poeppel, J. M. Blakely, *Surface Sci.* **1969**, *15*, 507.
[25] K. Lehovec, *J. Chem. Phys.* **1953**, *21*, 1123.
[26] http://owl.cengage.com/departments/GenChemKotz7eDemo0709/appendix/thermodynamic.html (23/11/2013)

GENERAL CONCLUSION & PERSPECTIVES

In situ Raman spectroscopy and optical imagery are effective in determining H_2S poisoning rate and extent in terms of sulfides amount and morphological changes; while *ex situ* Raman mapping elucidates the penetrating of sulfur attack inside the sample. The study shows that nickel sulfides are formed easily at low temperature (below 800°C), while cerium oxysulfide appears at ~750°C and above. The most severe change happens at 500°C as a result of the compromise between sulfur adsorption and sulfur-induced nickel diffusion. The formation of different sulfides at 200°C may create a volume expansion and a fissure inside the sample. So, much care has to be taken with an accidental presence of H_2S at low temperatures, during SOFC heating and cooling procedures.

The effect of H_2S on the electrochemical properties of a Ni-YSZ SOFC anode was also examined. The proposed electrical equivalent circuit comprising a second-order concentration impedance of adsorbed species can reproduce well the experimental data. A degradation of the cells in clean fuel is caused by an increase of the charge transfer resistance. In contact with H_2S, for the cell under open circuit condition, the concentration resistance increases and saturates with the amount of nickel sulfide measured by Raman spectroscopy. For the 500 mV- polarized cell, we observe at first an increase of charge transfer resistance, then an enormous increase of the concentration resistance which corresponds to a densification of the anode interior due to the presence of a Ni_xS_y phase. The ohmic drop between reference and working electrodes and the double layer capacitance are rather constant, showing that the electrolyte properties remain unchanged whatever the current or the atmosphere composition.

Compared to OCP condition, the presence of a polarization will facilitate the formation of nickel sulfide deep inside the anode rather than at the anode surface. We have tentatively explained these two behaviors by the presence of NiO at high polarizations, but experiments are still needed to confirm this hypothesis.

All the experiments were carried out with H_2S concentration range of 200-500 ppm; the electrochemical performance was investigated at 500°C. The high concentration of H_2S and low temperature were chosen in order to magnify the poisoning extent of H_2S so that it can be detected with high certainty by impedance spectroscopy, and especially by *in situ* Raman spectroscopy. Once reaction models have been established, e.g. the reactivity or the morphology change as a function of temperature, the electrical equivalent circuit…, they may act as guidance to test the more difficult and realistic experimental conditions, i.e. 0.1-10 ppm H_2S and 700-1000°C. For the future work, we suggest to conduct the measurements first with low H_2S concentration at 500°C, and then with low H_2S concentration at high temperature, e.g. 715°C or 800°C. We expect to be able to observe the adsorption phenomenon, which becomes weaker with increasing temperature, by impedance spectroscopy.

It is also important to study Ni-CGO/CGO half-cells to compare with Ni-YSZ/YSZ. CGO was proved in this study to react with H_2S at high temperature (to form $Ce_2O_{2.5}S$), so H_2S may attack the electrolyte part. In this case it would be interesting to know how the impedance spectra change.

We also suggest performing more fundamental studies on the H_2S poisoning kinetics with CGO, YSZ, Ni-YSZ at various temperatures and especially during the slow warming up stage.

Preliminary experiments were also conducted to observe the effect of another pollutant HCl. The experiments done in our laboratory show that Ni and Ni-CGO do not react with 500 ppm HCl (in 3% H_2/Ar) at 715°C and below. Experiments were conducted at CEA at 800°C. In this last case, surprisingly, CeOCl and $Ce_2O_{2.546}S$ were found in the Ni-CGO pellets exposed to 500 ppm HCl at 800°C. The presence of sulfide compound implies a residual presence of H_2S. The formation of sulfide compound is more likely to happen with very low H_2S concentration during the slow heating (5°C/min). Another interesting hypothesis is that the co-presence of the two pollutants HCl and H_2S may bring about more detrimental effect. This point needs to be developed in future work.

Summary

A Solid Oxide Fuel Cell (SOFC) can be fed with biogas without a preliminary reforming due to its high operating temperature. However, the biogas contains numerous pollutants like sulfur which poison the electrodes. This thesis focuses on the understanding of the H_2S impacts on the anode structure and electrical performances. Raman Spectroscopy, optical imagery and Impedance Spectroscopy have been used *in situ* to evaluate the sulfidation kinetics and the morphological changes of Ni and Ni-CGO pellets exposed to H_2S at various temperatures. The electrical performances of Ni-YSZ/YSZ/Pt cells under open circuit and 500 mV-polarizing conditions at 500°C have been measured. An electrical circuit with a second-order concentration impedance is proposed. The anode behaviors in clean and polluted fuel are discussed based on the evolutions of impedance shapes and on the fitted parameters. Correlations between the electrical properties and the build-up of nickel sulfide are presented.

Keywords: SOFC, *in situ* Raman Spectroscopy, *in situ* Impedance Spectroscopy, Ni-CGO, Ni-YSZ, hydrogen sulfur

---

Résumé

Une SOFC peut être alimentée en biogaz sans reformage préliminaire du fait de sa température de fonctionnement élevée. Cependant, la présence de polluants comme le soufre peut empoisonner les électrodes. Cette thèse se concentre sur la compréhension des effets de H_2S sur la structure de l'anode et les performances électriques. Spectroscopie Raman, imagerie optique et spectroscopie d'impédance ont été utilisées *in situ* pour évaluer la cinétique de sulfuration et les modifications morphologiques de Ni et Ni-CGO en présence de H_2S à différentes températures. Les performances électriques de Ni-YSZ/YSZ/Pt ont été mesurées à 500°C à l'abandon et sous polarisation (500 mV). Un circuit électrique avec une impédance de concentration du second ordre est proposé. Les caractéristiques de l'anode avec combustibles propre et pollué sont discutées à partir des formes et des décompositions des spectres. Les corrélations entre propriétés électriques et accumulation de sulfure de nickel sont présentées.

Mots clés: SOFC, Spectroscopie Raman *in situ*, Spectroscopie d'impédance *in situ*, Ni-CGO, Ni-YSZ, sulfure d'hydrogène